# High Order Large Eddy Simulation for the Analysis of Tonal Noise Generation via Aeroacoustic Feedback Effects at a Side Mirror

A thesis accepted by the Faculty
of Aerospace Engineering and Geodesy of the University of Stuttgart
in partial fulfillment of the requirements for the degree of
Doctor of Engineering Sciences (Dr.-Ing.)

by

**Hannes M. Frank**

born in Filderstadt

| | |
|---|---|
| Main referee: | Prof. Dr. Claus-Dieter Munz |
| Co referee: | Prof. Dr. Christophe Bailly |
| Date of defence: | May 12, 2017 |

Institute of Aerodynamics and Gas Dynamics
University of Stuttgart

2017

Für Miriam, Andrea und Eberhard.

# Preface

This thesis was developed during my time as academic employee at the Institute of Aerodynamics and Gas Dynamics (IAG) of the University of Stuttgart.

At this point I would like to thank my doctoral supervisor Prof. Dr. Claus-Dieter Munz for his support, the great time I had in his exceptional group and the scientific freedom I was granted during the PhD project. Furthermore, I thank Prof. Christophe Bailly for being my co-referee.

I also would like to thank Dr. Michael Jaroch from the aerodynamics team at Audi AG for the professional and friendly supervision of the side mirror project.

Many thanks also go to all current and past members of the Numerics Research Group I was able to work with, I always enjoyed the open and relaxed working atmosphere. I shared many interesting collaborative research and student projects, discussions and jokes with Florian Hindenlang, Andrea Beck, Thomas Bolemann, David Flad, Nico Krais, Matthias Sonntag and Serena Keller. I am also thankful for working together on the side mirror project with Maike Werner, who strongly contributed to the success of the project.

Last but not least, I am grateful for the love and the ongoing support of my parents, family and my girlfriend Miriam.

Stuttgart, June 10, 2017

Hannes Frank

# Contents

**Preface** v

**Contents** vii

**Symbols and Abbreviations** xi

**Kurzfassung** xiii

**Abstract** xv

**1 Introduction** 1
- 1.1 Tonal trailing edge noise 3
  - 1.1.1 Observations 3
  - 1.1.2 Interpretation 4
- 1.2 Objectives 6
- 1.3 Structure of the thesis 7

**2 Physical and numerical modeling** 9
- 2.1 Governing equations 9
- 2.2 Direct computation of flow-induced sound 10
- 2.3 Large eddy simulation 13
  - 2.3.1 Subgrid scale models 14
  - 2.3.2 Influence of the numerical scheme 15
  - 2.3.3 LES of transitional flows 17
- 2.4 Numerics 18
- 2.5 Current Implementation 20
  - 2.5.1 Polynomial bases and the projection operator 20
  - 2.5.2 Transformation of the equations 21
  - 2.5.3 Variational formulation 22
  - 2.5.4 DGSEM implementation 23
  - 2.5.5 Approximation of the viscous fluxes 26
  - 2.5.6 Non-conforming interfaces 27

2.5.7 Time discretization . . . . . . . . . . . . . . . . . . . . . . . 31
2.5.8 Under-resolved simulations and stability . . . . . . . . . 31
2.5.9 Boundary conditions for aeroacoustics . . . . . . . . . . . 33
2.5.10 Parallelization and performance . . . . . . . . . . . . . . 34
2.6 Analysis tools . . . . . . . . . . . . . . . . . . . . . . . . . . . 35
2.6.1 Classical linear stability theory . . . . . . . . . . . . . . 35
2.6.2 Global perturbation formulation . . . . . . . . . . . . . 36
2.6.3 Dynamic mode decomposition . . . . . . . . . . . . . . . 37
2.7 Validation . . . . . . . . . . . . . . . . . . . . . . . . . . . . . 40

**3 Simulation of a side mirror** **45**
3.1 Object of investigation . . . . . . . . . . . . . . . . . . . . . . 45
3.2 Simulation setup . . . . . . . . . . . . . . . . . . . . . . . . . 46
3.3 Computational mesh . . . . . . . . . . . . . . . . . . . . . . . 47
3.4 Simulation results . . . . . . . . . . . . . . . . . . . . . . . . 51
3.4.1 Time-averaged flow field . . . . . . . . . . . . . . . . . . 51
3.4.2 Acoustic emissions and source identification . . . . . . . 55
3.4.3 Unsteady flow field . . . . . . . . . . . . . . . . . . . . . 59
3.5 Stability analysis . . . . . . . . . . . . . . . . . . . . . . . . . 63
3.5.1 Base flow choice . . . . . . . . . . . . . . . . . . . . . . 63
3.5.2 Local linear stability analysis . . . . . . . . . . . . . . . 64
3.5.3 Impulse response analysis . . . . . . . . . . . . . . . . . 66
3.5.4 Modal decomposition . . . . . . . . . . . . . . . . . . . 70
3.5.5 Relation to the phase condition . . . . . . . . . . . . . . 73
3.6 Summary and discussion . . . . . . . . . . . . . . . . . . . . . 74

**4 Analysis of a simplified mirror model** **75**
4.1 Definition of the mirror model . . . . . . . . . . . . . . . . . . 75
4.2 Simulation setup . . . . . . . . . . . . . . . . . . . . . . . . . 77
4.2.1 Strategy . . . . . . . . . . . . . . . . . . . . . . . . . . . 77
4.2.2 Computational meshes and parameters . . . . . . . . . . 78
4.3 Base flow simulation . . . . . . . . . . . . . . . . . . . . . . . 81
4.3.1 Flow field . . . . . . . . . . . . . . . . . . . . . . . . . . 81
4.3.2 Acoustic emissions . . . . . . . . . . . . . . . . . . . . . 83
4.4 Subdomain simulation . . . . . . . . . . . . . . . . . . . . . . 85
4.4.1 Mean flow . . . . . . . . . . . . . . . . . . . . . . . . . . 85
4.4.2 Unsteady flow . . . . . . . . . . . . . . . . . . . . . . . . 86
4.4.3 Acoustic emissions . . . . . . . . . . . . . . . . . . . . . 88

4.5 Ladder structure . . . . . . . . . . . . . . . . . . . . . . . . . . 90
    4.5.1 Acoustic results . . . . . . . . . . . . . . . . . . . . . . 91
    4.5.2 Phase condition . . . . . . . . . . . . . . . . . . . . . . 91
4.6 Stability analysis . . . . . . . . . . . . . . . . . . . . . . . . . 93
4.7 Geometrical countermeasures against feedback tones . . . . . . 97
    4.7.1 Truncated trailing edge . . . . . . . . . . . . . . . . . . 99
    4.7.2 Lowered trailing edge . . . . . . . . . . . . . . . . . . . 102
    4.7.3 Modified design edge . . . . . . . . . . . . . . . . . . . 105
4.8 Summary and discussion . . . . . . . . . . . . . . . . . . . . . . 109

**5 Conclusions and prospects** **113**
5.1 Conclusions . . . . . . . . . . . . . . . . . . . . . . . . . . . . . 113
5.2 Prospects . . . . . . . . . . . . . . . . . . . . . . . . . . . . . . 115

**Bibliography** **117**

**List of Tables** **129**

**List of Figures** **131**

**Lebenslauf** **137**

# Symbols and Abbreviations

## Symbols

| | |
|---|---|
| $L_{\mathrm{SP}}$ | splitter plate length |
| $L_z$ | spanwise extent of the domain |
| $M$ | polynomial degree of the operator used for de-aliasing |
| $N$ | polynomial degree of the solution |
| $N(s)$ | N factor at station $s$ |
| $N_{\mathrm{geo}}$ | polynomial degree of the geometric mapping $\vec{x}(\vec{\xi})$ |
| $N_p(\delta_{99})$ | number of solution points in the boundary layer in the wall-normal direction |
| $n_{\mathrm{GP}}$ | total number of integration points based on $M$ |
| $n(f)$ | integral amplification of a spatially growing instability |
| $n_{\mathrm{Elems}}$ | number of elements |
| $n_{\mathrm{Elems},z}$ | number of elements in the spanwise direction |
| $s$ | wall-tangential distance to the trailing edge |
| $T^*$ | convective time unit based on a length scale and the free-stream velocity |
| $\tilde{t} = t/T^*$ | non-dimensional time unit |
| $U$ | conservative state vector |
| $U'$ | fluctuation state vector |
| $u_\delta$ | wall-tangential velocity at the edge of the boundary layer |
| $\vec{v} = (u, v, w)^T$ | velocity vector |
| $\Delta x = \frac{\Delta x_{\mathrm{Elem}}}{N+1}$ | Grid spacing based on the element-local resolution |
| $\Delta x_{\mathrm{Elem}}$ | element size |
| $\vec{x} = (x, y, z)^T$ | three-dimensional coordinates |
| $-\alpha_i$ | spatial growth rate |
| $\omega_r$ | global angular frequency |
| $\omega_i$ | global temporal growth rate |

## Abbreviations

| | |
|---|---|
| BR | Bassi-Rebay |
| CAA | Computational aeroacoustics |
| CFD | Computational fluid dynamics |
| CG | Continuous Galerkin |
| DE | Design edge |
| DFT | Discrete fourier transform |
| DG | Discontinuous Galerkin |
| DGSEM | Discontinuous Galerkin spectral element method |
| DMD | Dynamic mode decomposition |
| DNC | Direct noise computation |
| DNS | Direct numerical simulation |
| DOF | Degree(s) of freedom |
| DRP | Dispersion relation preserving |
| IAG | Institute for Aerodynamics and Gas Dynamics |
| LE | Leading edge |
| LES | Large eddy simulation |
| LWT | Laminar Wind Tunnel |
| PID | Performance index |
| PIV | Particle image velocimetry |
| POD | Proper orthogonal decomposition |
| ppw | Points per wavelength |
| PSD | Power spectral density |
| RANS | Reynolds averaged Navier-Stokes |
| SGS | Subgrid scale |
| SPL | Sound pressure level |
| TE | Trailing edge |

# Kurzfassung

In dieser Arbeit werden die Umströmung eines Seitenspiegel und die daraus resultierende tonale Geräuschentstehung mittels hochgenauer Large Eddy Simulationen untersucht. Die Vermeidung tonaler Geräusche, welche als störende Pfeifgeräusche wahrgenommen werden können, ist ein wesentliches Ziel der aeroakustischen Optimierung eines Kraftfahrzeugs. Die hierbei zugrunde liegenden Mechanismen sind noch nicht vollständig geklärt und können in der Regel nicht mit den heute in der Industrie verwendeten Aeroakustik-Lösern erfasst werden. Bei Spiegelgehäusen, die eine laminare Ablösung stromauf der Hinterkante aufweisen, sind akustische Rückkopplungseffekte, die bei der Umströmung von Tragflügeln bekannt sind, eine mögliche Ursache.

Um den hohen Genauigkeitsanforderungen Rechnung zu tragen, werden die Simulationen basierend auf der Discontinuous Galerkin Spektrale Element Methode durchgeführt, welche eine hohe Verfahrensordnung bietet. Die geometrische Flexibilität wird durch die zusätzliche Einführung nicht-konformer, dreidimensional gekrümmter Elemente erhöht.

Die Untersuchung wird anhand eines Seitenspiegels durchgeführt, welcher in dem betrachteten frühen Entwicklungsstand ausgeprägte tonale Geräusche entwickelt. Analog zu einer parallel durchgeführten experimentellen Arbeit wird der Untersuchung ein einzelner Seitenspiegel auf dem Windkanalboden zugrunde gelegt. In Vergleichen mit statischen Wanddruckmessungen, Hitzdraht- und PIV-Messungen ergibt sich eine bemerkenswerte Übereinstimmung zwischen dem berechneten und dem experimentellen Strömungsfeld. Das akustische Spektrum weist dominante schmalbandige Komponenten auf, welche durch Wirbelablösungen stromab einer Ablösung der laminaren Grenzschicht verursacht werden. Die in der Simulation identifizierten Quellregionen am Spiegel entsprechen den experimentellen. Weiterhin wird für eine der tonalen Frequenzen quantitative Übereinstimmung erreicht. Eine Störungsrechnung zeigt, dass eine globale Instabilität in Form einer akustischen Rückkopplungsschleife genau die diskreten Frequenzen auswählt, welche in der Strömungssimulation beobachtet werden. Diese Rückkopplungsschleife beinhaltet konvektives Störungswachstum in der abgelösten Scherschicht, akustische Abstrahlung an der Hinterkante und Einkopplung der akustischen Emissionen in die stromauf befindliche Grenz-

schicht durch natürliche Rezeptivität.
Dieser Mechanismus wird in einem zweiten Schritt anhand eines speziell entwickelten vereinfachten zweidimensionalen Modells genauer untersucht. Ein Subdomain-Konzept wird eingeführt, um die zweidimensionale Form des Modells zu nutzen und den hohen Rechenaufwand zu umgehen, der mit dem Nachlauf des stumpfen Körpers einhergeht. Die Abhängigkeit der tonalen Frequenzen von der Anströmgeschwindigkeit wird in den Simulationen nachgebildet und weist die Eigenschaften der im Experiment beobachtete sogenannten “ladder structure” auf. Des Weiteren lässt sich die Entwicklung der Frequenzen im betrachteten Geschwindigkeitsbereich mit einem theoretischen Rückkopplungsmodell basierend auf der linearen Stabilitätstheorie vorhersagen. Zuletzt wird die Wirksamkeit verschiedener Modifikationen der Spiegelkontur untersucht, um die tonalen Geräusche zu beseitigen.
Die vorliegende Arbeit leistet einen wesentlichen Beitrag zum Verständnis der Entstehung tonaler Strömungsgeräusche, welches bei zukünftigen Entwicklungen zugrunde gelegt werden kann. Darüber hinaus wurde bestätigt, dass relevante, aber wenig robuste aeroakustische Mechanismen auch für komplexe Geometrien mit dem vorgestellten Discontinuous Galerkin Löser erfasst werden können.

# Abstract

In this work, the flow around a side mirror and the resulting tonal noise generation are investigated using highly accurate compressible large eddy simulations. Avoiding tonal noise, which can be perceived as disturbing whistling sound, is a crucial target in automotive aeroacoustics. However, the underlying mechanisms are not completely understood and can typically not be captured with state of the art computational aeroacoustics solvers used in industry. Acoustic feedback effects known from tonal airfoil self-noise are a possible cause at smooth mirror housings that exhibit laminar separation upstream of the trailing edge.

Since this application demands high accuracy, a simulation code based on the high order discontinuous Galerkin spectral element method is employed. To enhance geometrical flexibility, it is augmented with an extension to non-conforming curved elements in three dimensions.

In the first part of the investigation, the simulation framework is used to analyze an early development stage side mirror exhibiting tonal noise generation. Adopting the corresponding experimental configuration, the study considers an isolated side mirror mounted on the wind tunnel floor. The computational flow field is shown to agree remarkably well with the experimental one based on comparisons with static wall pressure, hotwire and PIV measurements. Discrete peaks are obtained in the computational acoustic spectrum, originating at the trailing edge of the mirror downstream of laminar separation. The identified tonal noise source regions match the experimental ones and quantitative agreement is achieved for one of the tonal peak frequencies. Perturbation simulations reveal global acoustic feedback instabilities selecting the same discrete frequencies observed in the developed flow. The feedback loop comprises convective disturbance growth in the separated shear layer, scattering at the trailing edge and reinforcement through receptivity to the emitted sound in the upstream boundary layer.

In a second step, this mechanism is studied in more detail based on a specifically designed simplified two-dimensional model. A subdomain approach is introduced to exploit the two-dimensional shape and circumvent the computational cost associated with the bluff body wake of the model. Simulations of a range of free-stream velocities exhibit tonal frequencies varying similarly to the experimentally observed so-called 'ladder structure'. The tone frequencies are shown to evolve according to a theoretical feedback model based on linear stability theory. Finally, the efficacy of various modifications to the mirror contour to eliminate tonal noise generation is evaluated.

The present work contributes to the understanding of tonal noise generation mechanisms and can guide future designs. Moreover, it corroborates the capacity of the present discontinuous Galerkin framework to accurately capture relevant but delicate aeroacoustic effects at complex geometries.

# 1 Introduction

The airstream around a vehicle is among the most important noise sources in automotive development, especially towards higher traveling speeds [50]. Naturally, its relative impact on the overall noise becomes even higher for hybrid and electric vehicles. Despite considerable progress in applied computational aeroacoustics methods [103] and computing performance, aeroacoustic optimization of vehicles is still largely carried out in full-scale wind tunnel experiments. Therein, the side mirror requires special attention owing to its vicinity to the driver's ear and its bluff-body shape. In the mirror housing design process, a complex trade-off must be achieved, which includes rain water management, good visibility and size, aesthetics, manufacturing costs and aerodynamic drag. Thus, neutral sound emission is only one of many design targets – a circumstance which imposes tight limits on possible countermeasures addressing aerodynamic sound generation at the mirror.

The mirror is also a well-known source of tonal noise. The associated narrowband components in the acoustic spectrum are typically perceived as disturbing whistling sounds. Consequently, their elimination is crucial in aeroacoustic optimization. While the tones are known to often originate due to the flow of laminar boundary layers over notches or other water management devices and joints, they have also been observed to sometimes originate from smooth parts of the mirror housing. Furthermore, increasingly efficient aerodynamic vehicle shapes lead to a less disturbed flow around the mirror, promoting the generation of laminar whistling sounds [77]. The multitude of possible noise generation processes is not fully understood. Better fundamental understanding is needed to facilitate target-oriented design choices and improve engineering prediction tools.

Besides wind tunnel experiments, numerical simulations are the most important tool for fundamental research in fluid mechanics. Previous numerical work on side mirror aeroacoustics mostly concentrated on the generic side mirror experiment presented by Höld et al. [53] and Siegert et al. [108] in 1999, which was subsequently used e.g. in [5, 101] to evaluate the capacity of different computational aeroacoustics (CAA) approaches to predict the experimental acoustic spectra. An example of a non-generic side mirror simulation with remarkable agreement to measurements is given by Khaligi et al. [59]. However, tonal noise was not addressed in these studies, nor did it appear in the published reference measurements.

In a number of engineering applications, flow-induced tonal noise is associated with feedback mechanisms from the acoustic field to the unsteady flow. Popular examples include cavity noise [22], screech noise in supersonic jets [97] and the laminar whistling sounds at low Reynolds number airfoils [3, 21, 24, 32, 56, 61, 85, 93, 95, 111], which are discussed in detail in the following subsection. A characteristic feature of the latter is the presence of a laminar, typically separated boundary layer close to the trailing edge. The similarities to the flow around side mirrors producing laminar whistling sounds as for instance observed by Lounsberry et al. [77] indicate that acoustic feedback effects could play a role.

The hybrid CAA approaches employed in previous investigations [5, 59, 101, 108] are based on incompressible flow simulations and a posteriori noise prediction, which renders them incapable of capturing acoustic feedback effects. To that end, a direct noise computation is necessary, which represents a more general, physically accurate approach and is thus the first choice for fundamental studies. However, it also requires high accuracy of the numerical scheme and considerable computing power. For the present application, a high fidelity simulation procedure is needed that accurately describes acoustic wave propagation as well as the flow dynamics relevant to the noise generation across all flow regimes from laminar to turbulent. At the same time, it must support a comparatively complex geometry such as the side mirror. Discontinuous Galerkin (DG) methods gain popularity in the field of high fidelity CFD (computational fluid dynamics) due to their high accuracy, geometrical flexibility and suitability for massively parallel computations [45]. In the current work, we employ the simulation framework Flexi[1] based on the high order discontinuous Galerkin spectral element method (DGSEM) with an extension for non-conforming interfaces on curved, three-dimensional meshes.

This numerical work is part of an experimental [114–117] and numerical project to investigate the details of tonal noise generation at a side mirror and a simplified mirror model. Consequently, it is possible to validate and interpret the results by cross-referencing with experimental analyses of the same geometries. In this part of the project we present numerical evidence for acoustic feedback tones developing at the side mirror under investigation, thoroughly analyze the noise generation mechanism and evaluate countermeasures.

---

[1] open source at `https://www.flexi-project.org/`

## 1.1 Tonal trailing edge noise

As noted above, indications exist that sources of tonal noise at mirror housings could be driven by acoustic feedback effects at mirror housings in some cases, similar to feedback effects observed for airfoils at low to medium Reynolds numbers. Although the first well-recognized investigation by Paterson et al. [89] dedicated to tonal noise generation at isolated airfoils dates back to 1973, some open questions still draw the attention of researchers today.

### 1.1.1 Observations

Addressing discrete-frequency noise emitted from helicopter rotors, Paterson et al. [89] measured discrete components in the acoustic spectrum resulting from the flow around isolated NACA 0012 and NACA 0018 airfoils at $Re = 3 \cdot 10^5$ to $2.2 \cdot 10^6$ in a low turbulence open-jet wind tunnel. They already reported the main observations that were later confirmed and addressed in other works.

The tones were only present in the range of Reynolds number and angle of attack where the boundary layer at the pressure side remained laminar until shortly upstream of the trailing edge. Boundary layer tripping forward of 80% chord at the pressure side made the tones disappear, clearly linking the tones to a laminar boundary layer state. McAlpine et al. [81] and Nash et al. [85] later noted a dependency of tone occurrence on laminar separation upstream of the trailing edge of the pressure side. However, in the latter work, the authors also highlight a case where no tone established despite laminar separation of the boundary layer.

The typical variation of the tone frequencies with the free-stream velocity $u_\infty$ is schematically depicted in Fig. 1.1. Paterson et al. found the tone frequencies to follow a general trend proportional to $u_\infty^{3/2}$ and to be organized along several regularly spaced lines, like rungs of a ladder, which led to the term 'ladder structure'. If the velocity is increased, the tone frequency rises along the corresponding line proportional to about $u_\infty^{0.8}$. With a further increase in velocity, at some point, the frequency 'jumps' onto the next rung. In some cases, two or more simultaneous tones appeared, which was confirmed in facilities with both open [3, 95] and closed [85, 93] test-sections. However, in the closed wind tunnel experiments performed by Nash et al. [85], the number of tones was largely reduced through the use of acoustic lining, indicating a strong influence of the experimental conditions on the precise tone frequencies.

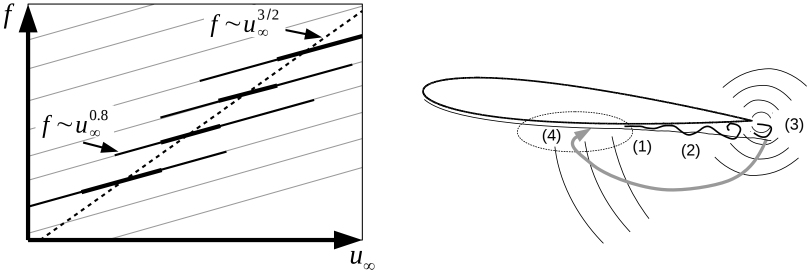

Figure 1.1: Left: Idealized diagram of the tone frequency development with respect to free-stream velocity. Thick lines: dominant tones, solid lines: associated side peaks, dashed line: general trend, thin lines: frequencies fulfilling the phase condition.
Right: Schematic of the aeroacoustic feedback loop. (1) separation point, (2) amplified instability in the separated shear layer, (3) diffraction at the trailing edge, (4) reinforcement of the instability by the upstream traveling acoustic wave.

### 1.1.2 Interpretation

An early model concept was given by Paterson et al., who proposed vortex shedding at the trailing edge as the origin of the tonal noise. Assuming a constant Strouhal number based on the boundary layer thickness at the trailing edge, they derived an empirical law consistent with the approximate $u_\infty^{3/2}$ scaling of the general trend. The inability of their model to explain the fine structure of the tones led Tam [111] to suggest a self-excited feedback loop consisting of large-scale unstable disturbances in the wake and upstream traveling acoustic waves. Generally, a feedback loop implies a vanishing phase difference about one cycle. This phase condition can only be fulfilled by discrete frequencies, naturally explaining the discrete rungs.

Fink [28] noted that according to trailing edge noise theory [46], the diffraction of amplified boundary layer instabilities at the trailing edge should be the primary noise source. Based on Fink's notion, Arbey and Bataille [3] proposed a revised variant of Tam's feedback loop. Therein, as outlined in Fig. 1.1 (right), upstream propagating acoustic waves reinforce the boundary layer instabilities at some position upstream through natural receptivity [102], again leading to a closed loop selecting discrete frequencies. Theoretical models based on that concept exhibit notable quantitative agreement to the fine structure of the measured tones [3, 21, 61, 93]. However, they do not allow a statement regarding the dominant tone frequency but merely predict the whole set of potential feedback frequencies indicated as gray lines in Fig. 1.1. Furthermore, these models rely on either simple scaling laws or linear stability theory (LST) to obtain the phase velocities of the boundary layer instabilities and require the specification of the unknown effective receptivity location. Ad hoc choices have been the point of maximum velocity along the airfoil [3] or the branch I point of first instability [21, 61]. By use of so-called receptivity strips, Plogmann et al. [93] were able to prescribe the effective receptivity site and could show that upon variation of the position of the receptivity strips the measured tone frequencies varied as predicted by the feedback model. Their results provide convincing experimental evidence for the selection of the tone frequencies via an acoustic feedback loop.

A different explanation for the discrete frequencies not necessarily dependent on an acoustic feedback loop was raised by McAlpine et al. [81], who proposed that frequency selection takes place during the amplification process close to the point of separation, where the range of the most amplified frequencies is comparatively narrow. Consequently, the dominant tone should match the most amplified frequency as predicted by LST. Their measured tone frequencies compared reasonably well to LST predictions based on the time-averaged velocity profiles obtained via laser Doppler anemometry.

Desquesnes et al. [24] followed the hypothesis of McAlpine et al. in the interpretation of their two-dimensional direct numerical simulation (DNS) of the NACA 0012 airfoil and obtained remarkable agreement between the dominant tone and the most amplified frequency according to LST. The computational spectrum also featured regular side peaks, which they related to an amplitude modulation of the dominant tone. They traced down this modulation to a phase mismatch between the hydrodynamic fluctuations convecting over both sides of the trailing edge. However, Pröbsting et al. [95] measured the flow and acoustic radiation at similar conditions and found a remaining amplitude modulation even when the suction side boundary layer is turbulent, showing that the phase mismatch cannot be the only reason for the occurrence of side peaks.

The two-dimensional DNS carried out by Jones and Sandberg [56] directly revealed the presence of an aeroacoustic feedback loop apparently selecting the dominant tone frequency. They tracked a low-amplitude isolated disturbance that was amplified while traveling through the boundary layer and generated an acoustic wavepacket once convected past the trailing edge. The upstream running component of the acoustic wavepacket initiated another hydrodynamic wavepacket, leading to a system of alternating wavepackets. This sequence can also be understood as global instability [93, 113]. The corresponding frequency resembled the tonal peak frequency observed in the developed flow but was significantly lower than the most amplified frequency yielded by LST. This discrepancy with previous interpretations [3, 24, 81] was attributed to the preference of lower frequencies of the acoustic receptivity and the trailing edge scattering process, shifting the globally most amplified frequency to a lower value.

The global stability characteristics of the flow around a NACA 0012 airfoil at similar conditions were analyzed numerically by Fosas de Pando et al. [32] using an Arnoldi type algorithm. They showed that the frequencies of the leading global linear instability modes correspond directly to the regularly spaced discrete tone frequencies found in the developed flow, demonstrating that each peak arises directly from a global instability and not due to nonlinear interactions. In line with this finding, they deduced how the superposition of two or more modes appears as amplitude modulation in the time signal.

Despite some controversy regarding the precise frequency selection mechanism, the feedback loop as proposed by Arbey and Bataille [3] in conjunction with a laminar separation is currently the most reasonable concept explaining the features of the ladder structure while being supported by recent numerical analyses [32, 56]. Based on these considerations, an aeroacoustic feedback loop appears likely to occur at side mirrors exhibiting laminar separation in the vicinity of the trailing edge.

## 1.2 Objectives

The following objectives are addressed in this thesis:

- Establish a DGSEM simulation framework to tackle complex aeroacoustic problems such as the side mirror tones by validation with published references and application to the side mirror problem.
- Find and confirm the fundamental tonal noise generation mechanism for the side mirror under investigation by analyzing the computational flow field supported by the corresponding experimental data.
- Study the tonal noise mechanism, evaluate parametric dependencies and propose and examine possible countermeasures.

## 1.3 Structure of the thesis

In Chapter 2, we begin with a discussion of direct noise computation and large eddy simulation (LES) with emphasis on the application to transitional flows and the requirements for the numerical scheme. Subsequently, the simulation framework is described, including the numerical scheme and the associated LES approach as well as the post-processing tools used to interpret the computational data.

The LES results for a particular side mirror geometry generating laminar whistling tones are presented in Chapter 3. A detailed analysis of the flow field and the radiated sound as well as comparisons with the experimental results are given. Furthermore, the underlying mechanisms are elucidated based on local and global stability considerations.

Building on these findings, the mechanism is studied in detail in Chapter 4 by means of two- and three-dimensional simulations of the flow around a simplified mirror model specifically designed to mimic the noise source at the original mirror. The trends of the acoustic spectrum with respect to the free-stream velocity are analyzed and compared to the experimental 'ladder structure'. Eventually, possible geometrical countermeasures are evaluated and discussed.

The current analysis contributes to the understanding of aeroacoustic noise generation mechanisms – not only for side mirrors. It is summarized in Chapter 5 together with the implications and conclusions for high order scale resolving simulations as well as automotive design.

# 2 Physical and numerical modeling

This chapter is devoted to the fundamental modeling aspects related to the direct computation of flow-induced sound. Compressible large eddy simulation and high order accurate numerics are the main building blocks. Having established this context, we present the simulation approach of this work. Furthermore, we discuss the post-processing tools to analyze and evaluate the computational data. The last section of the chapter presents the results of a validation study.

## 2.1 Governing equations

The compressible Navier-Stokes equations are the basic governing equations for a compressible, viscous fluid in motion. We write them in terms of the vector of conserved quantities $U = (\rho, \rho v_1, \rho v_2, \rho v_3, \rho e)^T$, where $\rho$ denotes density of the fluid, $\vec{v} = (v_1, v_2, v_3)^T$ the velocity vector and $e$ the total energy, i.e. the sum of internal and kinetic energy per unit mass.

The governing equations describe the temporal evolution of the conserved quantities and can be written in conservative form

$$U_t + \vec{\nabla}_x \cdot \vec{F}(U, \vec{\nabla}_x U) = 0. \tag{2.1}$$

where the subscript $t$ indicates the derivative with respect to time and $\vec{\nabla}_x = (\partial/\partial x, \partial/\partial y, \partial/\partial z)^T$. The flux vector can be split into advective and viscous fluxes, $\vec{F} = \vec{G}(U) - \vec{H}(U, \vec{\nabla}_x U)$, which read for each spatial coordinate direction $d$

$$G^d(U) = \begin{pmatrix} \rho\, v_d \\ \rho\, v_1 v_d + \delta_{1d}\, p \\ \rho\, v_2 v_d + \delta_{2d}\, p \\ \rho\, v_3 v_d + \delta_{3d}\, p \\ \rho\, e v_d + p\, v_d \end{pmatrix}, \; H^d(U, \vec{\nabla}_x U) = \begin{pmatrix} 0 \\ \tau_{1d} \\ \tau_{2d} \\ \tau_{3d} \\ \tau_{dj} v_j - q_d \end{pmatrix} \tag{2.2}$$

with $d = 1, 2, 3$. In (2.2), $p$ identifies the static pressure and $\delta_{ij}$ the Kronecker delta. The viscous stress tensor $\underline{\tau}$ appearing in $\vec{H}(U, \vec{\nabla}_x U)$, employing Stokes' hypothesis, is defined as

$$\underline{\tau} := \mu \left( \vec{\nabla}_x \vec{v} + (\vec{\nabla}_x \vec{v})^T - \frac{2}{3} (\vec{\nabla}_x \cdot \vec{v}) \underline{I} \right). \tag{2.3}$$

Here, $\underline{I}$ is the identity matrix. The heat flux $\vec{q} := (q_1, q_2, q_3)^T$ is written as

$$\vec{q} = -k \vec{\nabla}_x T, \tag{2.4}$$

where we use $k = \frac{c_p \mu}{Pr}$ for the heat conductivity. We restrict ourselves to fluids obeying the perfect gas law and constant material values. Specifically, these are the molecular viscosity, Prandtl number and the specific heats denoted by $\mu$, $Pr = 0.71$, $c_p$ and $c_v$. Using the adiabatic coefficient $\kappa = \frac{c_p}{c_v}$ and the specific gas constant $R = c_p - c_v$, finally the perfect gas law

$$p = \rho R T = (\kappa - 1)\rho(e - \frac{1}{2}\vec{v} \cdot \vec{v}), \quad e = \frac{1}{2}\vec{v} \cdot \vec{v} + c_v T \tag{2.5}$$

is used to close the system of equations.

## 2.2 Direct computation of flow-induced sound

The available methods to compute the acoustic radiation based on a CFD calculation can be divided into *direct* and *hybrid* approaches. The former is sometimes referred to as *direct noise computation* (DNC). It builds upon the fact that both acoustic wave generation and propagation are contained in the compressible Navier-Stokes equations (2.1). Typical applications include jet noise [16, 17], cavity noise [69, 99] and trailing edge noise [24, 32, 56, 80].

We characterize DNC by comparing the properties of both strategies. The procedures are sketched in Fig. 2.1. The starting point in both cases is a flow simulation to obtain the unsteady flow field. In the more commonly used hybrid approach[1], the acoustic wave propagation is calculated in a separate step using acoustic source terms obtained from the preceding fluid flow solution. This separation is motivated by the disparity between the large length scales and low energy scales of the acoustic field compared to the fluid flow. A large number

---

[1] In this context, 'hybrid approach' refers to methods that numerically solve an additional partial differential equation for the acoustic field. Integral methods, such as the one by Ffowcs Williams and Hawkings [119] imply a further simplification and can be employed at significantly lower computational cost. These methods are efficient and without alternative for farfield predictions over long distances but do not cover scattering problems at arbitrarily shaped surfaces.

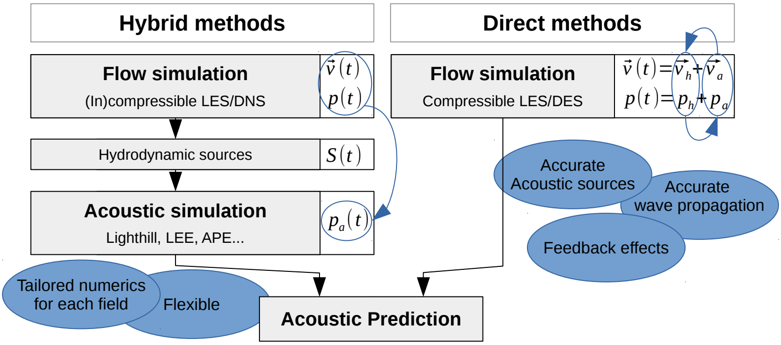
Hybrid methods
Direct methods
Flow simulation
(In)compressible LES/DNS
$\vec{v}(t)$
$p(t)$
Hydrodynamic sources
$S(t)$
Acoustic simulation
Lighthill, LEE, APE...
$p_a(t)$
Flow simulation
Compressible LES/DES
$\vec{v}(t)=\vec{v}_h+\vec{v}_a$
$p(t)=p_h+p_a$
Accurate Acoustic sources
Accurate wave propagation
Feedback effects
Tailored numerics for each field
Flexible
Acoustic Prediction

Figure 2.1: Comparison of direct and hybrid procedures and their properties for aeroacoustic noise prediction. Here, $(\cdot)_h$ and $(\cdot)_a$ denote hydrodynamic and acoustic components and $S(t)$ represents the acoustic source term.

of different formulations exist, many of them based on the inhomogeneous wave equation derived by Lighthill [75] and extensions thereof [57, 103]. In addition, various forms of perturbation equations based on the linearized Euler equations are employed [14, 26, 84]. Each formulation relies on different assumptions and simplifications regarding acoustic wave propagation with respect to the mean flow and the functional relationship between the acoustic source terms and the hydrodynamic fluctuations.

The decoupling between fluid flow and acoustic field in the hybrid approach implies flexibility in the choice of equation system and numerical method for both the flow and the acoustics calculation. As opposed to DNC, in the low Mach number range the incompressible Navier-Stokes equations may be employed to obtain the acoustic sources, potentially leading to substantial savings in computational effort due to larger time steps. The hybrid approach also allows to analyze sound radiation from different parts of the flow field in an isolated fashion by truncating the source regions. However, the flexibility of hybrid acoustics prediction methods also comes with increased complexity, since in order to exploit the resolution benefits gained through decoupling, it requires two computational grids and either synchronous execution or time-resolved storage and interpolation of the source terms onto the acoustic grid [103].

In contrast, the concept underlying DNC is simple. The relevant physics are captured in the numerical solution of one partial differential equation system using one computational grid. No further modeling assumption regarding the acoustic sources or the wave propagation is introduced with the direct approach, whereas the formulation of hybrid aeroacoustic models and source terms is a whole field of active research. Often, direct noise computations are used as reference for hybrid techniques, e.g. in [26].

The crucial property of the direct approach is that it permits feedback effects from the acoustic field to the fluid flow. Owing to the decoupling of the hydrodynamic and the acoustic field, hybrid acoustic predictions based on incompressible flow calculations exclude this effect. Due to the low energy of the acoustic waves compared to the hydrodynamic fluctuations especially at low Mach numbers, it is often regarded as negligible, for instance in [5,53,59,101,108] for noise predictions of the flow around generic and non-generic side mirrors. However, there are situations where the acoustic field strongly affects the developed flow, often leading to tonal noise. Acoustic feedback effects are known to be an essential component in screech noise in supersonic jets [97], cavity tones [22, 69, 99] and the trailing edge tones at airfoils at low to medium Reynolds numbers to which an overview is given in Section 1.1.

DNC thus represents a first principle approach that is often preferred in fundamental investigations of flow-induced sound. Whereas the hybrid approach is able to exploit the scale disparity to separate both fields, one is faced with a true multi-scale problem when conducting a DNC, which introduces severe requirements for the numerical scheme.

The simulation of wave propagation over large distances requires high accuracy to minimize artificial attenuation and phase errors. The accuracy of a numerical scheme can be represented in the number of grid points required to resolve a propagating wave (ppw) with a defined limit for the numerical dispersion and dissipation error. This perspective enables a refined analysis of the numerical error in contrast to merely considering the order of convergence. Directly addressing this issue, Tam and Webb [112] proposed optimized dispersion relation preserving (DRP) differencing schemes. Their fundamental idea is to sacrifice the optimal order of convergence in favor of low dispersion and dissipation errors down to a design ppw limit. More sophisticated optimized schemes were later developed based on their concepts [15, 60]. Bogey and Bailly [15] also stress the importance of the accuracy of the time integrator and propose optimized Runge-Kutta schemes. Irrespective of what particular

numerical scheme is chosen, these accuracy requirements must be kept in mind.
Another issue arises from the necessary, but artificial truncation of the computational domain. It can produce spurious reflections, which must be counteracted by non-reflective boundary conditions. For DNC, especially the outflow boundary poses a challenge, since there nonlinearly strong disturbances may be present that can cause artificial acoustic sources polluting the solution [23]. In addition, artificial reflections can also occur in regions of abrupt mesh coarsening [103], so that high quality meshes are required.

Regardless of the modeling choice for the sound propagation, the acoustic sources directly arise from hydrodynamic fluctuations, which necessitates the use of unsteady, scale-resolving CFD simulations, if no additional empirical input is to be included. To that end, we conduct large eddy simulations (LES) in the current work, for which low dispersion and dissipation errors are also highly beneficial. However, for LES there are further requirements on the numerical scheme in terms of robustness and stability, which are elaborated in the following discussion of LES. To equally and simultaneously cover all of the above conditions in a numerical simulation is the crucial challenge in the field of DNC.

## 2.3 Large eddy simulation

If the compressible or incompressible Navier-Stokes equations are solved without the use of a turbulence model, one speaks of direct numerical simulation (DNS). However, depending on the flow problem, a large bandwidth of length and time scales can appear. If the computational mesh is chosen fine enough, a solution is approached that is independent of the numerical scheme and grid. The multi-scale nature of turbulent flows is the main driver of the required resolution and the associated computational cost. This cost can be estimated to increase with the Reynolds number $\propto Re^3$ [94]. For application oriented simulations the cost mostly becomes unacceptable. Today, DNS is being viewed as too computationally expensive, despite the tremendous increase of available computational resources and the progress in numerical methods over the past decades.

A significantly less costly alternative for the simulation of turbulent flows is LES, where the grid size is chosen coarser than the smallest eddies, such that only a portion of the turbulent spectrum is resolved. The underlying assumption of a scale separation between large and small eddies is based on the hypotheses of Kolmogorov [63]. The motion of the large eddies depends on the boundary conditions, they are in general anisotropic and they contain the bulk of the fluctuation energy. Kolmogorov's first and second hypotheses state that the small eddies, at sufficiently high Reynolds number, are locally isotropic, exhibit universal statistics and contain only a small share of the fluctuation energy. Furthermore, most of the viscous dissipation occurs at the small scales. LES aims at the resolution of only the large scales, while the effects of the small, unresolved scales on the resolved ones are typically approximated by a turbulence model.

For practical flow simulations at realistic Reynolds numbers, the Reynolds-averaged Navier-Stokes (RANS) approach is the most common choice. The governing equations are averaged in time and a solution for the mean flow field is sought. The effects of the unsteady turbulent motion (i.e. the complete spectrum of turbulent eddies) are described by a turbulence model. Instead of a time-dependent problem, a steady one must be solved and the computational grids must only resolve the (much smoother) mean flow field, leading to a drastic reduction in computational effort compared to LES, not to mention DNS. For that reason, RANS is still the state of the art in engineering CFD.

However, one can expect significant improvement of mean flow results yielded by LES over RANS calculations in flows where the unsteady motion of the largest scales is important, such as jet flows, airfoils near stall or bluff-body flows [51, 94, 109]. Even more importantly, as mentioned in Section 2.2, in CAA applications unsteady flow simulations are necessary to represent the acoustic sources.

### 2.3.1 Subgrid scale models

Conceptually, the separation between large and small scales is accomplished by applying a spatial filtering operator to the governing equations [73]. Due to the nonlinearity of the latter, the resulting system still depends on scales smaller than the filter width. This dependency is expressed in the subgrid stress tensor. In practical simulations, this unknown tensor must be represented by a subgrid scale (SGS) model, which is commonly referred to as closure problem. Comprehensive overviews on the available models and their properties are given in the review articles by Lesieur and Métais [74], Piomelli [90] and Meneveau and Katz [82].

The viscous dissipation of kinetic energy is mainly associated with the smallest scales of motion, which are not or only marginally resolved in an LES. On these grounds, it is agreed that in most cases the main task of the subgrid scale model is to introduce dissipation to the resolved scales as a substitute for the energy flux towards smaller scales. The prototypical mechanism for this process is the energy cascade encountered in homogeneous isotropic turbulence [90]. At present, the most important and commonly used SGS models belong to the class of eddy viscosity models [39, 76, 86], which are strictly dissipative provided the associated SGS viscosity is non-negative. However, it is also well-known that the SGS stresses yielded by models of this type do not correlate well with the real SGS stresses in a priori analyses [82].

### 2.3.2 Influence of the numerical scheme

Traditionally, subgrid scale models in LES are constructed from a physics-based point of view, analogously to RANS models. RANS models lead to a closed system of modified governing equations, which are subsequently discretized and solved numerically. A convergent numerical discretization of a given problem should then approximate the exact solution (of the model equation) with vanishing grid spacing. This property is not given for LES. Convergence in the strict sense is only reached when the filter width approaches the smallest scales of motion, i.e. once the LES becomes a DNS. Thus, LES are under-resolved simulations by design and their solutions are highly dependent on the spatial resolution and the properties of the numerical scheme.

To further realize the influence of the numerical scheme in LES, consider the spectral distribution of a velocity field predicted by a well-resolved DNS as sketched in Fig. 2.2. The spectral distribution of kinetic energy strongly decreases towards the wavenumber associated with the smallest scale. In that grid-converged scenario, numerical errors are negligible, as they only affect the smallest scales. If LES is employed with a spectral cutoff wavenumber $k_{c,\mathrm{LES}}$, even the smallest scales represented by the LES grid exhibit non-vanishing energy. As opposed to a well-resolved DNS, we encounter spectral overlap between the range of scales carrying finite energy and the range where finite numerical errors occur.

In fact, the magnitude of the numerical dissipation error can be on the same order as the modeled subgrid scale dissipation [40, 68]. Consequently, in any LES the solution is governed by a nonlinear interaction between the subgrid scale model and finite numerical errors resulting from the chosen discretization [13]. The observation of the strong influence of numerical dissipation led to the development of so-called *implicit* LES approaches that solely rely on the numerical error as a substitute for an explicit SGS model. Examples are the monotonically integrated LES [18] or the approximate local deconvolution method [42]. An alternative approach is to use carefully designed numerical filters to control the energy of the marginally resolved scales [16].

Another consequence of under-resolution is that the order of accuracy of a numerical scheme loses its formal meaning. However, the favorable dissipation and dispersion properties of high order methods still suggest their superiority for any scale-resolving application [11]. Numerical evidence demonstrated that these theoretical properties of a given scheme lead to more accurate results. In their study of truncation and aliasing errors in LES of incompressible turbulent channel flow, Kravchenko and Moin [68] reported a deterioration of the mean velocity profile, second order statistics and energy spectrum for a second order differencing scheme compared to a spectral scheme with the same number of grid points. Similar observations were made by Gassner and Beck [37] in their study of the Taylor-Green vortex problem. In an under-resolved 16th order simulation, the dissipation rate agreed remarkably well with DNS reference data, while the results of the corresponding second order simulation displayed severe deviations.

Besides the superiority of high order accuracy for LES, in both papers [37, 68]

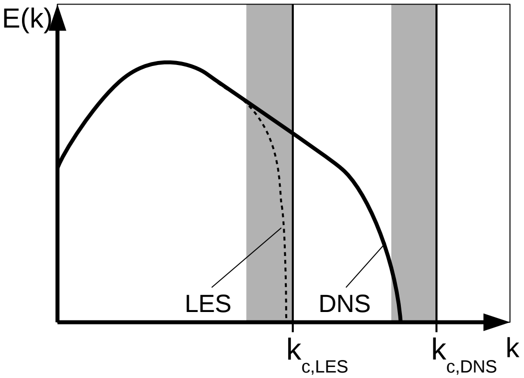

Figure 2.2: Schematic of a turbulent kinetic energy spectrum. $k_c$ marks the cutoff wavenumber given by the grid resolution. The gray-shaded areas mark the ranges of the marginally resolved scales, which are prone to numerical errors.

the strong impact of aliasing errors in high order LES was emphasized. This error arises due to the representation of the non-linear convection terms of the governing equations on the same discrete grid or basis used for the solution itself and can cause numerical instability. In contrast to the truncation error, techniques to remove this error can be applied [62] but they significantly add to the computational cost. Numerical dissipation caused by the truncation error may mask aliasing as a source of instability when using a low order scheme but tends to be insufficient for high order approximations depending on the degree of under-resolution [37].

In summary, these investigations highlight the strong influence of the numerical scheme on the results of LES. Regardless of the pursued SGS modeling approach, the superior approximation properties of high order schemes render them attractive in this context, but aliasing-induced instability must be controlled.

### 2.3.3 LES of transitional flows

LES of practical transitional flows (say, to model a wind tunnel experiment) is faced with the same challenges as DNS. The transition location and the specific instability mechanisms involved in a particular flow are largely dependent on boundary conditions such as wall roughness and the intensity and spectral characteristics of the inflow turbulence. This dependency on environmental conditions may lead to reproducibility issues in experiments between different laboratories or different specimen. A popular example is the wide range of experimentally observed transition locations $Re_{\text{crit}} = 3 - 5 \cdot 10^5$ for the laminar boundary layer on a flat plate [105]. As a consequence, boundary conditions should be defined with great care in a simulation of transitional flow. This also has to be kept in mind when interpreting the results or comparing simulation results to measurements.

In many transition scenarios, the fundamental instability mechanism is of relatively large length scale, i.e. it can in principle be resolved if the laminar velocity profile is captured by the grid. For instance, in the laminar flat plate (Blasius) boundary layer, the wavelengths of the unstable Tollmien-Schlichting waves scale with the boundary layer thickness, at $Re_{\delta^*} \approx 2000$ they lie between 5 and $14\delta_{99}$ (Sec. 6.1 in [79]). At later stages of transition, which exhibit rapid production of increasingly smaller scales, the situation differs between LES and DNS. In an adequately resolved DNS, production will continue up to the smallest length scale determined by viscous effects, while in an LES, this process is limited by the cut-off wavenumber of the computational grid or the SGS model.

Several applications of LES to canonical transitional flows are reported in literature, e.g. [48, 49, 91, 92]. The applicability of LES for transitional flows has been extensively examined and validated by Schlatter [104] for temporal and spatial transition of channel flow. In the light of the findings in [104], the use of subgrid scale models which add viscosity to the mean flow – especially in laminar regions as does the standard Smagorinsky model – should be avoided. Such a model would introduce unacceptable errors in terms of boundary layer thickness, shape of the boundary layer profile and the associated instability modes and can even cause relaminarization. Dynamic approaches adjust the strength of the model to the local flow situation which promises that laminar or transitional regions are preserved from a deterioration through excess model viscosity. However, they are difficult to control and lack robustness. For instance, the model constant of the dynamic Smagorinsky model is typically averaged in space in homogeneous directions, which limits the applicability to general three dimensional flows. Since these numerical and modeling-associated issues are circumvented altogether, implicit or no-model LES is highly attractive for transitional flows.

## 2.4 Numerics

The above requirements for LES and DNS of transitional flows on the one hand and those for the resolution of acoustic wave propagation on the other hand both imply that a numerical scheme of high or spectral order of accuracy should be used in order to keep numerical dispersion and dissipation errors low.

A wide range of different high accuracy schemes has been employed in LES and DNS with success, among which are high order differencing [15, 83, 112] and spectral Fourier and collocation methods [88]. Thanks to their high accuracy, compact finite difference schemes [6, 60, 72] are a typical choice for direct noise computations. All of the above methods are based on a structured representation of the solution and are typically implemented in highly specialized simulation codes for rather simple geometrical setups such as periodic boxes, jets, channels, pipes, flat plates or at most cylinders and airfoils.

In contrast, the class of high order finite element methods decomposes the computational domain into grid cells or elements, which in principle can be arranged for the discretization of arbitrary domains. This class includes continuous [29, 58] and discontinuous [41, 66] Galerkin methods (CG and DG). CG methods are employed for incompressible flow problems while DG methods are often preferred for compressible flows. The spectral difference [110] and flux reconstruction [52] methods are similar schemes closely related to the DG method. Their high order accuracy is retained by employing a local high order basis to represent the solution within each element. DG methods therefore combine high accuracy with geometrical flexibility.

Various DG schemes with different basis functions and a variety of element shapes have been proposed for the solution of the compressible Navier-Stokes equations [9, 35, 41]. In this work we employ the high order discontinuous Galerkin spectral element method (DGSEM) [66]. For DGSEM, a particular set of implementation choices, including a tensor product basis on hexahedral elements, lead to a highly accurate and efficient scheme that is both free-stream preserving and conservative at the discrete level.

A two-dimensional analysis of the dispersion and dissipation errors of DG schemes conducted by Hu et al. [47] showed (i) that the anisotropy of these errors is significantly lower when using a tensor product basis compared to full-order bases on triangles and quadrilaterals and (ii) that regarding the amplitude and phase errors, the one-dimensional case represents the worst case of all propagation angles in 2D. The one-dimensional numerical dissipation and dispersion properties of the DGSEM were analyzed by Gassner and Kopriva [36]. They found the properties comparable to the ones of a state of the art compact finite difference scheme [6] at the same order of convergence. The capabilities of the DGSEM for simulations of transitional and turbulent flows at moderate Reynolds numbers in an under-resolved, i.e. no-model LES setting have been demonstrated in [12, 13, 30] and for CAA applications for instance in [27, 31].

Besides accuracy, numerical schemes should be assessed in terms of computational efficiency. High order schemes require less grid points to reach a given error tolerance compared to low order methods but they generally imply higher computational effort per grid point and stronger coupling through larger stencils. Due to the tremendous effort of CFD problems, efficient parallelization of the simulation is of prime interest. Larsson and Wang [70] expect continuation of the trend in high performance computing architectures towards massively parallel systems, making larger and more realistic applications accessible for scale-resolving simulations in the future. The popular compact differencing and filtering schemes as well as Fourier bases all impose non-local coupling, compromising or at least challenging computational efficiency in a massively parallel setup. In contrast, the solution update of a DG scheme only requires information from direct neighboring elements regardless of the chosen approximation order, which marks a distinct advantage of these methods for future large scale simulations. Regarding single-core efficiency, the DGSEM is known to require significantly less operations than DG methods on e.g. tetrahedra [43].

## 2.5 Current Implementation

As detailed in the preceding section, the DGSEM represents an attractive method of choice for highly accurate, scale-resolving simulations of fluid flow and wave propagation. In the following, we outline the steps in the derivation of the method, our implementation and the extension to curved, non-conforming interfaces in three space dimensions. More detailed discussions are given in Hindenlang [43,45], Kopriva and Gassner [66] and the textbook by Kopriva [65].

### 2.5.1 Polynomial bases and the projection operator

Most DG schemes build upon a polynomial representation of the approximate solution within the elements and a projection operation to obtain its coefficients. We write the approximation $f_h(x)$ to the function $f(x)$ as a polynomial expansion

$$f(x) \approx f_h(x) = \sum_{i=0}^{N} \tilde{f}_i \phi_i^N(x) \tag{2.6}$$

in terms of an arbitrary basis $\phi_i^N(x)$ that spans the space of polynomials of degree $N$, $\mathbb{P}^N$. The projection operator onto the test function $\phi(x)$ can be defined for all square integrable functions $f(x), \phi(x) \in \mathbb{L}_2(C)$ by requiring

$$\int_C f_h(x)\phi(x)\,dx = \int_C f(x)\phi(x)\,dx. \tag{2.7}$$

Setting the test function to each of the basis functions $\phi_j^N(x)$ yields $N+1$ equations

$$\int_C f_h(x)\phi_j^N(x)\,dx = \int_C f(x)\phi_j^N(x)\,dx, \qquad j = 0, ..., N. \tag{2.8}$$

Inserting the polynomial expansion $f_h(x)$ from (2.6) delivers a linear equation system

$$\sum_{i=0}^{N} \tilde{f}_i \int_C \phi_i^N(x)\phi_j^N(x)\,dx = \int_C f(x)\phi_j^N(x)\,dx, \qquad j = 0, ..., N, \tag{2.9}$$

that can be solved for the unknown coefficients $\tilde{f}_i$.
Of course, there are other ways to determine the coefficients of the expansion (2.6), for instance through interpolation of $f(x)$, leading to a different numerical scheme with different properties. The appeal of projection is that the numerical

error becomes orthogonal to the chosen approximation space. Thus if $f_h(x) \in \mathbb{P}^N$, the lowest order in a polynomial expansion of the error is $N+1$. Equivalently, the projection operator delivers the best approximation $f_h(x) \in \mathbb{P}^N$ to $f(x)$ in the least squares sense [65], i.e. it minimizes the $\mathbb{L}_2$ norm of the error

$$\int_C |f(x) - f_h(x)|^2 \, dx. \tag{2.10}$$

### 2.5.2 Transformation of the equations

The Navier-Stokes equations (2.1) are represented by a general conservation law

$$U_t + \vec{\nabla}_x \cdot \vec{F}(U, \vec{\nabla}_x U) = 0. \tag{2.11}$$

Note that in the following, we understand $U$ as a *scalar* representative for any of the components of the state vector and $\vec{F}(U, \vec{\nabla}_x U)$ as the flux vector belonging to that component.

The computational domain $\Omega$ is subdivided in non-overlapping hexahedral elements. Each element is mapped onto a reference element $E = [-1, 1]^3$ by the transformation $\vec{x}(\vec{\xi})$, where $\vec{x} = (x, y, z)^T = (x_1, x_2, x_3)^T$ and $\vec{\xi} = (\xi, \eta, \zeta)^T = (\xi^1, \xi^2, \xi^3)^T$. Under this transformation, the system (2.11) reads

$$U_t + \frac{1}{J} \vec{\nabla}_\xi \cdot \vec{\mathcal{F}}(U, \vec{\nabla}_x U) = 0, \tag{2.12}$$

where we introduced $\vec{\nabla}_\xi = (\partial/\partial\xi, \partial/\partial\eta, \partial/\partial\zeta)^T$. The so-called contra-variant fluxes $\vec{\mathcal{F}}$ are computed from the physical flux $\vec{F}$

$$\mathcal{F}^i = J\vec{a}^i \cdot \vec{F} = \sum_{n=1}^{3} J a_n^i F_n. \tag{2.13}$$

Here, the contra-variant basis vectors multiplied by the Jacobian of the transformation are defined as

$$J\vec{a}^i = \frac{\partial \vec{x}}{\partial \xi^j} \times \frac{\partial \vec{x}}{\partial \xi^k}, \qquad (i, j, k) \quad \text{cyclic} \tag{2.14}$$

and 'cyclic' implies either $(i, j, k) = (1, 2, 3)$, $(2, 3, 1)$ or $(3, 1, 2)$. The determinant of the mapping is written as

$$J = \vec{a}_1 \cdot (\vec{a}_2 \times \vec{a}_3). \tag{2.15}$$

Kopriva [64] showed how to approximate the contra-variant basis in order to achieve discrete *free-stream preservation* under the transformation. This is the property that a spatially constant solution $U =$ const. remains constant for all times, since $\vec{F}(U) =$ const. and $\vec{\nabla}_x \cdot \vec{F}(U) = 0$. Besides conservation, this property is crucial for multi-scale simulations, where low amplitude components such as acoustics are easily overshadowed by spurious errors induced by the more energetic unsteady hydrodynamic components. In Kopriva's variant the contra-variant basis vectors are computed in a curl form

$$Ja_n^i = -\hat{x}_i \cdot \vec{\nabla}_\xi \times \left( I^N (x_l \vec{\nabla}_\xi x_m) \right), \qquad (n, m, l) \quad \text{cyclic.} \tag{2.16}$$

leading to discretely divergence-free metrics. Here we denote by $I^N(\cdot)$ the polynomial interpolation operator of order $N$ and by $\hat{x}_i$ the unit vector in Cartesian space.

### 2.5.3 Variational formulation

The variational form of the conservation law (2.12) is written by projection of the transformed conservation law (2.12) onto a test function $\phi(\vec{\xi})$ on the reference element $E$

$$\int_E \left( JU_t + \vec{\nabla}_\xi \cdot \vec{\mathcal{F}} \right) \phi(\vec{\xi})\, d\vec{\xi} = 0. \tag{2.17}$$

Note that multiplying the transformed equation by $J$ before integrating in reference space is consistent with conservation in physical space, since $d\vec{x} = Jd\vec{\xi}$. This is immediately seen when setting the test function $\phi(\vec{\xi}) = 1$. The interior and boundary contributions are separated after an integration by parts and we obtain the *weak form*

$$\int_E JU_t \phi \, d\vec{\xi} + \int_{\partial E} \left( \vec{\mathcal{F}} \cdot \hat{n} \right)^* \phi(\vec{\xi})\, dS - \int_E \vec{\mathcal{F}} \cdot \vec{\nabla}_\xi \phi(\vec{\xi})\, d\vec{\xi} = 0, \tag{2.18}$$

where $\hat{n}$ identifies the outward pointing unit normal vector of the reference element. The transformed surface normal flux appearing in the second term is related to the physical flux by

$$(\vec{\mathcal{F}} \cdot \hat{n})^* := \mathcal{F}^* = (\vec{F}^* \cdot \vec{n})\hat{s} \tag{2.19}$$

with the surface element $\hat{s}$ and the outward pointing normal vector in physical space, which read as $\hat{s} = |J\vec{a}^1(1, \xi^2, \xi^3)|$ and $\vec{n} = J\vec{a}^1(1, \xi^2, \xi^3)/\hat{s}$ for the $\xi^1 = 1$

surface of the reference element. We distinguish between advective and viscous fluxes as $G(U)$ and $H(U, \vec{\nabla}_x U)$, respectively, so that $(\vec{F} \cdot \vec{n})^* := F^* := G^* - H^*$. The advective part is computed as a function of the generally discontinuous state on either side of the interface

$$G^* = G^*(U^+, U^-, \vec{n}) \tag{2.20}$$

by use of a numerical flux function. Typical choices are the local Lax-Friedrich flux or the Roe and Pike Riemann solver [98], the latter has been applied throughout this work. It is worth mentioning that this surface flux is the only component of the DG operator where coupling between neighboring elements is enforced. The treatment of the viscous fluxes $H(U, \vec{\nabla}_x U)$ is described in Section 2.5.5.

### 2.5.4 DGSEM implementation

For implementation, the volume and surface integrals appearing in the weak form (2.18) are substituted with a numerical quadrature rule. Numerical integration in one space dimension is written as

$$\int_{-1}^{1} f(\xi)\, d\xi = \sum_{j=0}^{M} f(\hat{\xi}_j)\omega_j \tag{2.21}$$

with the integration points and weights $\{\hat{\xi}\}_{j=0}^{M}$ and $\{\omega\}_{j=0}^{M}$, respectively. When choosing Legendre-Gauss points, integration by (2.21) is exact for polynomial integrands of order $2M + 1$.

The solution in each element is represented by a tensor product of one-dimensional Lagrange polynomials

$$U(\vec{x}, t) \approx U_h(\vec{x}(\vec{\xi}), t) = \sum_{i,j,k=0}^{N} \hat{U}_{ijk}(t)\Psi_{ijk}^{N}(\vec{\xi}), \quad \Psi_{ijk}^{N}(\vec{\xi}) = \ell_i^N(\xi^1)\ell_j^N(\xi^2)\ell_k^N(\xi^3), \tag{2.22}$$

where

$$\ell_i^N(\xi) = \prod_{j=0; j\neq i}^{N} \frac{\xi - \xi_j}{\xi_i - \xi_j} \tag{2.23}$$

which have the property

$$\ell_i^N(\xi_j) = \delta_{ij} = \begin{cases} 1, i = j \\ 0, i \neq j \end{cases} . \tag{2.24}$$

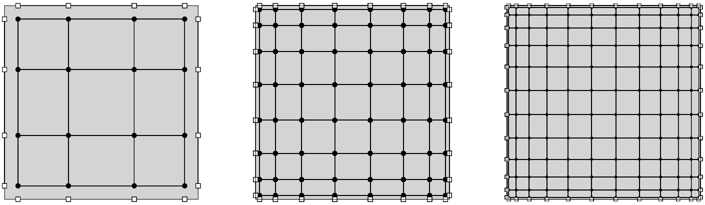

Figure 2.3: Legendre-Gauss points in the volume (filled circles) and on the surface (squares) of the reference element for $N = 3$, $N = 7$ and $N = 11$.

Thus, the degree of freedom $\hat{U}_{ijk}(t)$ represents the solution $U_h(\vec{x}(\vec{\xi}_{ijk}), t)$ at the node $\vec{\xi}_{ijk} = (\xi_i, \xi_j, \xi_k)^T$. The interpolation point distribution $\{\xi\}_{i=0}^N$ is not chosen yet. A very efficient method results if the nodes for interpolation and integration are co-located [66], i.e. $M = N$ and $\{\xi\}_{i=0}^N = \{\hat{\xi}\}_{i=0}^N$. In three spatial dimensions, the interpolation nodes $\vec{\xi}_{ijk}$ are chosen as the tensor product of the $N + 1$ Legendre-Gauss points $\{\hat{\xi}\}_{j=0}^N$, which is depicted in Fig. 2.3 for $N = 3$, $N = 7$ and $N = 11$. Two properties may be noticed: the clustering of the points towards the boundaries with increasing $N$ and that the boundaries themselves are not included.

The contra-variant volume flux in the third term of (2.18) is treated similarly

$$\mathcal{F}^m(\vec{\xi}) = \sum_{i,j,k=0}^{N} \mathcal{F}^m_{ijk} \Psi^N_{ijk}(\vec{\xi}), \qquad m = 1, 2, 3 \tag{2.25}$$

where the contra-variant flux $\mathcal{F}^m_{ijk}$ at the node is computed by (2.13) using $\hat{U}_{ijk}(t)$. The same is done for the contra-variant surface flux. For example at the $\xi^1 = +1$ surface (indicated by $\cdot|^{+\xi^1}$), we have

$$\mathcal{F}^*(\xi^2, \xi^3)\big|^{+\xi^1} = \sum_{j,k=0}^{N} \mathcal{F}^*_{jk}\big|^{+\xi^1} \ell_j(\xi^2)\ell_k(\xi^3) \tag{2.26}$$

which interpolates the flux values $\mathcal{F}^*_{jk}$ calculated by (2.19) at the corresponding surface collocation points (squares in Fig. 2.3). Note that for nonlinear functional dependencies of the flux on the solution and through possible nonlinearities in the metric terms, a truncation error in the sense of (2.10) and an additional aliasing error is introduced through the interpolation of the flux in (2.25) [66]. Based on these definitions, we can derive the discrete form of the DGSEM. Galerkin methods set the test function equal to the basis representing the solution (see (2.8)), i.e. $\phi(\vec{\xi}) = \Psi^N_{ijk}(\vec{\xi})$. Using the interpolation nodes as quadrature points (i.e. $M = N$ in (2.21)), the integral over the time derivative in the weak form (2.18) becomes

$$\sum_{\lambda,\mu,\nu=0}^{N} \left( J(\vec{\xi}_{\lambda\mu\nu}) \hat{U}_{t,\lambda\mu\nu} \Psi^N_{ijk}(\vec{\xi}_{\lambda\mu\nu})\, \omega_\lambda \omega_\mu \omega_\nu \right), \qquad i,j,k = 0,...N. \tag{2.27}$$

Due to collocation and the property (2.24) of the Lagrange interpolation function, the test function $\Psi^N_{ijk}(\vec{\xi}_{\lambda\mu\nu})$ is only non-zero where $(\lambda,\mu,\nu) = (i,j,k)$ so that only one term of the sum remains

$$J(\vec{\xi}_{ijk}) \hat{U}_{t,ijk}\, \omega_i \omega_j \omega_k, \qquad i,j,k = 0,...N. \tag{2.28}$$

Let us now concentrate on the third integral on the right-hand side of (2.18)

$$\int_E \vec{\mathcal{F}} \cdot \vec{\nabla}_\xi \phi \, d\vec{\xi} = \sum_{d=1}^{3} \int_E \mathcal{F}^d \frac{\partial \phi}{\partial \xi^d} \, d\vec{\xi}. \tag{2.29}$$

Inserting the flux (2.25) and the test function and evaluating the integral via quadrature for the first term in (2.29) gives

$$\int_E \mathcal{F}^1 \frac{\partial \phi}{\partial \xi^1} \, d\vec{\xi} = \sum_{\lambda,\mu,\nu=0}^{N} \mathcal{F}^1_{\lambda\mu\nu} \left. \frac{d\ell^N_i(\xi)}{d\xi} \right|_{\xi=\xi_\lambda} \ell^N_j(\xi_\mu) \ell^N_k(\xi_\nu)\, \omega_\lambda \omega_\mu \omega_\nu. \tag{2.30}$$

Introducing the polynomial derivative matrix $D_{ij} = \ell'^N_j(\xi_i)$ [65] and again exploiting the property (2.24) leads to

$$\int_E \mathcal{F}^1 \frac{\partial \phi}{\partial \xi^1} \, d\vec{\xi} = \sum_{\lambda=0}^{N} \mathcal{F}^1_{\lambda jk} D_{\lambda i}\, \omega_\lambda \omega_j \omega_k. \tag{2.31}$$

Using the same arguments for the remaining surface integral over $\partial E$ in (2.18) and rearranging, we arrive at the following semi-discrete form

$$\begin{aligned}\hat{U}_{t,ijk} + \frac{1}{J(\vec{\xi}_{ijk})}\Big\{ &\Big[\mathcal{F}^*_{jk}\big|^{+\xi^1}\hat{\ell}_i(1) + \mathcal{F}^*_{jk}\big|^{-\xi^1}\hat{\ell}_i(-1)\Big] + \sum_{\lambda=0}^{N}\mathcal{F}^1_{\lambda jk}\hat{D}_{i\lambda} \\ &+ \Big[\mathcal{F}^*_{ik}\big|^{+\xi^2}\hat{\ell}_j(1) + \mathcal{F}^*_{ik}\big|^{-\xi^2}\hat{\ell}_j(-1)\Big] + \sum_{\mu=0}^{N}\mathcal{F}^2_{i\mu k}\hat{D}_{j\mu} \\ &+ \Big[\mathcal{F}^*_{ij}\big|^{+\xi^3}\hat{\ell}_k(1) + \mathcal{F}^*_{ij}\big|^{-\xi^3}\hat{\ell}_k(-1)\Big] + \sum_{\nu=0}^{N}\mathcal{F}^3_{ij\nu}\hat{D}_{k\nu}\Big\} \\ &= 0, \quad i,j,k = 0,...N.\end{aligned} \tag{2.32}$$

In (2.32), we have used the definitions

$$\hat{\ell}_i(\xi) = \frac{\ell_i(\xi)}{\omega_i} \tag{2.33}$$

and

$$\hat{D}_{ij} = -D_{ji}\frac{\omega_j}{\omega_i}. \tag{2.34}$$

### 2.5.5 Approximation of the viscous fluxes

The viscous fluxes $\vec{H}(U, \vec{\nabla}_x U)$ that depend on the solution and its gradient require special treatment. We follow Bassi and Rebay [8], who chose the same discontinuous approximation space for the gradients as for the solution. In their approach, later termed BR1 scheme, the original equation (2.11) is rewritten in a system of first order equations

$$\begin{aligned} U_t + \vec{\nabla}_x \cdot \vec{F}(U, \vec{Q}) &= 0. \\ Q_d - \frac{\partial}{\partial x_d}U &= 0, \qquad d = 1,2,3. \end{aligned} \tag{2.35}$$

The auxiliary equation for $\vec{Q} \approx \vec{\nabla}_x U$ is solved in the weak form in the same way as (2.11)

$$\int_E J Q_d \phi \, d\vec{\xi} - \int_{\partial E}\Big(\vec{\mathcal{U}}_d \cdot \hat{n}\Big)^* \phi \, dS + \int_E \vec{\mathcal{U}}_d \cdot \vec{\nabla}_\xi \phi \, d\vec{\xi} = 0, \quad d = 1,2,3, \tag{2.36}$$

where $\vec{\mathcal{U}}_d = (Ja^1_d, Ja^2_d, Ja^3_d)^T U$. Like for the advective part, the surface contributions in (2.36), for instance at $\xi^1 = +1$,

$$\Big(\vec{\mathcal{U}}_d \cdot \hat{n}\Big)^*\Big|^{+\xi^1} = U^*(U^+, U^-)\, n_d \hat{s}\big|^{+\xi^1} = U^*(U^+, U^-)\; Ja^1_d\big|^{+\xi^1} \tag{2.37}$$

must be functions of the discontinuous states from both sides of the interface. The same is true for the viscous surface fluxes in the original equation $H^*$. In the BR1 scheme, they are set to

$$U^*(U^+, U^-) = \frac{1}{2}\left(U^+ + U^-\right), \tag{2.38}$$

$$H^*(U^+, U^-, Q^+, Q^-, \vec{n}) = \frac{1}{2}\left(\vec{H}(U^+, Q^+) + \vec{H}(U^-, Q^-)\right) \cdot \vec{n}. \tag{2.39}$$

This simple arithmetic mean is motivated by the diffusive nature of the operator [8]. Taking $Q_d$ in the same polynomial solution space as $U$, the discrete auxiliary equation is retrieved by replacing $U_t$ with $Q_d$, $\vec{\mathcal{F}}$ with $-\vec{\mathcal{U}}_d$ and $\mathcal{F}^*$ with $-\mathcal{U}_d^* := -(\vec{\mathcal{U}}_d \cdot \hat{n})^*$ in (2.32).
It should be mentioned that the BR1 method is formally unstable for purely elliptic problems [4]. A remedy was proposed with the BR2 scheme [10]. In practice, both schemes seem to perform similarly in terms of accuracy and stability for advection-dominated problems. The BR1 scheme was used throughout this work owing to its simplicity and due to the fact that it is free of parameters.

### 2.5.6 Non-conforming interfaces

The DGSEM is restricted to hexahedral elements, which complicates mesh generation for fully three dimensional problems compared to DG methods on e.g. tetrahedra. Algorithms for automated generation of unstructured hexahedral meshes typically only work for two-dimensional setups or extrusions thereof. In terms of local mesh refinement, flexibility can be greatly enhanced by the use of non-conforming interfaces. They allow to locally refine a conforming base mesh without affecting the remainder of the mesh. In this work, this workflow is followed using the open source library p4est [19].

#### Formulation

In the DGSEM framework, non-conforming interfaces are treated using so-called mortars [67], which are intermediate constructs between adjacent, non-conforming sides. The grid must meet certain prerequisites: (i) we only consider 4:1 and 2:1 interfaces as depicted in Fig. 2.4. This criterion is met by p4est, which through its restriction to isotropic refinement and the '2:1 balance' property only produces 4:1 interfaces in three dimensions. (ii) The polynomial representation of the edges and surfaces on both sides of an interface must be identical. If the

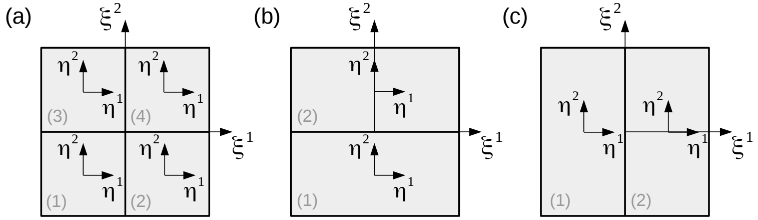

Figure 2.4: Mortar interface types: (a) 4:1, (b) and (c) 2:1.

geometry is represented with a polynomial approximation of degree $N_{\text{geo}}$, in general the polynomial space of the large side is a subset of the composite space of the adjacent small sides. Thus, the easiest way to ensure (ii) is to interpolate the polynomial mapping from the large side to the small sides.

Mortars enable the conservative transfer of fluxes between elements that share non-conforming interfaces by a three-step procedure based on projection. The procedure is schematically shown in Fig. 2.5 for the case of a 4:1 interface, and is as follows:

1. Interpolation of the solution $U(\vec{\xi})$ and the numerical gradient $\vec{Q}(\vec{\xi})$ from both sides to the mortars. As the small sides coincide with the mortars and the same interpolation nodes are chosen, this amounts to simply copying the solution to the mortar. For the large sides, we evaluate the polynomial basis at the mortar's interpolation nodes. The polynomials defined on the large face can be represented exactly on the small mortar sides.

2. Evaluation of the numerical flux on the mortars based on the solution and gradient from both sides of the interface.

$$\mathcal{F}^*_M = \left(G^*(U^+_M, U^-_M, \vec{n}) + H^*(U^+_M, U^-_M, Q^+_M, Q^-_M, \vec{n})\right) \hat{s}_M. \tag{2.40}$$

3. Projection of the flux from the mortars back to the adjacent sides. For the small sides, again the fluxes can simply be copied. For the large sides, the composite discontinuous polynomial flux interpolant of the adjacent

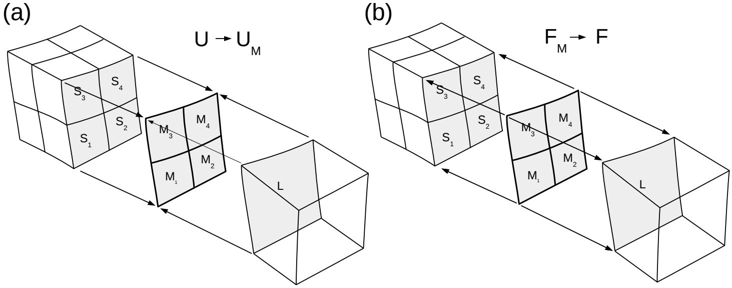

Figure 2.5: Schematic of the mortar procedure. (a) Step 1, projection of the solution $U$ to the mortars. (b) Step 3, projection of the flux from the mortars to the adjacent sides.

small sides $M_1$ through $M_4$ is projected onto the large side solution space

$$\sum_{m=1}^{4} \int_{M_m} \left( \mathcal{F}_L^*(\vec{\xi}_m(\vec{\eta})) - \beta \mathcal{F}_{M_m}^*(\vec{\eta}) \right) \ell_i(\xi_m^1(\vec{\eta}))\ell_j(\xi_m^2(\vec{\eta}))d\vec{\eta} = 0, \qquad i,j = 0, ..., N. \tag{2.41}$$

Therein, we denote by $\vec{\eta} = (\eta^1, \eta^2)^T$ the coordinates in mortar space $\vec{\eta} \in [-1, 1]^2$ as indicated in Fig. 2.4 and by $\vec{\xi}_m(\vec{\eta})$ the mapping from the mortar $M_m$ to the large side reference coordinates. The factor $\beta$ adjusts the contra-variant flux to match the surface of the large element. The surface metrics between large and small elements should only differ by the factor between their reference space sizes, i.e. for the 4:1 interface, $J\vec{a}^i|_L = 2^2 J\vec{a}^i|_{M_m}$ in the respective subspaces and thus in that case, $\beta = 4$.

This projection operation is conservative, since the local mean values of the contra-variant fluxes are preserved. It can be cast into matrix-vector form using numerical quadrature. For the calculation of the numerical gradients $\vec{Q}$ at non-conforming interfaces, the BR1 scheme outlined in Section 2.5.5 is augmented with the above procedure.

### Ensuring free-stream preservation under curved mappings

While the purpose of curved elements is the proper description of the boundary, in some important cases (e.g. boundary layers) the curved mapping has to extend several layers into the computational domain to ensure valid elements [44]. Thus, the non-conforming interface should also be applicable for arbitrarily curved sides in three space dimensions. In general, free-stream preservation can be guaranteed if the polynomial description of the surface metric $\vec{n}\hat{s} = J\vec{a}^i$ are identical on both sides of the interface between two adjacent elements. However, if the polynomial degree of the mapping $\vec{x}(\vec{\xi})$ exceeds $N/2$, the calculation of the metric terms (2.16) is not exact. For conforming interfaces, the introduced errors on both sides are the same, since the interpolation nodes on both sides of the interface coincide. In the non-conforming case they do not, hence there will be a difference between the $J\vec{a}^i$ and as a result, a violation of the free-stream preservation property. Two-dimensional meshes and extrusions thereof are important exceptions where no error is introduced in the calculation of the metric terms.

The strategy to ensure free-stream preservation for non-conforming curved interfaces implemented in this work exploits the fact that the non-conforming meshes are generated by the subdivision of a conforming base mesh. In that case, a 'global mapping' approach can be employed. The metric terms are first computed on the elements of the conforming base mesh using (2.16) and then interpolated on the subdivided 'child' elements. This ensures matching metrics across the non-conforming interfaces. However, the geometric mapping is then restricted to the approximation space of the parent elements. As a result, the interpolation error at the curved boundaries is larger than the one resulting from the usual 'local mapping' at the same polynomial degree of the mapping $N_{\text{geo}}$ defined on the child elements. For smooth geometries, provided that the number of subdivisions is not too high, this error specific to the global mapping remains small.

A comparison between the standard and the global mapping approach is given in Fig. 2.6 for the example of a non-conforming, curved mesh around a sphere. A parallel flow with $Ma = 0.3$ is initialized and enforced at all boundaries, including the sphere surface. The metric terms are calculated using (2.16) based on a polynomial mapping with $N_{\text{geo}} = 4$, the simulation is run at $N = 4$ for 2000 time steps, which here suffices to establish a time-converged global $L_2$ error. The standard approach is seen to develop severe deviations from the desired free-stream state on the order of 10%, apparently emerging at the non-conforming interfaces. In contrast, with the global mapping approach, the largest local

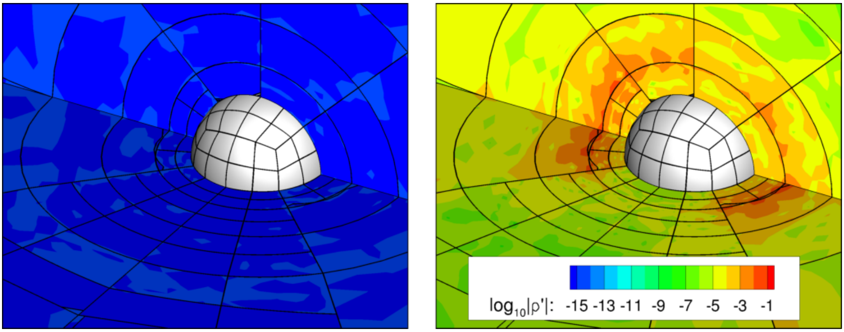

Figure 2.6: Free stream preservation test with a non-conforming curved sphere mesh with $N = 4$ and $N_{\text{geo}} = 4$. Shown is the deviation from the free-stream density $\log_{10} |\rho'/\rho_0|$ after 2000 time steps. Left: Global mapping metrics, right: local mapping metrics.

deviation in the whole computational domain is approximately $10^{-13}$. These results clearly show that free-stream preservation can be lost with curved, non-conforming and three-dimensional meshes without additional treatment. Due to the observed high magnitude of these errors, the low-amplitude acoustic field would be completely overshadowed by the numerical errors in this case.

### 2.5.7 Time discretization

The semi-discrete operator (2.32) provides an explicit expression for the time derivative $U_t$, such that the system can be advanced in time with a method of lines. Due to its accuracy and ease of implementation, we employ the explicit low storage fourth order Runge-Kutta scheme by Carpenter and Kennedy [20], if not stated otherwise. In some cases, the optimized fourth order 14 stage Runge-Kutta scheme proposed by Niegemann et al. [87] is applied, which allows a larger time step per stage.

### 2.5.8 Under-resolved simulations and stability

As pointed out in Section 2.3.2, conducting an LES means to run an under-resolved simulation. In that situation, the nonlinear terms in the governing equations can introduce aliasing errors which, depending on the severeness of under-resolution, can render the scheme unstable. Variational methods offer a natural means to remove unrepresentable scales, since the problem is stated by projection of the governing equations on the available polynomial basis. Thus, proper integration of the variational problem can eliminate the aliasing error [37, 62].

However, consistent integration comes at a high computational cost. The number of required quadrature points $M$ for a given approximation of degree $N$ is a function of the nonlinearity of the physical flux with respect to the solution. For essentially incompressible problems, $M = 3/2N$ was found sufficient by Gassner and Beck [37]. Collocation of integration and interpolation is the fundamental choice leading to the highly efficient implementation presented in Section 2.5.4, but implies $M = N$ and is therefore prone to aliasing errors. Since the efficiency of the collocation method is lost for a formulation of the variational problem with $(N+1)^3$ degrees of freedom and $(M+1)^3$ quadrature points per element, de-aliasing is carried out in an alternative manner: The collocation operator (2.32) is evaluated with $M > N$ and projected on $\mathbb{P}^N$ in each Runge-Kutta stage. This is accomplished using an element-local, modal cut-off filter as detailed in [37].

The transformed conservation law (2.12) implies that the conserved variable in reference space is the product of the Jacobian and the solution vector, $JU$. Discrete conservation is ensured by applying the projection filter to the time derivative of this quantity, $JU_t$, such that $JU_t \in \mathbb{P}^N$. Likewise, this approach is discretely free-stream preserving, since a vanishing time derivative $JU_t$ remains vanishing under the filter operation.

The de-aliasing procedure can also be applied locally and adaptively [30]. When coupled to a suitable indicator function, this technique allows to regain part of the resolution capacity of the polynomial modes $N < p \leq M$ that is otherwise lost to the de-aliasing process.

It is important to note that de-aliasing does neither guarantee numerical stability nor meaningful solutions. Under-resolved but de-aliased simulations using dissipation-free schemes (Fourier methods, central differencing) run without an SGS model or some other form of dissipation become unstable or at least produce erroneous results [68]. Depending on the degree of under-resolution, some (modeled or numerical) dissipation mechanism acting on the resolved scales is necessary to substitute the energy transfer to the subgrid scales. The DGSEM in conjunction with the de-aliasing procedure was shown to yield accurate results for a number of transitional and turbulent test cases at medium Reynolds numbers without the use of an explicit SGS model in [12]. The success of the no-model approach was attributed to the high accuracy of the scheme optimally exploiting the available degrees of freedom to resolve a large bandwidth of scales and to the numerical dissipation of the method acting predominantly on the smallest resolved scales as indicated by the analysis of the approximation properties in [36].

### 2.5.9 Boundary conditions for aeroacoustics

Appropriate farfield boundary conditions are crucial for aeroacoustics simulations. If not handled with proper care, outgoing disturbances can evoke artificial reflections at these boundaries, that may spoil the delicate acoustic field. Typically, two categories of disturbances and corresponding treatments are distinguished: low amplitude disturbances, an important example being outgoing acoustic waves and high amplitude disturbances such as the vortical wake flow convecting across the outflow boundary.

For the first type a variety of boundary conditions based on linearization and characteristic wave decomposition can be found in literature, see e.g. the review by Colonius [23] and the references therein. In the DG framework, it is common to apply boundary conditions weakly by prescribing the flux at the boundary face using a Riemann solver as $F^*_{\mathrm{BC}} = F^*(U_{\mathrm{BC}}, U^-)$. Similar to the aforementioned characteristic boundary conditions, the Roe Riemann solver used to calculate this flux is based on a characteristic wave decomposition of a linearized system. In Flad et al. [31] it was shown that weakly enforced Dirichlet boundary conditions based on the Roe Riemann solver yield similar reflection coefficients compared to classical characteristic boundary conditions.

For the category of high amplitude disturbances, the prerequisites of the linearized approach are not met. In that case, a common approach is to define a so-called sponge region in which the disturbances are attenuated before reaching the boundary. This can be achieved by grid-stretching, spatial filtering, artificial damping terms or a combination thereof.

For the current investigation, we employ a simple and robust variant. Within the sponge zone, the semi-discrete equation is augmented with a damping source term

$$U_t = R(U) - d\sigma(\vec{x})(U - U_B), \tag{2.42}$$

where $R(U)$ represents the discretized Navier-Stokes operator given by (2.32), $d$ controls the magnitude of the source term, $\sigma(\vec{x})$ denotes a ramping function that smoothly increases towards the boundary from zero to one and $U_B$ identifies the base flow towards which the solution is relaxed.

Depending on the flow problem, appropriate choices for the base flow $U_B$ may be a constant free-stream state, an analytic expression or the time-averaged solution from a previous simulation obtained on a larger domain. A generally applicable base flow can be obtained by means of a moving time-average of the solution. This is most efficiently done using the differential form of the temporal exponential filter

$$\bar{U}_t(t, \Delta) = \frac{U(t) - \bar{U}(t, \Delta)}{\Delta}, \tag{2.43}$$

which is applied during runtime to obtain the base flow $U_B = \bar{U}(t, \Delta)$ in every time step. This idea is adopted from Pruett et al. [96], who utilized the equivalence of (2.43) to the integral form of the exponential filter. As opposed to the integral form, implementation of the differential form requires minimal storage of the time history of $U$. The filter width $\Delta$ should be set to cover the largest time scales of the flow.

The above technique is robust and applicable in general configurations. For the class of aerodynamic flows that we are interested in, another important quality of the moving average base flow is the preservation of the steady potential flow field, which was demonstrated in [31]. In order to approach a solution independent of the boundary conditions, the farfield boundaries must be placed sufficiently far from the object under investigation. While coarsening of the grid towards the farfield boundary helps attenuate outgoing disturbances, grid reflections can emerge. In terms of computational cost it is not affordable to maintain a fine grid supporting the vortical or turbulent wake flow up to the outflow boundary. The proposed sponge zone can be placed close to the object. Effectively, the sponge not only prevents outflow reflection but also mitigates grid reflections.

### 2.5.10 Parallelization and performance

As noted in Section 2.4, DG methods are attractive for parallel computations as only the surface fluxes have to be exchanged between neighboring elements. A detailed description of the main parallelization building blocks of the employed simulation framework can be found in [43]. The domain decomposition is based on a space-filling curve, leading to a convenient setup of parallel simulations for varying numbers of cores. The surface fluxes are exchanged based on non-blocking MPI commands, so that local work can be performed during communication.

The thorough analysis of parallel performance on the CRAY XE6 at the High-performance Computing Center in Stuttgart (HLRS) in [43] demonstrates ideal scaling of the overall implementation on structured and unstructured meshes. Peak performance is reached for a load of about $10^3$ to $5 \cdot 10^3$ integration points per core almost independent of the chosen approximation order. In Beck [11], a comparison of the accuracy and performance with other high order codes is given. In that study, the DGSEM framework exhibits efficiency in terms of accuracy per cost similar to state of the art finite difference schemes.

## 2.6 Analysis tools

Various techniques are employed to interpret the large amount of data produced by the simulations. Besides statistical quantities such as the time average and Reynolds stresses or the discrete Fourier transform (DFT) and power spectral density (PSD) in time, additional evaluation instruments are introduced in the following. Subsection 2.6.1 gives a brief overview on the classical linear stability theory (LST) that is used to evaluate the local stability characteristics of the boundary layer or shear layer. The important global stability properties of the flow are analyzed based on a perturbation formulation (Section 2.6.2). The dynamic mode decomposition (DMD) introduced in Section 2.6.3 provides insight into the frequency content and stability of global dynamic eigenmodes obtained from a set of solution snapshots.

### 2.6.1 Classical linear stability theory

The stability of a steady base flow $U_0(\vec{x}) = (\rho_0, u_0, v_0, w_0, T_0)^T$ with respect to infinitesimal disturbances $U'(\vec{x}, t) = (\rho', u', v', w', T')^T$ can be analyzed by means of compressible linear stability theory [79]. Under the assumption that the base flow $U_0$ is a steady solution to the Navier-Stokes equations (2.1), linearization about the base flow state gives

$$U'_t = \mathcal{L}(U_0)U', \tag{2.44}$$

where $\mathcal{L}(U_0)$ represents the linearized Navier-Stokes operator. In the following we consider a wall bounded flow and a local coordinate system, where $x$ defines the streamwise direction tangential to the wall, $y$ and $z$ the wall-normal and spanwise coordinates. The local one-dimensional theory addresses base flows with only one inhomogeneous direction (the wall-normal direction $y$ for a wall-bounded flow). Thus, locally the base flow is required to satisfy $U_0(\vec{x}) \approx U_0(y)$, which implies slow variations in the streamwise and spanwise directions compared to the wall-normal direction, i.e. $\frac{\partial U_0}{\partial x} \ll \frac{\partial U_0}{\partial y}$ and $\frac{\partial U_0}{\partial z} \ll \frac{\partial U_0}{\partial y}$. Note that this step is necessary to decouple the system in the essentially homogeneous directions $x$ and $z$.

The fluctuations are assumed to take the form

$$U'(y, z, t) = \hat{U}(y) e^{i(\alpha x + \beta z - \omega t)} + c.c. \tag{2.45}$$

where *c.c* denotes the complex conjugate. Inserting this ansatz into the linearized governing equation (2.44) yields an eigenvalue problem. The complex coefficients $\alpha$, $\beta$ and $\omega$ denote the streamwise and spanwise wavenumber and the angular frequency. Thus, (2.45) describes traveling and potentially amplified or damped wave-type solutions. Here, we only consider the so-called *spatial theory*, where the angular frequency $\omega \in \mathbb{R}$ appears as a parameter and the complex wavenumber $\alpha \in \mathbb{C}$ is an eigenvalue of the system. Its imaginary part determines the growth rate of the particular mode at angular frequency $\omega$. The corresponding eigenfunction $\hat{U}(y)$ describes the shape of the disturbance mode. In the present work, we only consider streamwise traveling waves, so the spanwise wavenumber $\beta$ is set to zero.

The resulting eigenvalue problem is discretized using a Chebyshev collocation method to yield an eigenvalue problem of the size $9N^2$ for each streamwise position and each angular frequency of interest, where $N$ denotes the number of collocation points. It is solved using ARPACK routines [71]. The employed stability solver was used for instance in [107].

### 2.6.2 Global perturbation formulation

In this work, we apply the above local stability theory mainly to evaluate the amplification properties of the boundary layers and shear layers in terms of spatial growth rates and associated frequencies. This theory is limited by the assumption of two homogeneous directions, which permits wave-like solutions of the form (2.45). These limitations are overcome with global stability concepts, which have proven to be essential in the understanding of the dynamics of separated flows, bluff-body and wake flows and cavities [113]. The bi- or triglobal theory typically results in large eigenvalue problems, which at present easily become prohibitively expensive in terms of computational power and storage for arbitrary flows. For that reason, they are typically solved using matrix-free iterative Krylov techniques, see e.g. [78].

We here resort to a simple perturbation formulation of the Navier-Stokes solver as employed by Jones et al. [55, 56] or Schmidt and Rist [107]. The nonlinear

Navier-Stokes operator that governs the time evolution is written as

$$U_t = R(U). \tag{2.46}$$

Inserting a Reynolds decomposition $U = U_0 + U'$, noting that for general base flows $(U_0)_t = R(U_0) \neq 0$ and rearranging yields the operator governing the time evolution of the perturbation

$$U'_t = R(U_0 + U') - R(U_0). \tag{2.47}$$

Thus, the subtraction of the base flow time derivative is sufficient to analyze the dynamics of small perturbations to arbitrary base flows. This simple modification is suitable for any Navier-Stokes solver. A Taylor series expansion of (2.46) about $U_0$ shows that equation (2.47) approximates a formal linearization for small perturbations $U'$.

One simulation run in the perturbation formulation provides two important analyses. First, the response to an isolated small disturbance helps reveal acoustic feedback effects, see e.g. Jones et al. [55], Jones and Sandberg [56] and Pando de Fosas et al. [32]. Second, the time series is decomposed into an expansion of approximate global instability modes using the dynamic mode decomposition (DMD) introduced in the next subsection.

### 2.6.3 Dynamic mode decomposition

The DMD algorithm extracts coherent structures from a time series of snapshots. As opposed to the proper orthogonal decomposition (POD), the modes are gained based on the temporal dynamics of the time series, rather than an energy norm. Consequently, each mode is associated with a distinct frequency and temporal growth rate. The DMD relies on the time series only and therefore is not restricted to the linear regime, but may also be used for the analysis of nonlinear systems or experimental data. For flow fields obtained from both linear simulations or nonlinear ones with small perturbations, the extracted dynamic modes approximate global linear stability modes [106, 107]. The derivation follows the original contributions of Rowley et al. [100] and Schmid [106].

The starting point for the decomposition is a set of observables $\mathbf{k}_n$ at time instants $t_n = \Delta t \cdot (n-1)$, where $\Delta t$ is the sampling step. In our case, $\mathbf{k}_n$ denotes all degrees of freedom of the numerical solution at $t_n$, i.e. a vector with $M = 5n_{\mathrm{GP}}$ rows (accounting for the five state variables of the system), where $n_{\mathrm{GP}}$ denotes the number of quadrature points. The time series consisting of $N$ instants is written as the $M \times N$ matrix $\mathbf{K}_1^N$

$$\mathbf{K}_1^N = [\mathbf{k}_1, \mathbf{k}_2, \mathbf{k}_3, ..., \mathbf{k}_N]. \tag{2.48}$$

Therein, the subscript indicates the first and the superscript the last instant of the time series. It is then assumed that a linear operator $\mathbf{A}$ exists that projects a snapshot into the next one

$$\mathbf{k}_{n+1} = \mathbf{A}\mathbf{k}_n, \qquad n = 1, ..., N, \tag{2.49}$$

which is true without approximation for the case of a linear system. For our choice of input data, the operator $\mathbf{A}$ is closely related to the linearized Navier-Stokes operator (2.44). The objective is to find approximations to the eigenvalues and eigenvectors of $\mathbf{A}$, which characterize the dynamics of the system. Using (2.49), equation (2.48) can be written in terms of a Krylov sequence

$$\mathbf{K}_1^N = \left[\mathbf{k}_1, \mathbf{A}\mathbf{k}_1, \mathbf{A}^2\mathbf{k}_1, ..., \mathbf{A}^{N-1}\mathbf{k}_1\right]. \tag{2.50}$$

Krylov methods are used for instance in the solution of eigenvalue problems. While the famous Arnoldi algorithm orthonormalizes the iterates and thus requires the action of $\mathbf{A}$ on arbitrary vectors, the DMD does not require an explicit representation of the operator matrix $\mathbf{A}$. A formulation is chosen which approximates the eigenvalues and eigenvectors of $\mathbf{A}$ only based on the snapshot series. Under the assumption that for a sufficient number of snapshots, the columns of $\mathbf{K}_1^N$ become linearly dependent, the last snapshot can be expressed in terms of the preceding snapshots

$$\mathbf{k}_N = a_1\mathbf{k}_1 + a_2\mathbf{k}_2 + a_3\mathbf{k}_3 + ... + a_{N-1}\mathbf{k}_{N-1} + \mathbf{r} \tag{2.51}$$

$$= \mathbf{K}_1^{N-1}\mathbf{a} + \mathbf{r} \tag{2.52}$$

with a residual vector $\mathbf{r}$. This linear combination reflects the action of $\mathbf{A}$, which becomes apparent by considering

$$\mathbf{A}\mathbf{K}_1^{N-1} = \mathbf{K}_2^N = \mathbf{K}_1^{N-1}\mathbf{S} + \mathbf{r} \cdot \mathbf{e}_{N-1}^T \tag{2.53}$$

where $\mathbf{S}$ is a so-called companion matrix of size $(N-1) \times (N-1)$ of the form

$$\mathbf{S} = \begin{pmatrix} 0 & 0 & \cdots & 0 & a_1 \\ 1 & 0 & \cdots & 0 & a_2 \\ 0 & 1 & \cdots & 0 & a_3 \\ \vdots & & \ddots & & \vdots \\ 0 & 0 & \cdots & 1 & a_{N-1} \end{pmatrix}. \tag{2.54}$$

Rowley et al. [100] showed that the eigenvalues of the low dimensional matrix $\mathbf{S}$ then approximate the ones of $\mathbf{A}$, they are also called Ritz values. The resulting

decomposition algorithm first determines $\mathbf{a}$ by minimizing the residual $\mathbf{r}$ in (2.52). Subsequently, it computes the eigenvalues and eigenvectors of $\mathbf{S}$.
Here, the alternative algorithm proposed by Schmid [106] is chosen, which enhances numerical stability. The economy-sized singular value decomposition of the first $N-1$ snapshots reads as

$$\mathbf{K}_1^{N-1} = \mathbf{U}\mathbf{\Sigma}\mathbf{W}^H, \tag{2.55}$$

where $\mathbf{U}$ and $\mathbf{W}$ are unitary matrices of size $M \times r$ and $r \times N-1$. $\mathbf{\Sigma}$ is a diagonal matrix composed of the $r$ singular values, where $r$ indicates the rank of $\mathbf{K}_1^{N-1}$ and $(\cdot)^H$ the complex conjugate transpose. The columns of $\mathbf{U}$ represent the POD modes. In order to obtain a representation in a lower-dimensional space, the operator $\mathbf{A}$ is projected on the POD modes. Substituting (2.55) in the left hand side of (2.53) and rearranging yields

$$\tilde{\mathbf{S}} = \mathbf{U}^H\mathbf{A}\mathbf{U} = \mathbf{U}^H\mathbf{K}_2^N\mathbf{W}\mathbf{\Sigma}^{-1}, \tag{2.56}$$

where again the eigenvalues $\sigma_j$ of $\tilde{\mathbf{S}} \in \mathbb{C}^{r\times r}$ approximate the ones of $\mathbf{A}$. The corresponding eigenvectors $\mathbf{y}_j$ are transformed back to the high-dimensional space by

$$\mathbf{\Phi}_j = \mathbf{U}\mathbf{y}_j. \tag{2.57}$$

The algorithm thus consists of a singular value decomposition of the snapshot matrix $\mathbf{K}_1^{N-1}$, followed by an eigen-decomposition of the low-dimensional operator $\tilde{\mathbf{S}}$ given by (2.56).
In order to obtain the dynamic modes that fit the data sequence, we scale the eigenvectors, e.g. $\hat{\mathbf{k}}_j = \alpha_j\mathbf{\Phi}_j$. Herein, the complex coefficients $\alpha_j$ measure the magnitude and phase of the modes at $t = t_1$ and are obtained through projection of the first sample on the basis, e.g. $\sum_{j=1}^{r}\mathbf{\Phi}_j\alpha_j = \mathbf{k}_1$, which is realized efficiently on the available lower-dimensional basis

$$\mathbf{Y}\alpha = \mathbf{U}^H\mathbf{k}_1, \tag{2.58}$$

where $\mathbf{Y}$ represents the basis corresponding to the eigenvectors $\mathbf{y}_j$. The snapshot sequence may then be reconstructed from the DMD basis

$$\mathbf{k}_n \approx \sum_{j=1}^{r}\hat{\mathbf{k}}_j\sigma_j^{n-1} = \sum_{j=1}^{r}\hat{\mathbf{k}}_j e^{\omega_j t_n}, \tag{2.59}$$

where in the last step the eigenvalues are converted to the complex stability plane by $\omega_j = \log(\sigma_j)/\Delta t$. The imaginary and real part of $\omega_j$ thus indicate the mode's angular frequency and growth rate.
To summarize, the employed DMD algorithm consists of the following steps:

1. Read in the snapshots $\mathbf{k}_n$ and arrange them to the snapshot matrix $\mathbf{K}_1^N$.
2. Calculate the singular value decomposition $\mathbf{K}_1^{N-1} = \mathbf{U\Sigma W}^H$.
3. Construct $\tilde{\mathbf{S}}$ using equation (2.56).
4. Obtain the eigenvalues $\sigma_j$ and eigenvectors $\mathbf{y}_j$ of $\tilde{\mathbf{S}}$.
5. Solve for the complex coefficients $\alpha_j$ based on equation (2.58).
6. Calculate the DMD modes with $\hat{\mathbf{k}}_j = \alpha_j \mathbf{U}\mathbf{y}_j$.

## 2.7 Validation

The DGSEM framework described in Section 2.5 has been applied to a number of turbulent and transitional test cases [13, 27, 31] that also cover laminar separation, transition and turbulent reattachment in an LES setting [12]. The example discussed here addresses the simulation of an aeroacoustic feedback loop.

The NACA 0012 airfoil was subject of the majority of the studies addressing tonal airfoil self-noise [3, 24, 56, 85, 89, 93]. The two-dimensional DNS of Jones and Sandberg [56] provided numerical evidence for the presence of an acoustic feedback loop selecting discrete frequencies. A well-resolved simulation at $Ma = 0.4$ and $Re_C = 100,000$ based on the chord $C$ at an angle of attack of $\alpha = 0°$ is carried out based on their setup using a two-dimensional variant of the Flexi DGSEM code.

The C-shaped farfield boundary has a radius of $r = 7C$ while the region downstream of the airfoil extends $9C$. We choose a polynomial degree of $N = 5$ and discretize the computational domain with $40,934$ unstructured elements

| | LE current | LE ref. | TE current | TE ref. |
|---|---|---|---|---|
| $\Delta x/C$ | $4.2 \cdot 10^{-4}$ | $6.1 \cdot 10^{-4}$ | $5.3 \cdot 10^{-4}$ | $4.0 \cdot 10^{-4}$ |
| $\Delta y/C$ | $2.3 \cdot 10^{-4}$ | $3.5 \cdot 10^{-4}$ | $2.3 \cdot 10^{-4}$ | $4.0 \cdot 10^{-4}$ |

Table 2.1: Wall-tangential and wall-normal grid spacing $\Delta x$ and $\Delta y$ at the leading edge (LE) and trailing edge (TE) for the current simulation of the NACA 0012 case and reference [56].

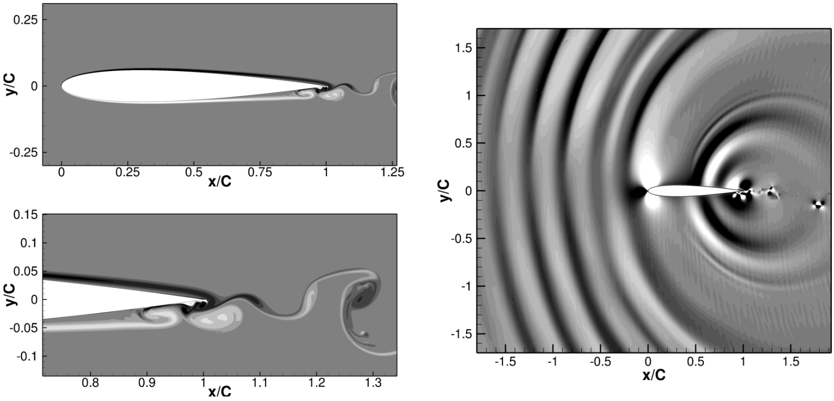

Figure 2.7: Left: Instantaneous vorticity contours over the range $\Omega_z = \pm 100 u_\infty/C$, right: Volume dilatation contours in the range $\vec{\nabla}_x \cdot \vec{v} = \pm 0.1 u_\infty/C$.

resulting in $1.47 \cdot 10^6$ degrees of freedom (DOF). De-aliasing is not necessary in this well-resolved case. The polynomial description of the boundary elements of degree $N_{\text{geo}} = 4$ ensures proper representation of the airfoil curvature. Details on the near-wall resolution of the current and the reference simulation are listed in Table 2.1. In order to account for the inner-element polynomial approximation, the grid spacings are given in terms of $\Delta x = \Delta x_{\text{Elem}}/(N+1)$, where $\Delta x_{\text{Elem}}$ denotes the element size. Weakly enforced Dirichlet boundary conditions are employed at the farfield in conjunction with the moving-average sponge zone introduced in Section 2.5.9, which is arranged as a circle around the trailing edge. The source term strength $d\sigma(\vec{x})$ is ramped from 0 to 0.5 in the range $r/C = 2$ to 6, while the temporal filter width is set to $\Delta = 2C/u_\infty$. The simulation was conducted on the CRAY XC40 Hornet cluster using 720 cores, the computational wall time amounts to 3 minutes per convective time unit $T^* = C/u_\infty$ at a time step of $\Delta t/T^* = 3.1 \cdot 10^{-5}$.

The flow topology is illustrated by instantaneous vorticity contours in Fig. 2.7 (left). The initially favorable pressure gradient undergoes a change of sign at about $x/C \approx 0.1$, which eventually leads to separation at $x/C \approx 0.6$ on both surfaces. The separated shear layer on the lower surface appears thicker

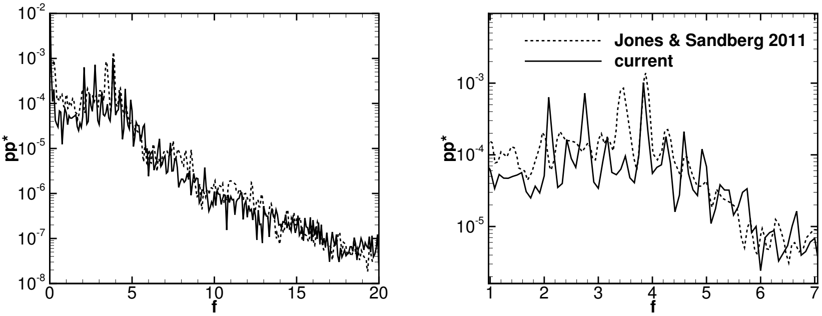

Figure 2.8: PSD of pressure at $\vec{x}/C = (0.5, 0.5)$, where the origin is placed at the leading edge of the airfoil.

than on the upper surface and there, we observe the roll-up of vortices shortly upstream of the trailing edge. However, in other instants, the shedding occurs predominantly on the upper side. Apparently, this alternation is a consequence of the nominally symmetric setup. Fig. 2.7 (right) shows the associated acoustic radiation by means of volume dilatation ($\vec{\nabla}_x \cdot \vec{v}$) contours, where the typical dipole character of trailing edge noise can be easily recognized. The sound radiated from the airfoil is superimposed by weak artificial reflections of short wavelength from downstream.

We compare the resulting acoustic signal at an observer position $0.5C$ above the airfoil with the reference in Fig. 2.8 by means of the PSD of pressure. The PSD is approximated by averaging over 5 blocks with 50% overlap and a Hanning window over a total of $36T^*$, starting from $t/T^* = 24$. The spectrum is composed of a group of discrete peaks at the lower frequency end and a broadband component decreasing towards higher frequencies. We find remarkable quantitative agreement in the main tonal noise frequency. Furthermore, the general shape of the acoustic spectrum is reproduced well. Deviations are found in the missing side peak at $fT^* \approx 3.3$ and additional lower side peaks at $fT^* \approx 2$ and 2.9 yielded by the present simulation which do not appear in the reference.

The perturbation analysis of the time-averaged flow field carried out for this reference case in [56] helped identify the presence of an acoustic feedback loop instability that apparently governs the frequency selection of the vortex shedding process. The vortex shedding was attributed to the roll-up of convective instabilities amplified in the boundary layers and separated shear layers. Scattering of these vortices at the trailing edge leads to acoustic radiation. The upstream running part of the acoustic waves reinforces instabilities of the same frequencies through receptivity of the boundary layer in the vicinity of the leading edge, so that a closed feedback loop results.

Accurate prediction of the acoustic signal is only possible if these precise hydrodynamic and acoustic processes are captured by the simulation. The close agreement of our simulation with the acoustic results of the reference demonstrate the suitability of the high order code framework for aeroacoustic feedback effects.

# 3 Simulation of a side mirror

In the preceding chapter, we have described a high-order simulation framework for the simulation of complex multi-scale flows that is validated for trailing edge noise problems and aeroacoustic feedback mechanisms. This simulation tool is now applied for the analysis of the flow around a side mirror geometry in the present chapter. Hydrodynamic and acoustic results are presented alongside with local and global stability analyses by means of classical LST and a perturbation simulation on the time-averaged flow field. Where appropriate and available, the results are compared to the corresponding experimental data. Subsequently, we discuss the obtained physical insights. The presentation closely follows the publication in Frank and Munz [33].

## 3.1 Object of investigation

Fig. 3.1 shows the side mirror being investigated. It belongs to an early development stage of the AUDI A7 (model year 2010) and was found to develop strong whistling tones at free-stream velocities of $20\,\mathrm{m\,s^{-1}}$ and above. For the present analysis we consider an isolated mirror on the wind tunnel floor, aerodynamic and acoustic interaction effects with the vehicle are neglected. This step is supported by static pressure measurements of the isolated mirror and a preliminary detached eddy simulation of the complete vehicle, which suggest that the flow field in the tonal source region is comparable. In order to further reduce the complexity of the setup, the water management groove parallel to the trailing edge has been removed in the simulation (Fig. 3.1(right)) and filled up with clay in the experiment (Fig. 3.1 (left)). Note that in the final design of this mirror, the groove was also omitted on the side surface. A critical feature of the geometry that is referred to in the following analysis is the rounded edge parallel to the trailing edge termed design edge (DE).
Werner et al. [115, 116] investigated the flow around this mirror experimentally and performed acoustic measurements in the low-turbulence, open-return Laminar Wind Tunnel (LWT) of the Institute for Aerodynamics and Gas Dynamics (IAG) of the University of Stuttgart. Again, a sharp whistling sound was observed in the reduced configuration. When plotted over the free-stream

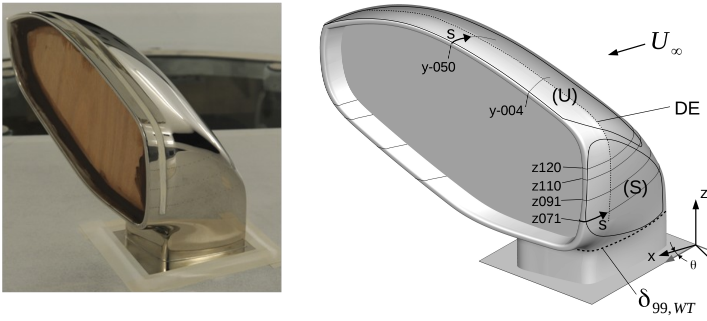

Figure 3.1: Left: mirror model in the LWT. Right: Mirror geometry. Marked areas are *(S)*: Side surface, *(U)*: Upper surface, *DE*: Design edge. The $\delta_{99,\mathrm{WT}}$ line marks the approximate thickness of the wind tunnel boundary layer in the experiments and $s$ is a body-fitted coordinate with origin at the trailing edge.

velocity, the measured acoustic spectra displayed a pattern of narrowband components exhibiting similarities to the ladder-like structure known from previous investigations at isolated airfoils, of which an overview is given in Section 1.1. In the present experiments at the mirror, boundary layer tripping clearly demonstrated that a laminar boundary layer state was necessary for tone occurrence. Furthermore, the regions of tonal noise generation could be identified through tripping as the side surface (S) and the upper surface (U), as indicated in Fig. 3.1. The observation of a ladder-like structure together with the dependency on a laminar boundary layer state suggest that the tonal components could be caused by a variant of the feedback loop model discussed in Section 1.1. The numerical results presented in the following give detailed insight into the nature of the tonal source mechanism.

## 3.2 Simulation setup

The chosen coordinate system and the free-stream flow direction for the isolated mirror configuration are depicted in Fig. 3.1. Comparison of the measured pressure distributions with a detached eddy simulation of the complete vehicle indicated that the pressure distribution on the side surface of the mirror mounted on the car could be reproduced qualitatively when the isolated mirror was rotated about $\theta = 20^\circ$ around the $z$ axis. The free-stream velocity is chosen as $u_\infty = 27.78\,\mathrm{m\,s^{-1}}$ and the yaw angle to $\theta = 20^\circ$, well within the range where tonal noise was observed in the measurements.

The free-stream temperature, pressure, density, kinematic viscosity and adiabatic coefficient are chosen as $T_\infty = 293.15\,\mathrm{K}$, $p_\infty = 10\,130\,\mathrm{Pa}$, $\rho_\infty = 1.202\,\mathrm{kg/m^3}$ and $\nu = \mu/\rho_\infty = 1.51 \times 10^{-5}\,\mathrm{m^2/s}$ and $\kappa = 1.4$. Isothermal no-slip boundary conditions are employed on the mirror surface, while at the wind tunnel floor, slip (symmetry) conditions are enforced. In the experiment, the thickness of the turbulent floor boundary layer is estimated as $\delta_{99,\mathrm{WT}} \approx 30\,\mathrm{mm}$ (see Fig. 3.1) at the mirror location. Since the tonal source regions (S) and (U) are located well outside of $\delta_{99,\mathrm{WT}}$, no effect of the floor boundary layer on the tonal noise generation at the mirror is expected. In addition, the measurements clearly indicate laminar flow on the side surface as long as no tripping device is applied. Furthermore, the inflow turbulence present in the wind tunnel is not modeled in the simulation.

At the farfield boundary, a weak Dirichlet boundary condition (Section 2.5.9) is set based on the free-stream state. The farfield boundary is realized as the combination of a spherical half-dome of radius $25L$ upstream and a half-cylinder of length $18L$ downstream. Here, the length scale $L = 0.1\,\mathrm{m}$ is chosen roughly as the length of the side surface in streamwise direction. Following the reasoning in Sections 2.3.2, 2.3.3 and 2.5.8, no explicit SGS model is employed. Possible artificial reflections through interaction of the unsteady wake with the outflow boundary are reduced to uncritical levels using the potential flow preserving sponge zone introduced in Section 2.5.9, which is applied upstream of the outflow boundary. The associated source term is ramped parallel to the free-stream velocity vector beginning at approximately $2L$ downstream of the average trailing edge $x$ coordinate of the mirror. Based on the time scale $T^* = L/u_\infty$, the damping parameter and the temporal filter width are set to $d = 0.8/T^*$ and $\Delta = 4T^*$, respectively.

## 3.3 Computational mesh

The non-conforming mesh visualized in Fig. 3.2 is generated by refining a coarse, conforming block-structured grid using p4est (cf. Section 2.5.6). The mirror surface and the downstream wake region up to the outflow boundary are refined

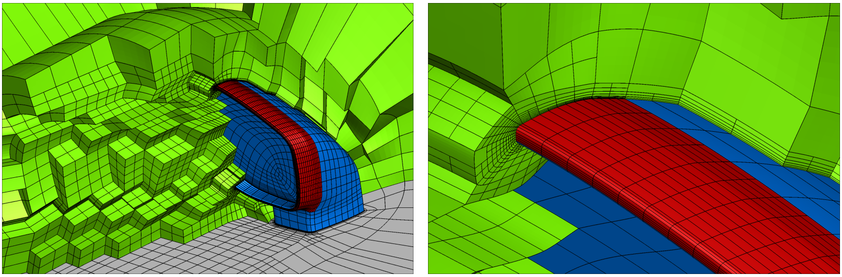

Figure 3.2: Cut view of the computational mesh.

| Case | $n_{\mathrm{GP}}$ | $\Delta t$ [s] | $\Delta y$ [mm] | $N_p(\delta_{99})$ | $\Delta x$ [mm] | $f_{4\mathrm{ppw}}$ [Hz] |
|---|---|---|---|---|---|---|
| N4M6 | $11.2 \cdot 10^6$ | $3.9 \cdot 10^{-8}$ | 0.026 | 20 | 0.6 | 6060 |
| N7M10 | $43.7 \cdot 10^6$ | $1.8 \cdot 10^{-8}$ | 0.016 | 32 | 0.38 | 9830 |

Table 3.1: Computational mesh and resolution details for two runs at polynomial degrees $N = 4$ and $N = 7$.

by one subdivision level. The area marked in red in Fig. 3.2 enclosing the design edge, the trailing edge and an overlap region downstream is refined a second time. An agglomeration approach [44] is employed to generate the curved elements. The associated mapping of polynomial degree $N_{\mathrm{geo}} = 4$ is constructed from a super-sampled version of the (unrefined) base grid. To ensure free-stream preservation, the metric terms are evaluated in the manner described in Section 2.5.6.

The sensitivity to the spatial resolution is assessed by varying the polynomial degree on the same mesh. With increasing $N$, both the spatial resolution and the accuracy of the scheme increase. Computational details on two simulations are listed in Table 3.1. As discussed in Section 2.5.8, the de-aliasing strategy employs the DGSEM operator at a polynomial degree of $M$ and restricts the solution to $\mathbb{P}^N$ with $N < M$ by use of a polynomial projection filter. In Table 3.1, the number following N denotes the polynomial degree of the approximation, whereas the number following M indicates the polynomial degree corresponding to the element-internal integration points. The resulting total number of integration points is denoted by $n_{\mathrm{GP}} = (M+1)^3 \times n_{\mathrm{Elems}}$. Note that the corresponding number of degrees of freedom is lower by the factor $\left(\frac{N+1}{M+1}\right)^3$. The wall-normal and wall-tangential grid spacings $\Delta y$ and $\Delta x$ are given with respect to the inner-element resolution using the definition in Section 2.7. They represent maximum values in the refined region on the side surface. The number of solution points in wall-normal direction within the boundary layer $N_p(\delta_{99}) = \frac{\delta_{99}}{\Delta y}(N+1)$ is used to characterize the resolution of the boundary layer profile. This number is taken at the design edge, where the local boundary layer thickness reaches its minimum, $\delta_{99} \approx 0.5\,\mathrm{mm}$. The simulations were conducted on the CRAY XC40 Hornet cluster. The used computational wall time per $T^*$ on 3288 cores for simulations N7M10 and N4M6 amounts to about 4.6 and 0.6 hours, respectively.

After initialization with free-stream conditions, the simulations are run for 30 convective time units $T^*$. In order to evaluate both the effects of the averaging window and the spatial resolution, the time-averaged pressure coefficient can be compared in Fig. 3.3 for two averaging windows ($24T^*$ and $40T^*$) and $N = 4$ and $N = 7$. The pressure coefficient is extracted along lines with $z = $ const. on the side surface and $y = $ const. on the upper surface. The local wall-tangential distance to the trailing edge is denoted $s$ as indicated in Fig. 3.1.

The results for the different averaging windows N7M10-24 and N7M10-40 are not discernible, suggesting that the chosen time frames are sufficient and a statistically steady mean flow is reached. The small differences between the two spatial resolutions N4M6 and N7M10 – which correspond almost to doubling the resolution isotropically – indicate that for the mean flow a regime of low grid dependency is reached. Based on these findings and taking into account the close agreement with the experimental static pressure measurements, the following analysis is carried out based on configuration N7M10.

We now address the capability of the simulation to resolve the instability dynamics in the source region shortly upstream of the trailing edge. As a simple lower bound for reasonably well resolved waves, we choose the 4 ppw limit. The wavelength of an instability of frequency $f$ is estimated from the time-averaged boundary layer edge velocity as $\lambda_{\min} \approx 0.4u_\delta/f$. Therein, a phase velocity of $u_{\mathrm{ph}} \approx 0.4u_\delta$ is assumed for the primary instability of a wall-bounded inflectional velocity profile [25]. Solved for the estimated frequency bound, we have

$$f_{4\mathrm{ppw}} \approx \frac{0.4u_\delta}{\lambda_{4\mathrm{ppw}}} = 0.4u_\delta \frac{N+1}{4\Delta x_{\mathrm{Elem}}}. \tag{3.1}$$

The frequencies of the estimated waves resolved with 4 ppw in the direction

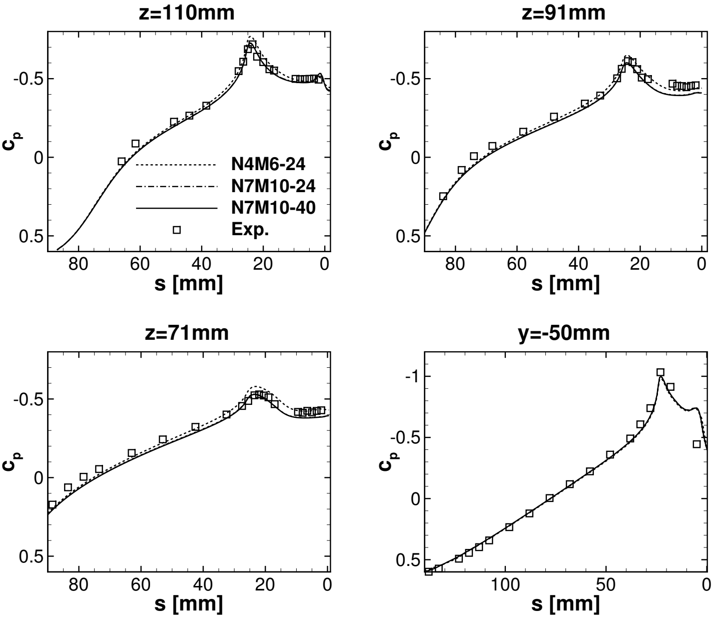

Figure 3.3: Computational and measured pressure coefficient distributions along surface lines $z = 110$, $z = 91$, $z = 71$ and $y = -50\,\mathrm{mm}$. The wall-tangential distance to the trailing edge is denotes by $s$.

tangential to the wall are listed in Table 3.1. Linear stability calculations based on the time-averaged flow field confirm the estimated wavelength $\lambda_{\min}$ as lower bound. The tonal frequencies we will present in Section 3.4.2 are well below the listed bounds for N7M10, indicating that the wavelengths of the associated instabilities are adequately resolved.

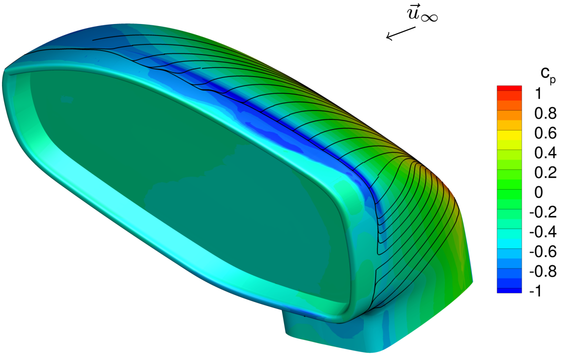

Figure 3.4: Isocontours of the time-averaged pressure coefficient and surface streamlines based on wall friction.

## 3.4 Simulation results

### 3.4.1 Time-averaged flow field

The mean flow pattern in the near-wall region is characterized by means of pressure coefficient contours on the mirror surface and surface streamlines based on the skin friction in Fig. 3.4. On the side surface, the DE is located about 25 mm upstream of the trailing edge. The surface streamlines indicate boundary layer separation shortly downstream of the DE induced by a pressure rise along the entire trailing edge. This pressure rise is also clearly noticeable in Fig. 3.3 and follows the suction peak caused by the strong localized turning at the DE. Towards the lower part of the side surface, the DE becomes gradually less pronounced, which apparently leads to a weaker suction peak and a downstream shift of the separation point. The flow exhibits a defined separation line oriented along the DE except for the region at the outer end of the mirror.

The experiments already indicated that one of the tonal noise sources is located at the side surface. Particle image velocimetry (PIV) data of the near wall region is available at the $z = 110$ mm cut (reference in Fig. 3.1) and can be compared to the computational results in Fig. 3.5. The experimental (a) and computational (b) mean velocity magnitude distributions show a thin boundary layer of about

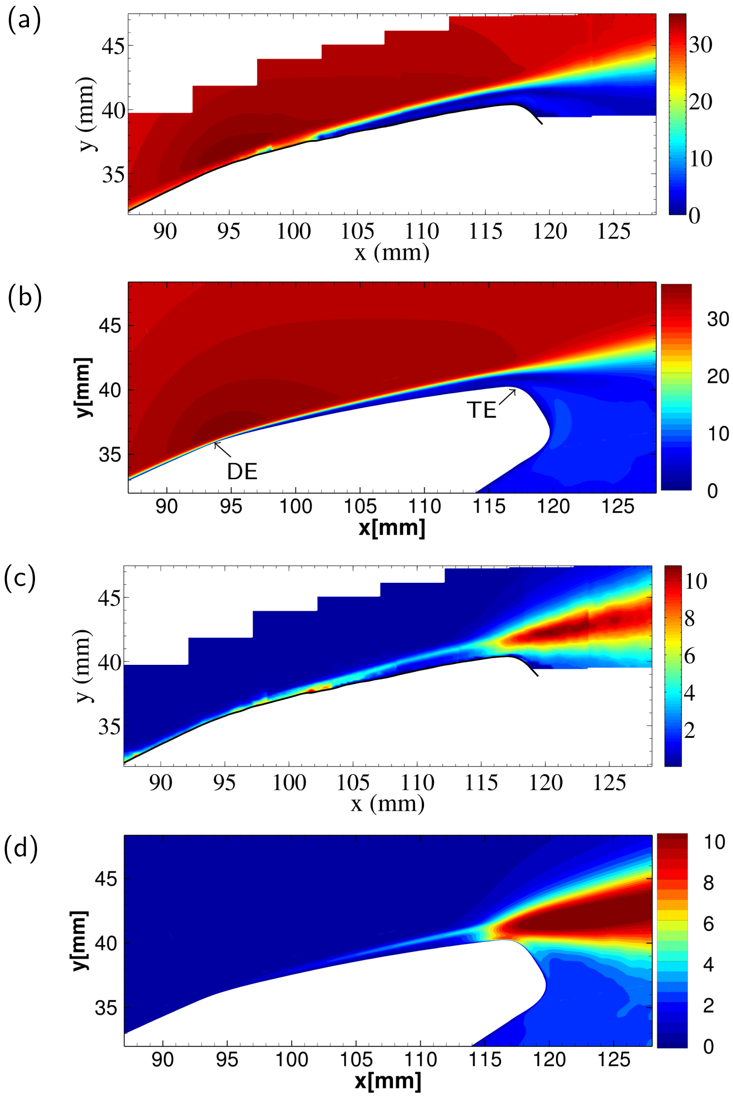

Figure 3.5: Comparison of PIV data (a,c) with the simulation results (b,d) in the $z = 110\,\mathrm{mm}$ cut. (a,b): Time-averaged velocity magnitude $\langle \vec{v} \cdot \vec{v} \rangle^{1/2}$, (c,d): RMS velocity fluctuations $\langle \vec{v}' \cdot \vec{v}' \rangle^{1/2}$, both in $\mathrm{m\,s^{-1}}$.

$\delta_{99} \approx 0.6\,\mathrm{mm}$ for the computational case. As a result of separation shortly downstream of the DE, the boundary layer begins to widen there, consistent with the pressure coefficient in Fig. 3.3. We notice good agreement with the PIV data in terms of the spreading rate and separation angle of the shear layer. The RMS of the velocity fluctuations plotted in Fig. 3.5 (c) and (d) shows that the flow is essentially steady and laminar until close to the trailing edge. From that position, strong fluctuations emerge in a qualitatively similar manner in PIV and simulation. Referring back to Fig. 3.5 (a) and (b), this onset of energetic fluctuations is accompanied with a significant thickening of the shear layer beginning at the trailing edge. Upstream, weak fluctuations can be observed along a thin line which follows the inflection point of the shear layer, suggesting the occurrence of flapping of the separated region at low frequency. The measurement artifacts in the early shear layer visible in the PIV data can be attributed to the seeding material partly deposited on the portion of the surface between the evaluation slice and the camera position.

A more quantitative analysis is accomplished by comparing the boundary layer profiles on the side surface at $z = 110$ and $z = 120\,\mathrm{mm}$ with the corresponding hotwire measurements in Fig. 3.6. Due to the experimental difficulty to accurately determine the boundary layer thickness for such a thin boundary layer, the measured profiles are shifted in the wall-normal direction to match the boundary layer thickness from the simulation. However, shifting was applied only within reasonable limits of at most $\pm 0.05\,\mathrm{mm}$, a bound based on experience with the hotwire facility used in the LWT. Due to the use of a single-wire probe, the sign of the measured signal is lost so that flow reversal cannot be detected. Consequently, the backflow region is not captured properly. Bearing that in mind, a satisfying match between the measured and computed profiles can be noticed.

The first position at $z = 110\,\mathrm{mm}$ is located close to the DE with $s_{\mathrm{DE}} = 24.7\,\mathrm{mm}$, which we define as the position of the local surface curvature maximum. However, the exact definition of the TE is somewhat arbitrary due to the rounded design. Between $s = 25\,\mathrm{mm}$ and the point of separation at 19.58 mm, the boundary layer profile becomes inflectional. At the following downstream positions, we notice that the inflection point moves outwards, up to the last position as the shear layer commences to spread. Furthermore, only a small amount of mean backflow is apparent. The reverse flow levels stay below $0.03u_\delta$ until close to the trailing edge ($0.1u_\delta$ at $s = 3.47\,\mathrm{mm}$). Nash et al. [85] found in their measurements at the NACA 0012 airfoil that the cases with tonal noise generation are associated with comparatively low reverse flow levels ($< 0.02u_\delta$) in the corresponding source regions, which is consistent with the DNS results

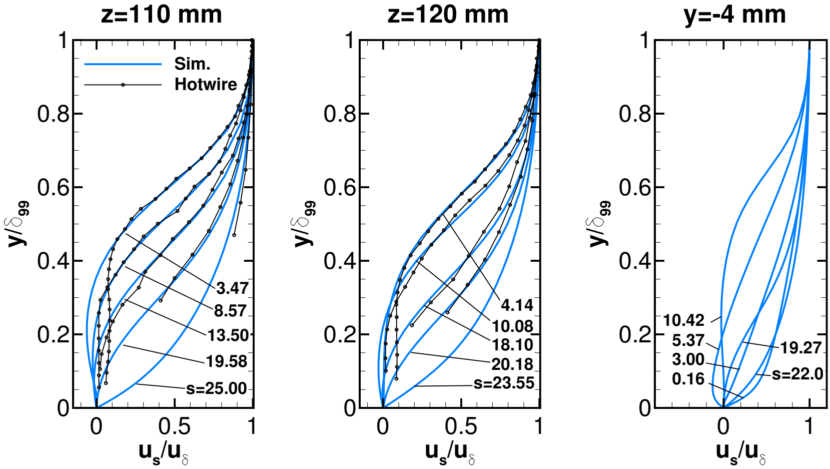

Figure 3.6: Time-averaged profiles of wall-tangential velocity $u_s/u_\delta$ plotted over $y/\delta_{99}$ from LES and hotwire measurements. The streamwise position is marked with the wall-tangential distance to the trailing edge, $s$.

reported by Desquesnes et al. [24]. The amplification of instabilities would then be driven by the inflectional velocity profiles and likely be of convective nature. The occurrence of absolute instabilities is typically associated with larger reverse flow levels in the range of $\geq 0.15 u_\delta$ [2]. Thus, the boundary layer state in the critical regions of the mirror surface is consistent with descriptions in previous studies in the case of tonal noise generation. The same observations and conclusions can be drawn for the profiles at $z = 120\,\text{mm}$.

In the experiments, a tonal noise source was also localized on the upper surface. The following section demonstrates that this is also true for the computation. Hence, the boundary layer state in the associated region is characterized in the rightmost panel of Fig. 3.6. The velocity profiles are extracted along a cut approximately following the local streamlines that reach the trailing edge at $y = -4\,\text{mm}$, which is indicated in Fig. 3.1. Similar to the near wall flow at the side surface, we observe a rapid change from a stable laminar boundary layer profile to an inflectional one induced by the DE, leading to separation within less than 3 mm from $s = 22\,\text{mm}$ to 19.27 mm. However, in contrast to the side surface where the shear layer remains separated, here the inflection point moves back towards the wall with decreasing $s$, eventually leading to reattachment.

### 3.4.2 Acoustic emissions and source identification

The preceding section established the flow conditions in the critical regions and validated the simulation in terms of mean flow quantities through comparisons with measured data. Now we turn to the radiated acoustics and the localization of the tonal noise sources. The pressure signal is sampled at a rate of 44.1 kHz over $45T^*$ or 0.162 s on a spherical array of $109 \times 27$ probes centered around the mirror with $r = 500\,\mathrm{mm}$. Subsequently, the PSD is computed using blocks with 2048 samples and 50% overlap in conjunction with a Hanning window to reduce spectral leakage. In order to characterize the spatial distribution of the acoustic field, contours of the sound pressure level (SPL) of selected frequencies and the overall SPL are plotted on the evaluation sphere in Fig. 3.7. The footprint of the wake manifests as a high amplitude spot downstream of the mirror at all shown frequencies, but can be clearly distinguished from the remainder of the field. For each frequency, a complex wave pattern emerges due to the scattering of the emitted sound at the mirror housing and the wind tunnel floor. For $f = 2857\,\mathrm{Hz}$, strong radiation in the lateral and upstream direction can be found, whereas for $f = 3544\,\mathrm{Hz}$ and 4367 Hz, the dominant contribution is directed mainly above the mirror. Also notice the decreasing length scale of the wave structures with increasing frequency. Based on this analysis, we can expect that the frequency spectra vary significantly with the probe position.

For that reason, the PSD of pressure is plotted for two probe positions in Fig. 3.8, aiming at capturing the acoustic emission from the side surface at Pos. 1 and those from the upper surface at Pos. 2, indicated in Fig. 3.7. Note that Pos. 1 is also chosen to match the inflow microphone position in the measurements. Both probes are located on the evaluation sphere, their vertical positions are $z = 270$ and $z = 500\,\mathrm{mm}$ above the floor for Pos. 1 and Pos. 2, respectively.

Some remarks on the experimental setup are necessary before discussing the simulation results. In contrast to the simulation setup, where free field conditions are approximated, the measurements were conducted in a closed rectangular test-section with a cross section of $0.73 \times 2.73\,\mathrm{m}^2$. It is clear that the scattering in the duct significantly affects the acoustic field. In addition to the different sound propagation, the transition locations and turbulence intensities in the parts of the flow around the mirror emitting the relevant broadband components cannot be guaranteed to match experimental ones. Finally, the background noise of the wind tunnel is not captured in the simulation. Therefore, we

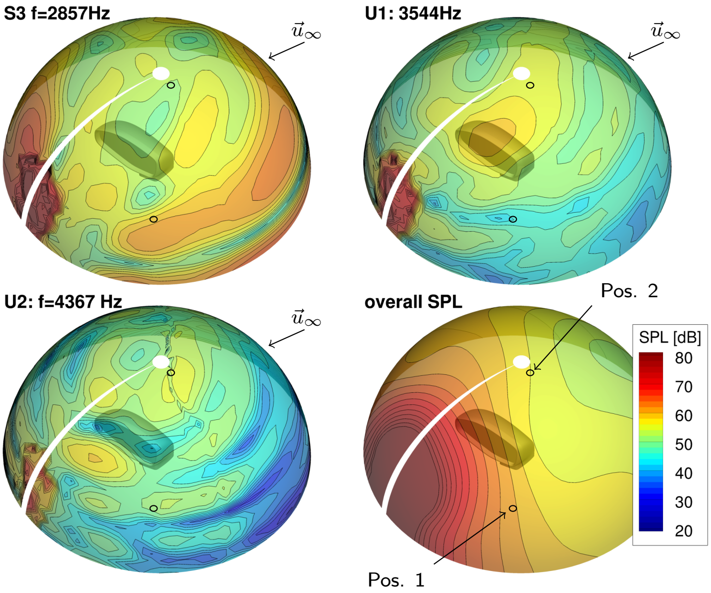

Figure 3.7: SPL for selected frequencies and overall SPL (bottom right) on a spherical evaluation surface of $r = 500\,\mathrm{mm}$ placed around the mirror.

can only compare tonal noise frequencies between experiment and simulation, clear statements regarding the broadband noise spectra or the precise spatial amplitude distributions of the tonal modes are not possible.

The computational spectrum at Pos. 1 is composed of an evenly decaying broadband part and two distinct tonal peaks at approximately 2860 Hz (S3) and 4380 Hz (U2). The radiation patterns in Fig. 3.7 suggest that the dominant source for S3 is located at the side surface, while radiation at U2 is associated with the upper surface. This notion will be confirmed by the following analysis of the wall pressure spectra. The computational spectrum does not exhibit the experimental peaks at about 3500 Hz and 5000 Hz, which are radiated from the side surface and the upper surface, respectively. However, a closer analysis of the measured signal revealed that tonal modes belonging to the side surface can

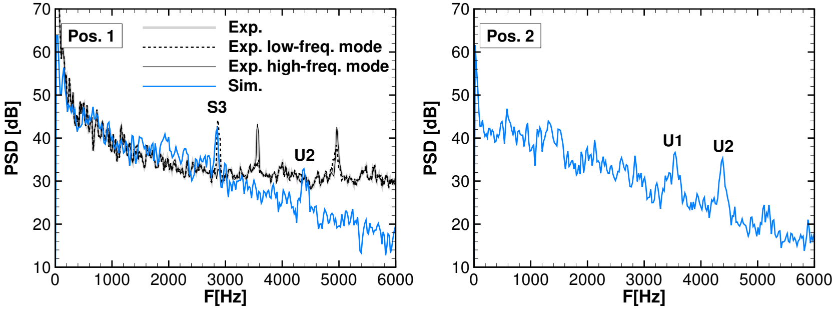

Figure 3.8: PSD of pressure at two positions outside of the unsteady hydrodynamic field. The experimental low-freq. mode and high-freq. mode datasets are obtained via conditional averaging of the spectra. PSD reference value: $4 \cdot 10^{-10}\text{Pa}^2/\text{Hz}$.

show an alternating behavior. Short-time spectra of the measured signal at Pos. 1 plotted over time showed that two modes at 2900 Hz and 3500 Hz alternate on a time scale of 0.1 to several seconds in an irregular fashion, only one of them being active at the same time. The experimental spectrum is thus the result of averaging about the associated periods. In Fig. 3.8, two experimental spectra obtained by averaging the time periods corresponding to each mode are plotted for comparison. Notice how these conditional spectra only differ notably from the measured long-time spectrum around the tonal peaks. This analysis reveals a close match between the measured low frequency mode (2900 Hz) and the computational side surface mode S3. Apparently, the simulation predicts a state where the lower of the two modes is dominant. While the precise reason for the alternation in the experiment is unknown, Werner et al. [116] were able to trigger a mode with loudspeaker forcing, indicating a high sensitivity to environmental disturbances of the flow in the experimental setup, which are practically absent in the simulation. Furthermore, the averaging time window used in the simulations was significantly shorter than the observed alternation periods.

At Pos. 2, the computational data exhibits two tones at 3550 Hz (U1) and 4380 Hz (U2), which originate at the upper surface. The latter tone is also observed at Pos. 1, while the first is not, which can be explained by referring to Fig. 3.7: Pos. 1 lies within a shadowed region regarding the acoustic propagation

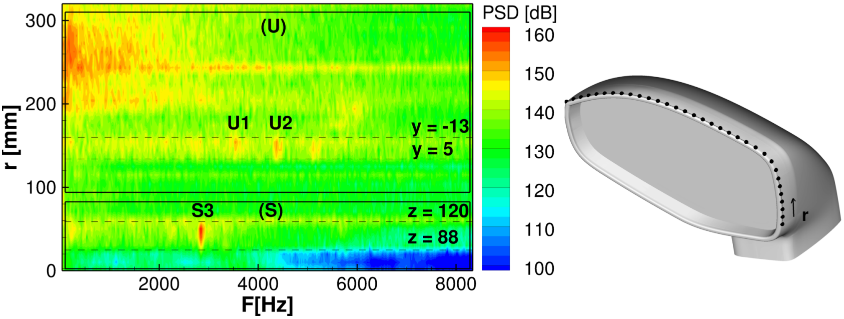

Figure 3.9: PSD of the wall pressure fluctuations along the coordinate $r$ at the trailing edge. PSD reference value: $4 \cdot 10^{-10}\text{Pa}^2/\text{Hz}$.

of U1. The experimental spectrum at Pos. 1 only exhibits a single peak radiated from the upper surface, which has a significantly higher frequency of about 5000 Hz (Fig. 3.8 (left)). An indication for a tone of a similar frequency in the simulation is found in the weak trace of a peak at about 5000 Hz in the computational data at Pos. 2, which is generated at the upper surface. Although shear layer instabilities of this frequency should be resolved with significantly more than 4 ppw, the dominance of the two lower tones might be a result of insufficient resolution.

The source positions of particular tonal components in the acoustic spectrum are obtained in the following analysis. In the experiment, a beamforming algorithm using a linear wall-mounted microphone array identified the dominant noise sources in the vicinity of the trailing edge of the mirror, indicating a noise generation mechanism similar to airfoil trailing edge noise. In Fig. 3.9 (left), we evaluate the wall pressure fluctuation spectra at the trailing edge along the coordinate $r$ depicted in Fig. 3.9 (right). The PSD is calculated using 1024 samples per block over $28T^*$, while the other parameters remain unchanged. On both the side surface and the upper surface, we find a region with narrowband frequency content. Specifically, the side surface features the expected peak at approx. 2860 Hz corresponding to S3, whereas on the upper surface multiple additional narrowband features are visible. Among these features we recognize U1, U2 and the weak trace at 5000 Hz. Thus, each tone observed in the acoustics spectra in Fig. 3.8 has a counterpart in the wall pressure spectrum. The various tonal noise components therefore originate from the respective hydrodynamic fluctuations at the trailing edge.

### 3.4.3 Unsteady flow field

The previous subsection connected wall pressure fluctuations in specific regions on the side and upper surface near the trailing edge with the generation of various tonal peaks in the acoustic spectrum. In order to characterize the unsteady flow inducing these pressure fluctuations, we visualize the transitional and turbulent flow by means of isosurfaces of the $Q$ criterion colored by velocity magnitude in Fig. 3.10. The most upstream unsteady vortical structures appear between the DE and the trailing edge over the whole mirror housing. Towards the corner region between side and upper surface, their onset is shifted upstream. On the side surface, a regular pattern of spanwise oriented rollers emerges shortly upstream of the trailing edge. An animation of the $Q$ isosurfaces shows that the regularity of these structures is a robust flow feature.
To evaluate the frequency associated with these coherent structures, a discrete temporal Fourier transform of the flow field is performed on the computational grid using 225 snapshots with a sampling frequency of $50/T^*$ or 13.9 kHz. The resulting time window covers $4.5T^*$ or about 46 periods of the tonal frequency

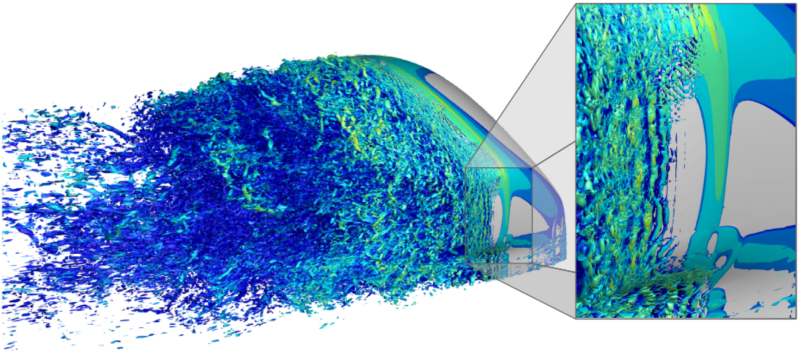

Figure 3.10: Vortical structures at a flow field snapshot visualized by isosurfaces of $Q = 100(u_\infty/L)^2$ colored with velocity magnitude.

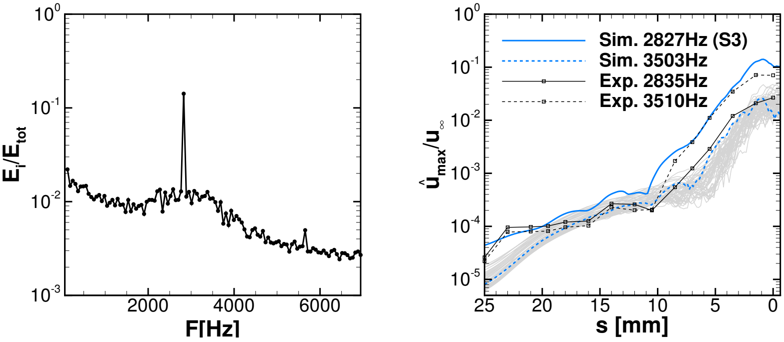

Figure 3.11: Left: Spectrum of the integral kinetic energy on an evaluation surface at the trailing edge. Right: Spatial development of the local maximum in the wall-tangential velocity $\hat{u}_{\max}/u_\infty$ for selected modes from the simulation and hotwire measurements at $z = 110\,\mathrm{mm}$. The light gray shaded lines represent computational modes in the band $2000\,\mathrm{Hz} \leq f \leq 4000\,\mathrm{Hz}$.

$f_{S3}$. The kinetic energy per unit mass $\frac{1}{2}\hat{\vec{v}} \cdot \hat{\vec{v}}$ of each Fourier mode is measured on an integration surface normal to the mirror housing, which is oriented along the $r$ coordinate in Fig. 3.9 (right). Along the wall-tangential direction, the surface ranges from $z = 50$ to $z = 140\,\mathrm{mm}$, whereas in the wall-normal direction the limit is chosen as $\approx 30\delta_{99}$. Fig. 3.11 (left) shows the resulting spectrum of integral kinetic energy on the surface normalized by the total fluctuation energy, where a sharp peak at $2827\,\mathrm{Hz} \approx f_{S3}$ is retrieved. The small difference in frequency is attributed to the different sizes of the time intervals employed for the DFT and the PSD in Fig. 3.8.

The inflectional velocity profiles found in Section 3.4.1 hint at an inviscid instability driving these fluctuations. Each amplified mode should exhibit exponential growth along the streamlines in the case of a convective instability. The streamlines at the side surface in Fig. 3.4 are found to be oriented parallel to the wind tunnel floor in good approximation. It is then appropriate to evaluate the spatial development of the fluctuations along a $z = \text{const.}$ cut, which we choose as $z = 110\,\mathrm{mm}$ in Fig. 3.11 (right). The plot results from taking the wall-normal maximum of the wall-tangential velocity fluctuation component $\hat{u}_{\max}/u_\infty$ at each streamwise position $s$ for the computational data and for the hotwire data in the experimental case. The development of the dominant computational mode $S3$ and the dominant experimental one ($f = 3510\,\mathrm{Hz}$) can be compared to the selected modes at similar frequencies and to computational modes from the surrounding band $2000\,\mathrm{Hz} \leq f \leq 4000\,\mathrm{Hz}$ shaded in light gray. All curves in the figure show a similar behavior: a comparatively modest increase in $\hat{u}_{\max}$ until around $s = 10\,\mathrm{mm}$ is followed by steeper growth further downstream almost up to the trailing edge, where eventually saturation can be noticed.

In both simulation and experiment, the velocity fluctuations are composed of a hydrodynamic part and a contribution due to the sound particle velocity, which cannot be separated in a straightforward manner. The observed development can be explained by a low amplitude acoustic component originating at the trailing edge and slowly decaying in the upstream direction and a hydrodynamic instability growing exponentially in the downstream direction. The latter is stronger in amplitude only in the rear part, while in the upstream part the development is governed by the decay of the acoustic component. The growth rates in the downstream part are similar over the complete frequency band. Despite the similar growth rates, the dominant tonal mode S3 protrudes significantly over the background level. Interestingly, we find reasonable agreement between the computational and experimental tonal mode amplitudes in the rear part, whereas the amplitudes of the respective counterparts at similar frequencies are in the broadband range.

To conclude this analysis, the spatial growth in the separated region up to the trailing edge found in Fig. 3.11, together with the inflectional velocity profiles and low backflow levels found in Fig. 3.6 strongly indicate that the vortical structures visualized in Fig. 3.10 are the result of a convective Kelvin-Helmholtz type instability. Frequency selection remains an open question at this point, since the dominant mode S3 is amplified at a growth rate comparable to the ones found for a wide band of frequencies.

Fig. 3.12 visualizes the spatial structure of the dominant mode S3 and two representative DFT modes by means of isosurfaces of the streamwise velocity fluctuations in the left column and isocontours of pressure fluctuations in the $z = 110\,\mathrm{mm}$ cut in the right column. Note that plotting the real part results in an arbitrary but spatially consistent phase. The isosurfaces of mode S3 show a regular pattern on the side surface, similar to the coherent structures found in Fig. 3.10 in length scale and spanwise extent.

In contrast, the two modes representing the surrounding broadband range do

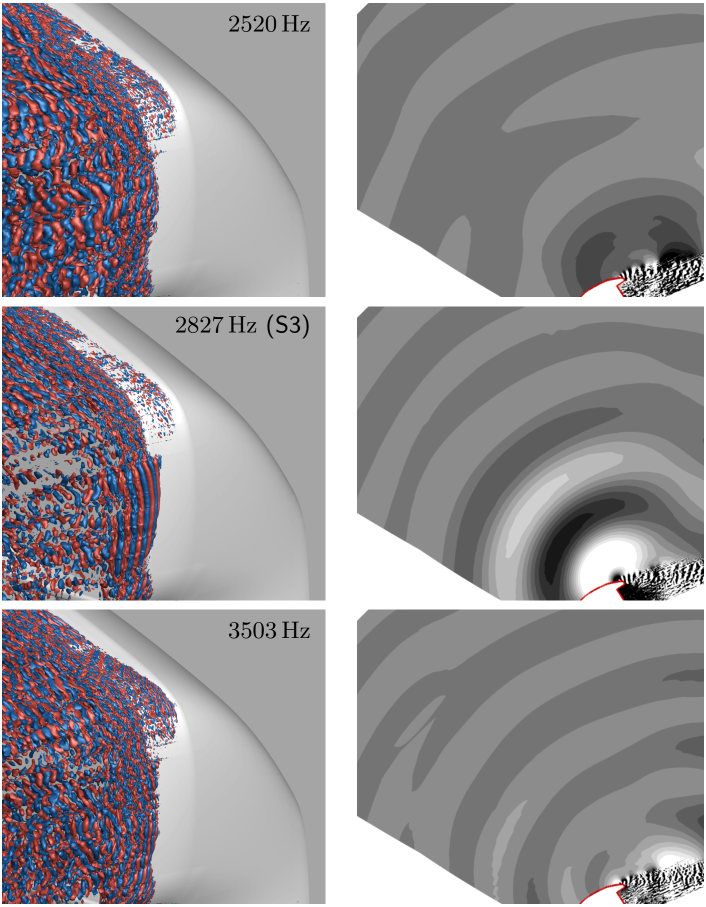

Figure 3.12: Left column: isosurfaces of (the real part of) positive and negative streamwise velocity for three DFT modes. The levels are chosen to ensure comparability. Right column: Pressure contours at $z = 110\,\mathrm{mm}$.

not exhibit this high level of regularity. The coherence of the vortex structures associated with S3 is also reflected in the visualization of the acoustic radiation in the right column of Fig. 3.12. Clearly, the acoustic source lies in the direct vicinity of the trailing edge on the side surface for the tonal mode S3, while more complex patterns emerge for the two other modes such that no clear statement regarding their source positions can be made.

## 3.5 Stability analysis

Our evaluation of the developed flow field provided several indications consistent with the notion of an underlying acoustic feedback instability driving the coherent vortex shedding and consequently the acoustic emissions from the side surface. The inflectional velocity profiles and the fluctuation growth along the shear layer Fig. 3.11 suggest that the vortex shedding at the trailing edge is preceded by a convective Kelvin-Helmholtz type instability. Stability considerations give detailed insight into these mechanisms. First, we analyze the amplification properties of the separated boundary layer by means of the local stability analysis described in Section 3.5.2. In the two subsequent Sections 2.5 and 3.5.4, the global stability of the flow is characterized using the techniques presented in Sections 2.6.2 and 2.6.3.

### 3.5.1 Base flow choice

For any hydrodynamic stability analysis, the first crucial step is the choice of an appropriate base flow. Since the underlying assumption of the linear theory is that the base flow satisfies the governing equations, the base flow should be a steady, laminar flow in the absence of any excitation, which we term equilibrium state. Such a flow can can be obtained by selective frequency damping [1] for arbitrary configurations. However, especially for flows with separated regions, the equilibrium state can differ significantly from the developed flow [56]. Consequently, the stability results may not be relevant to the considered flow. The obvious alternative is the time-averaged flow, which does not satisfy the governing equations (but the RANS equations). Barkley [7] compared stability results based on both the equilibrium state and the time-averaged flow for the case of cylinder flow. While the equilibrium state was found unstable – consistent with the presence of vortex shedding in the developed flow – the growth rates resulting from the time-averaged flow were marginally stable. However, using the time-averaged flow he was able to accurately predict the Strouhal frequency of the flow, whereas the most unstable frequencies of the equilibrium flow deviated from the vortex-shedding frequency of the developed flow. Broadly speaking, while the growth rates yielded by the time-averaged base flow analysis may be not representative, the frequencies of the dominant modes are expected to be captured more accurately. Since we are interested in the dynamics of the developed flow, we continue our analysis based on the time-averaged flow. This approach was also taken in previous tonal noise investigations at the NACA 0012 airfoil [24, 32, 56].

### 3.5.2 Local linear stability analysis

The stability of the boundary layer on the side surface is analyzed using the stability solver described in Section 2.6.1. The eigenvalue problem is approximated using 110 collocation points. The far field boundary condition is placed at $y(s) = 30\delta^*(s)$, where $\delta^*(s)$ denotes the local displacement thickness at position $s$. Only two-dimensional (streamwise) disturbances are considered, by setting the spanwise wavenumber $\beta = 0$. For each frequency $f = \omega/(2\pi)$, the spatial growth rate is retrieved as the negative imaginary part of the wavenumber, $-\alpha_i$. The net amplification for a particular frequency $f$ at position $s$ is then given by

$$n(f,s) = \ln\left(\frac{|U'(f,s)|}{|U'(f,s_0)|}\right) = -\int_{s_0(f)}^{s} \alpha_i(f,\tilde{s})d\tilde{s}, \tag{3.2}$$

where $s_0(f)$ marks the first occurrence of $-\alpha_i(f) = 0$ along the streamline. The resulting amplification along the $z = 110\,\mathrm{mm}$ cut on the side surface is plotted in the top row of Fig. 3.13 for frequencies up to 8830 Hz. The left panel illustrates that the onset of instability occurs at the same position over all considered frequencies, $s_0 \approx 21.5\,\mathrm{mm}$, in between the design edge and the point of separation. Furthermore, when considering the right panel, we find that a wide range of frequencies is amplified at all positions. Moreover, the variation with frequency is not very steep around the most amplified frequency. Thus, while the convective amplification process is undoubtedly a crucial component of the fundamental noise generation mechanism, it appears that its characteristics cannot explain the sharp frequency selection necessary for the generation of tonal noise.

The tonal noise frequency associated with the side surface ($f_{S3} = 2860\,\mathrm{Hz}$) is well within this amplified range, but significantly lower than the most unstable frequency predicted by the linear theory (4270 Hz). Analyses at $z = 120\,\mathrm{mm}$ and $y = -4\,\mathrm{mm}$ (cf. Fig. 3.6) also indicate that the most unstable frequencies are higher by up to 50% compared to the observed tonal frequencies. In the

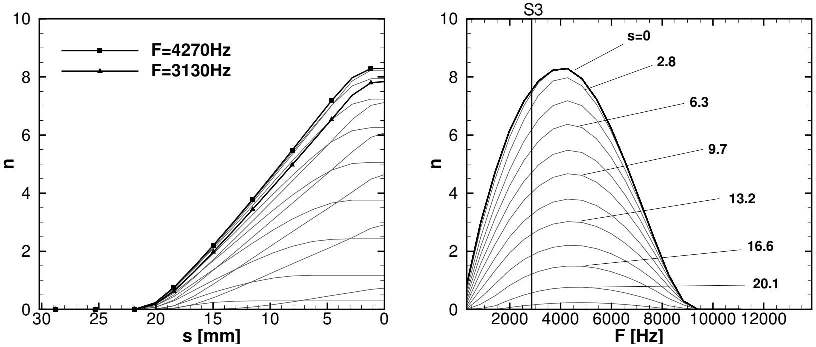

Figure 3.13: Integral amplification $n(f,s)$ at $z = 110\,\mathrm{mm}$ along the streamwise coordinate for selected frequencies ($277\,\mathrm{Hz} \leq f \leq 8830\,\mathrm{Hz}$, left) and at selected streamwise positions over frequency (right).

recent experimental investigation of Werner et al. [116] at the current mirror geometry, a similar discrepancy between tonal noise frequency and local LST predictions was noted.

However, in several previous studies [24,81,85] it was claimed that the main tonal noise frequency should correspond to the most amplified frequency according to LST. In both experimental (McAlpine et al. [81]) and numerical works (Desquesnes et al. [24]), reasonable agreement between the measured tonal noise frequency and the most amplified frequency was reported. On the other hand, in the DNS-based analysis of the NACA 0012 airfoil described by Jones and Sandberg [56], the dominant tonal frequency was found lower than the most unstable frequency. The authors argued that in the case of an acoustic feedback loop, the overall gain over a feedback cycle is determined not only by convective amplification, but also by the scattering at the trailing edge and the receptivity process. Both processes become more efficient towards lower frequencies, which consequently shifts the globally most amplified mode to a lower frequency. This reasoning was supported by analyses of the frequency dependency of the receptivity process around the leading edge [55] and of the scattering process at the trailing edge [56] for the case of the NACA 0012 airfoil.

### 3.5.3 Impulse response analysis

The local stability analysis in the preceding subsection identified the range of convectively amplified frequencies in the separated shear layer. However, the convective amplification process is only one of the relevant effects, among which are trailing edge scattering, upstream wave propagation and receptivity. In order to take into account all of these processes as well as their interactions, a global point of view is necessary. To that end, a global perturbation analysis as outlined in Section 2.6.2 is performed.

Since we are only interested in the near-wall dynamics, the perturbation simulation is conducted in a subdomain of the original simulation. Sponge terms are used to enforce homogeneous boundary conditions in terms of the disturbance variables at the artificial farfield boundaries. Furthermore, the perturbation simulation is run at $N = M = 7$, i.e. without de-aliasing, since only small amplitude disturbances are considered. This measure prevents possible perturbations caused by the round-off error in the application of the projection filter. The initial disturbance is placed in a wall-adjacent grid element at $z = 110\,\mathrm{mm}$ and $s \approx 21\,\mathrm{mm}$. It is realized as a spatially constant perturbation within the element with $U'(t = 0)/U_\infty = 10^{-8}$. Only the density and velocity components are perturbed.

The spatio-temporal response of the flow to the initial excitation is illustrated by a sequence of time instants in Fig. 3.14, where isosurfaces of the streamwise velocity disturbance $u'$ are shown alongside density disturbance contours on a $z = 110\,\mathrm{mm}$ and a $y = 0\,\mathrm{mm}$ slice. Non-dimensional time is defined as $\tilde{t} = t/T^*$. The first noticeable effect of the excitation is the emergence of a weak acoustic pulse ($\tilde{t} = 0.01$). Shortly later, we observe the formation and rapid growth of a hydrodynamic wavepacket ($\tilde{t} = 0.2$), which upon convection over the trailing edge is scattered to large scale acoustic emissions ($\tilde{t} = 0.49$). At $\tilde{t} = 0.7$, the most energetic part of the wavepacket has traveled past the trailing edge. The subsequently following wave structures still visible at the side surface are weaker in amplitude and result only in weak acoustic radiation. In the next snapshot, a second energetic wavepacket appears on the side surface, which again leads to significant acoustic radiation. The distinct structure of compact wavepackets is lost towards later times and superseded by a continuous pattern ($\tilde{t} = 1.5$).

Interestingly, temporally amplified instabilities are seen to form on the upper surface in Fig. 3.14, although the initial disturbance was placed on the side surface. The initial excitation of these instabilities is attributed to the initial acoustic pulse visible at $\tilde{t} = 0.01$. A wave pattern similar to the one found on the side surface is seen to develop. The location around which the instability appears

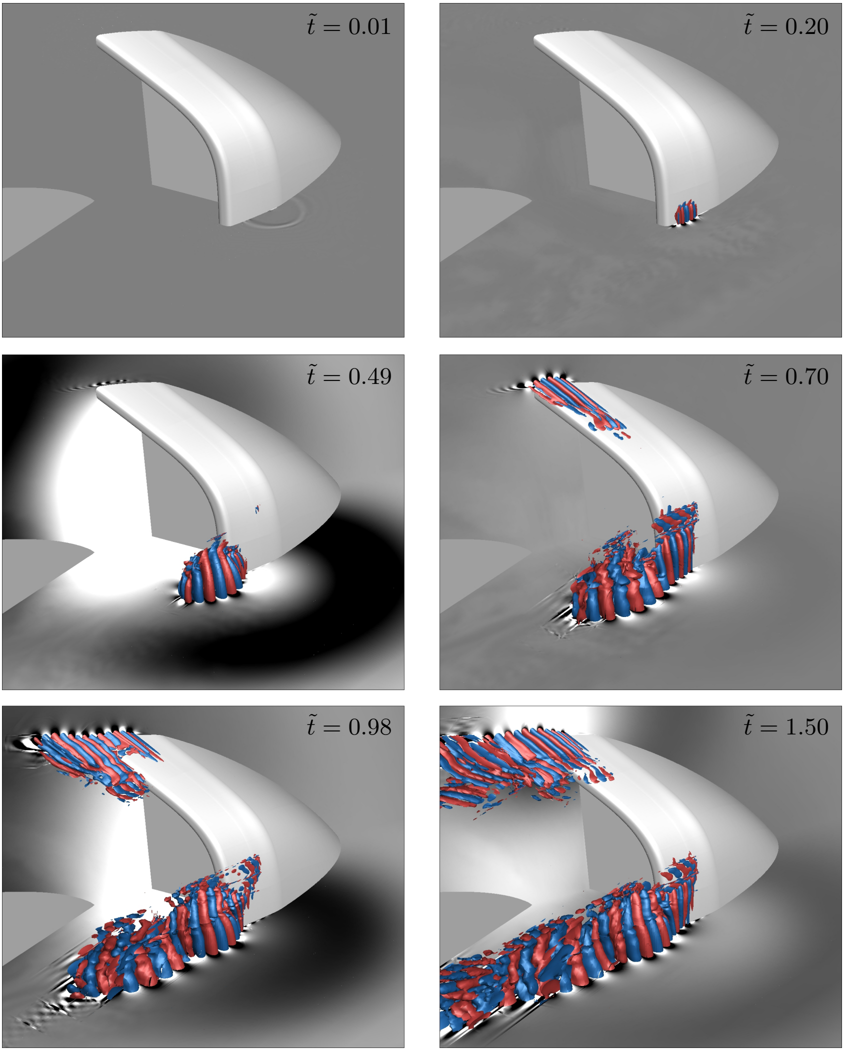
$\tilde{t} = 0.01$
$\tilde{t} = 0.20$
$\tilde{t} = 0.49$
$\tilde{t} = 0.70$
$\tilde{t} = 0.98$
$\tilde{t} = 1.50$

Figure 3.14: Time evolution of the disturbance wavepacket visualized by isosurfaces of the streamwise velocity disturbance $u'/u_\infty = \pm 10^{-7}$. Grayscale density contours with $-10^{-10} \leq \rho/\rho_\infty \leq 10^{-10}$ on slices at $z = 110\,\mathrm{mm}$ and $y = 0\,\mathrm{mm}$ characterize the acoustic radiation.

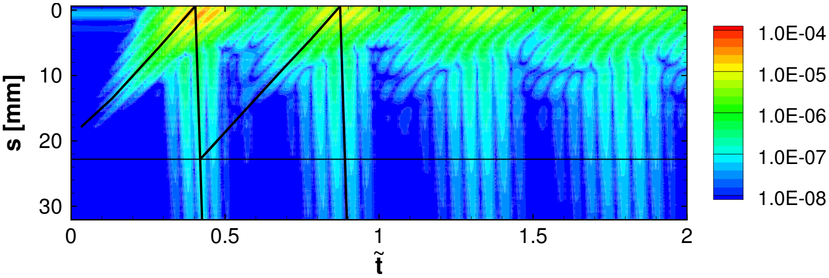

Figure 3.15: Time evolution of the pressure perturbation magnitude $|p'/p_\infty|$ along the wall-tangential line at $z = 110\,\mathrm{mm}$.

matches the tonal noise generation region on the side surface (cf. Fig. 3.9). The compact wavepacket structure can clearly be seen by plotting the perturbation pressure at the wall over time, which has been done in Fig. 3.15 along the $z = 110\,\mathrm{mm}$ line. In order to cover the large amplitude bandwidth including growing hydrodynamic components and relatively weak acoustic ones, we plot contours of $\log(|p'/p_\infty|)$, which also means that minima and maxima cannot be distinguished. In that plot, convection and growth of the first wavepacket are apparent between $\tilde{t} = 0$ and 0.5. From about $\tilde{t} = 0.3$, we observe the upstream running component of the acoustic emission generated at the trailing edge ($s \approx 0\,\mathrm{mm}$) by the initial wavepacket. Subsequently, a second hydrodynamic downstream running wavepacket is discernible at about $\tilde{t} = 0.6$. The sequence of these events indicates that the second hydrodynamic disturbance is initially excited through acoustic receptivity. In its early stage, the second hydrodynamic wavepacket has a very low amplitude and is thus obscured by the acoustic component. However, extrapolation of the trajectories helps estimate the approximate location of the effective receptivity position. We obtain $s_r \approx 23\,\mathrm{mm}$, about $2\,\mathrm{mm}$ downstream of the DE. This position is located within the region of rapid mean flow adjustment (Fig. 3.6) downstream of the pressure minimum, where the boundary layer is expected to be most susceptible to external disturbances [102]. Furthermore, the local stability analysis in Section 3.5.2 showed that shortly downstream of that position the flow first becomes unstable. Modes excited further upstream initially undergo damping, while downstream excited modes possess a shorter amplification length. Thus, we expect the dominant modes to be induced in a narrow region in the direct vicinity

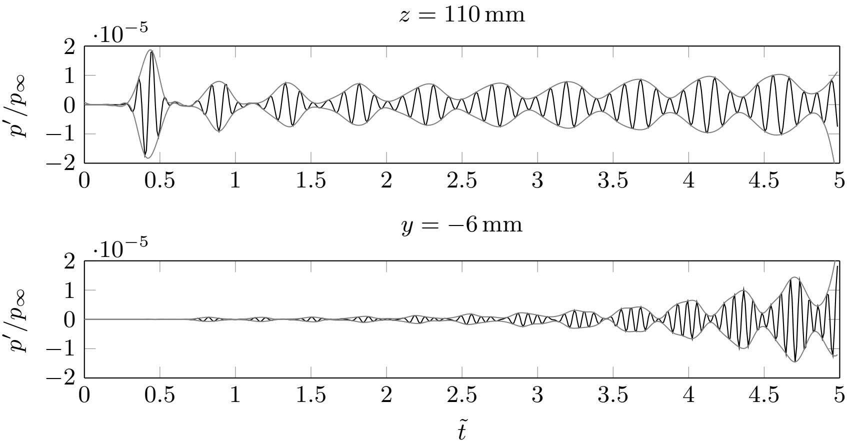

Figure 3.16: Perturbation wall pressure $p'/p_\infty$ at the trailing edge at $z = 110\,\mathrm{mm}$ (top) and $y = -6\,\mathrm{mm}$ (bottom) as a function of time.

of the DE. The process of alternating hydrodynamic and acoustic wavepackets is maintained towards later times. Hence, the impulse response analysis uncovers the self-sustained acoustic feedback loop instability at the side surface of the mirror.

Temporal growth or decay is addressed by plotting the wall pressure signal at the trailing edge in Fig. 3.16 for the side surface (top) and a position within the excited region at the upper surface (bottom) found in Fig. 3.14. The resulting signal in Fig. 3.16 (top) is characterized by a drop in amplitude after the first wavepacket, followed by slow temporal growth. The solution can be thought of as a superposition of a continuous range of growing or decaying global modes triggered by the initial disturbance. The higher amplitude of the first wavepacket is a result of the decay of most of these modes, while for later times an asymptotic state dominated by the growing global modes is reached. As opposed to the flow on the side surface, which is directly affected by the initial disturbance, at $y = -6\,\mathrm{mm}$ we observe strictly monotonic growth at a higher rate. Furthermore, the instability frequency at this location is higher. Again a clear wavepacket structure is visible, strongly suggesting the dynamics on the upper surface are also governed by an acoustic feedback loop.

By considering the envelope of these signals, it is possible to measure the time it takes to complete one cycle of the loop. Measuring from peak to peak yields $T_{\mathrm{loop}}/T^* \approx 0.47$ or $f_{\mathrm{loop}} \approx 591\,\mathrm{Hz}$ at $z = 110\,\mathrm{mm}$ and $T_{\mathrm{loop}}/T^* \approx 0.35$ and $f_{\mathrm{loop}} \approx 793\,\mathrm{Hz}$ at $y = -6\,\mathrm{mm}$.

### 3.5.4 Modal decomposition

Through the impulse response analysis in the preceding subsection, the presence of self-sustained acoustic feedback loop instabilities could be evidenced. These instabilities emerge in the same regions that have been identified as tonal noise source regions (cf. Fig. 3.9). Using the DMD algorithm outlined in Section 2.6.3, we now approximate the contributing global modes and their associated frequencies and growth rates. Note that although the DMD approximates the eigenmodes of the operator similar to Krylov methods [106], its results are always dependent on the underlying time series.

The solution vector of primitive perturbation variables $(\rho', u', v', w', p')^T$ is sampled using the element-local representation with $(N+1)^3$ Gauss points at 201 snapshots in time with timestep $\Delta\tilde{t} = 0.02$, corresponding to a sampling frequency of 13.9 kHz. The resulting time interval ranges from $\tilde{t} = 0$ to 4.

Fig. 3.17 shows the Ritz spectrum obtained via DMD, wherein the imaginary and real parts of the Ritz values represent the angular frequency and the growth rate, respectively. Thus, modes with $\omega_r > 0$ are unstable. The color and size coding is based on the Euclidean norm $||\hat{\mathbf{k}}_j||$ of the associated modes, which can be seen as a measure of their initial energy.

Most of the spectrum's energy is contained in a continuous, mostly damped branch ranging from 0 to about $6000\,\mathrm{s}^{-1}$. However, two sets of regularly spaced, discrete modes clearly protrude over this background branch. Visualization of the associated modes helps identify the spatial region where the respective modes are mostly active. Exemplary modes are visualized by means of streamwise velocity disturbance isocontours in Fig. 3.18. It turns out that the discrete mode set with lower frequencies (S1-S3) dominates the dynamics at the side surface, while the higher frequency discrete modes are associated with the critical region on the upper side (U1-U3). Thus, DMD identifies the dominant global modes resulting from the acoustic feedback loop.

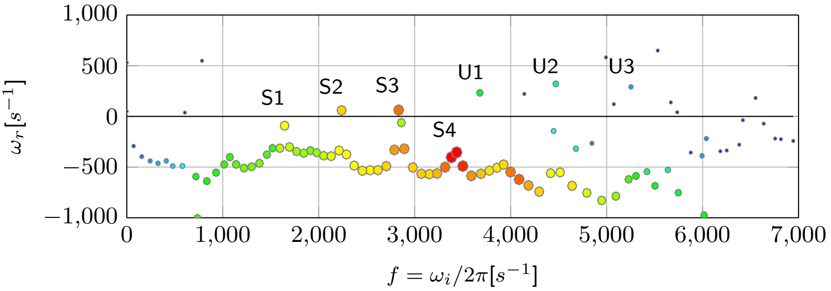

Figure 3.17: Ritz spectrum of the DMD based on the perturbation calculation in the complex stability plane. $\omega_r > 0$ defines the unstable halfplane, coloring and size indicate the Euclidean norm $||\hat{\mathbf{k}}_j||$ of the respective mode. The symmetric complex conjugate part is omitted.

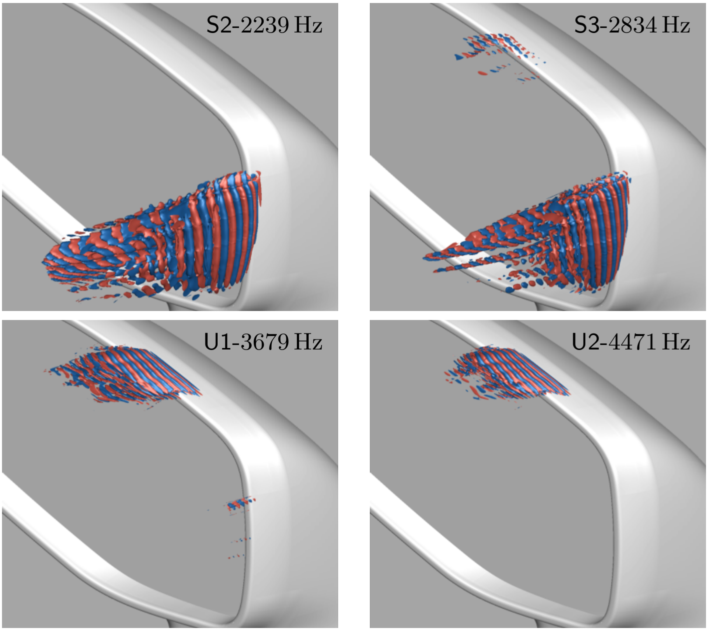

Figure 3.18: Isosurfaces of positive (red) and negative (blue) streamwise velocity $\hat{u}_i/u_\infty$ of selected unstable dynamic modes.

The frequencies of the approximate global feedback instability modes yielded by the perturbation analysis ($f_p$) can be compared to the ones of the tones observed in the developed flow ($f_{\mathrm{LES}}$) in Table 3.2. A good match can be noted for all tones detected in Fig. 3.8 and Fig. 3.9. The slight discrepancies may be explained by the limited frequency resolution, possible base flow modifications on a slow timescale and the nonlinear effects present in the LES. Overall, the remarkable coincidence of the dominant global mode frequencies and the tonal modes underpins the relevance of the global stability analysis to the developed flow and directly connects the tonal noise generation to the acoustic feedback instability. Interestingly, not all of the feedback modes determined by the stability analysis are observable in the developed flow.

In Section 3.4.2, it was found that only one of the tonal modes generated at the side surface in the experiment could be captured in the simulation. The global stability analysis retrieves a trace of the missing mode S4 in Fig. 3.17. However, judging from its comparatively high decay rate, it is not surprising that this tone was not detectable in the developed flow. While the exact reason for this discrepancy with the experiment is unknown, the differences between simulation and experiment in terms of environmental disturbances and sound propagation are deemed as more likely causes than insufficient spatial resolution. According to the estimated range of resolved frequencies in Table 3.1, S4 should be appropriately resolved by the computational mesh. Furthermore, the computation captures tones of significantly higher frequency at the upper surface.

| Mode | | S1 | S2 | S3 | U1 | U2 | U3 |
|---|---|---|---|---|---|---|---|
| $f_p$ | [Hz] | 1645 | 2239 | 2834 | 3679 | 4471 | 5254 |
| $f_{\mathrm{LES}}$ | [Hz] | – | – | 2860 | 3545 | 4382 | – |
| $\Delta f_k$ | [Hz] | – | 594 | 595 | – | 791 | 783 |
| $1/T_{\mathrm{loop}}$ | [$\mathrm{s}^{-1}$] | | 591 | | | 793 | |

Table 3.2: Frequencies of unstable feedback modes from the perturbation calculation $f_p$, their respective frequencies from the power spectra of the LES data $f_{\mathrm{LES}}$ (if detectable), frequency spacing $\Delta f = f_k - f_{k-1}$ and 'loop frequency' $1/T_{\mathrm{loop}}$ for side surface (S) and upper surface (U) measured from Fig. 3.14.

### 3.5.5 Relation to the phase condition

Some of the previous experimental and theoretical works [3,21,61,93] on laminar whistling sounds (cf. Section 1.1) introduced the notion of a phase condition to explain and predict the selection of discrete frequencies by the acoustic feedback mechanism. Basically, this criterion states that a feedback instability can only be self-maintaining if the net phase difference over one cycle of the loop vanishes. In the following, we show that such a condition is also fulfilled by the feedback modes identified in Section 3.5.4.

Using the notation of Plogmann et al. [93], the phase shift over one cycle is written as

$$\Delta\varphi(f) \approx 2\pi f \left( \frac{d}{u_{\mathrm{ph}}(f)} + \frac{d}{c - \overline{u}_\delta} \right) + \varphi_d, \tag{3.3}$$

where $d$, $u_{\mathrm{ph}}(f)$, $\overline{u}_\delta$ and $c$ denote the distance between the effective receptivity position and the trailing edge, the average phase velocity of the instability, the average velocity at the edge of the boundary layer of the base flow and the speed of sound. The phase delays introduced by the trailing edge scattering and the receptivity process are combined into an effective phase delay $\varphi_d$. The overall phase shift defined in (3.3) must be balanced by an integer multiple of $2\pi$, i.e. $\Delta\varphi(f_k) = 2\pi k$.

Taking the difference between (3.3) for $k$ and its counterpart with $k-1$ and rearranging yields

$$f_k - f_{k-1} = \Delta f_k \approx \left( \frac{d}{u_{\mathrm{ph}}} + \frac{d}{c - \overline{u}_\delta} \right)^{-1}, \tag{3.4}$$

where it is assumed that $u_{\mathrm{ph}}(f)$ only varies weakly between $f_k$ and $f_{k-1}$. Note that the term within brackets corresponds to the loop time $T_{\mathrm{loop}}$, which has been estimated from the signal plotted in Fig. 3.16.

Eq. (3.4) shows that the frequency spacing between adjacent modes $\Delta f$ is determined by the reciprocal of the loop time. Furthermore, it is basically independent of the phase delay $\varphi_d$. The frequency spacing between the feedback modes can be compared to $1/T_{\mathrm{loop}}$ in Table 3.2. The remarkable agreement for both tonal source regions S and U evidence that frequency selection is directly tied to the loop time. In addition, it suggests that the tones are organized in agreement with the theoretical phase condition. Modes fulfilling this criterion are able to reinforce themselves over each cycle, while modes between these discrete positions in frequency space are damped.

## 3.6 Summary and discussion

To conclude, the main insights resulting from the simulation at the side mirror are as follows.

- The high order DGSEM simulation of the compressible Navier-Stokes equations is capable of predicting tones associated with an acoustic feedback loop around the laminar separated shear layer upstream of the mirror's trailing edge.
- The good agreement with the measurements in base flow quantities such as the pressure distribution and the boundary layer profiles at the tonal source regions in principle enables quantitative comparability of the tone frequencies. Even so, agreement is only found for one tone frequency. Experimental evidence suggests a high influence of environmental conditions and external disturbances on the selection of the tone frequencies [85]. Thus, quantitative comparisons are difficult even between careful measurements and a highly accurate simulation. Apart from this fundamental issue, we highlight the identification of the tonal noise source locations in close accordance with the experiment.
- Tonal noise generation via coherent vortex shedding is observed for the case of open separation at the side surface as well as for turbulent reattachment upstream of the trailing edge at the upper side. The latter case illustrates that even if the boundary layer reattaches, the spanwise coherence loss ultimately eliminating the tone requires a finite distance to develop.
- The global stability analysis provides evidence for the existence of an acoustic feedback loop governing the dynamics in the tonal source regions and selecting the precise discrete frequencies found in the developed flow. Furthermore, the estimated effective receptivity position from the analysis is consistent with the notion of localized receptivity via strong mean flow gradients induced by the surface curvature at the design edge. It is shown that the frequencies of the feedback modes obtained in the global analysis are spaced consistent with the phase condition.

The obtained results also serve as validation case for the chosen computational approach. However, due to the high effort in terms of mesh generation and computational resources, a deeper computational analysis is realized based on a simplified model geometry in Chapter 4.

# 4 Analysis of a simplified mirror model

The computational investigation presented in Chapter 3 successfully confirmed the acoustic feedback mechanism known from airfoil self-noise as the driving mechanism behind the tonal noise generation for the present mirror geometry. In order to fundamentally study the noise generation process, it is necessary to reduce the complexity of the considered flow problem. Based on the findings of Chapter 3, a simplified, two-dimensional mirror model is devised to isolate the fundamental tonal noise generation mechanism. The simplified design reduces the computational cost by orders of magnitude compared to the original mirror and thus allows for parameter variations, facilitates analysis and enables us to explore the effects of simple geometrical modifications.

In the present chapter, after the definition of the simplified mirror model, we introduce the simulation strategy chosen to most efficiently exploit the two-dimensional geometry in terms of computational resources. The obtained flow features and noise emissions are then first presented and compared to the corresponding wind tunnel measurements in order to establish the suitability of the geometry and the simulation approach to investigate the tonal noise generation at the original mirror. Subsequently, we evaluate the radiated noise over a wide range of free-stream velocities. It is then possible to compare the computational trends with the experimentally observed ladder structure, which remains the most important evidence of the feedback loop in experimental analyses. The above analyses are also available in [34]. Finally, geometric countermeasures to suppress or at least diminish the tones are evaluated, which arise as direct consequences from our analysis and obey the objectives and boundary conditions in automotive aeroacoustic development.

## 4.1 Definition of the mirror model

One of the two dominant tonal noise contributers at the three-dimensional geometry was identified as the side surface marked with (S) in Fig. 4.1 (left). Starting from a horizontal cut through this surface at $z = 110\,\mathrm{mm}$, the two-dimensional mirror model was optimized by Werner et al. [117] using the mixed-design routine of XFOIL so as to mimic the pressure distribution measured on

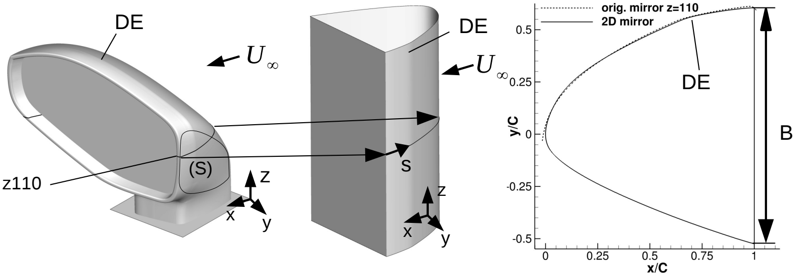

Figure 4.1: Left: Original mirror geometry with the cut at $z = 110\,\mathrm{mm}$, center: Extruded mirror model, right: Cross-sectional view through the mirror model.

the original mirror. The lower surface of the mirror model was chosen to give a favorable pressure gradient up to the trailing edge in order to minimize the acoustic radiation from that position.

Fig. 4.1 (left) shows the cut in the original geometry, the extruded mirror model (center) and a corresponding cross-section (right). This cross-section reveals that the optimized, final version of the mirror model only slightly differs from the original cut. In Chapter 3, the so-called design edge (DE) was identified as the crucial geometric element for the tonal noise generation mechanism, as (i) the boundary layer separates shortly downstream (Fig. 3.6) and (ii) the rapid streamwise development of the boundary layer profiles promotes natural receptivity (Fig. 3.15). In the cross-section of the mirror model in Fig. 4.1 (right), the DE appears as a relatively subtle hump. The local change in curvature may be noticed more clearly in the shaded representation of the mirror model in Fig. 4.1 (center). The length and relative base height of the model are $C = 70.17\,\mathrm{mm}$ and $B/C = 1.13$.

Preliminary simulations and experiments showed that the flow around the simplified mirror geometry develops large scale bluff-body type vortex shedding at low frequencies on the order of 100 Hz for $u_\infty = 27.78\,\mathrm{m\,s^{-1}}$. This large scale unsteady motion dominates the local flow at the trailing edge to the degree that no high frequency tone appears. As a remedy, a splitter plate was attached at the base of the simplified mirror in both simulation and experiment so as to create a calmer wake flow. In two-dimensional simulations and in the experiments, a splitter plate of length $L_{\mathrm{SP}}/C = 5.7$ or 400 mm was found long enough to ensure that the separated shear layer at the edge of the wake reattaches on the splitter plate before it reaches the trailing edge. In the three-dimensional simulation, it was necessary to increase the splitter plate length to $L_{\mathrm{SP}}/C = 8$.

## 4.2 Simulation setup

### 4.2.1 Strategy

Two main aspects arise in the simulation of the mirror model, which lead to the specific simulation strategy that was chosen for the current investigation:

- First, we wish to analyze a local flow feature with small length and time scales lower than $C$ and $C/u_\infty$, namely the tonal noise generation mechanism in the vicinity of the trailing edge. However, in order to ensure realistic flow conditions for this mechanism, the turbulent wake flow must be taken into account. The associated largest length and time scales must be expected to be on the order of $L_{\mathrm{SP}}$ and $L_{\mathrm{SP}}/u_\infty$, respectively. Consequently, we face a strong disparity in length and time scales between the large scale wake flow and the target noise generation mechanism, leading to both a large number of degrees of freedom and a high number of time steps to reach statistical convergence. Furthermore, in simulations of two-dimensional setups like the one at hand, the spanwise extent of the computational domain should be chosen so as to prevent artificial correlation in the spanwise direction. For simulations of laminar separation bubbles, the spanwise extent $L_z$ is typically chosen based on a length scale of the bubble, such as the peak displacement thickness. For instance, Jones et al. [54] used $L_z = 10\delta^*_{\mathrm{max}}$ in a DNS of laminar separation at a flat plate. Due to the bluff-body wake, in our case the spanwise extent of the computational domain must be chosen considerably larger, which significantly increases the computational cost.

- Second, since the mechanism to be investigated is fundamentally two-dimensional, two-dimensional simulations are desirable. They should be used when possible, i.e. when the influence of three-dimensional effects such as turbulence on the examined flow features can be neglected.

Based on these considerations, a two-step simulation approach is followed. In a first step, an LES of the complete configuration including the splitter plate is

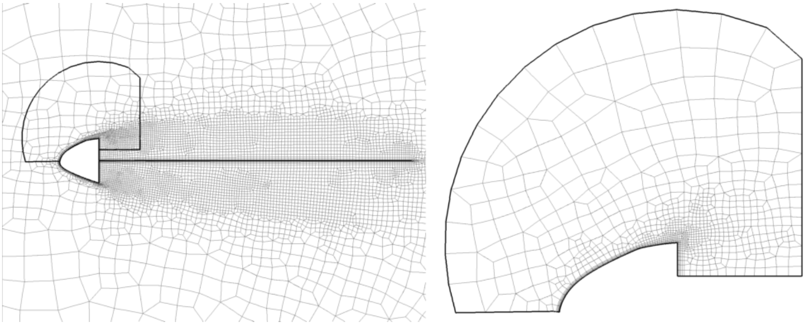

Figure 4.2: Left: computational mesh of the base flow simulation including the boundaries of the subdomain. Right: computational mesh of the subdomain simulation.

conducted using a comparatively coarse grid. This simulation aims at capturing the mean turbulent wake flow. In the second step, subdomain simulations are performed, which enclose only the local flow around the mirror model. In these simulations, the mean flow conditions are controlled by imposing the time-averaged flow field from the first LES as a farfield boundary condition. This approach largely reduces the required computational effort, as only one simulation resolving the large-scale turbulent wake is required, while the investigation of the mechanism itself can be performed on the subdomain, allowing for a high resolution of the trailing edge region. In addition, subdomain simulations can be carried out in two or three space dimensions to examine the effects of resolved turbulence on the noise generation while always maintaining the surrounding original mean flow through the boundary conditions.

### 4.2.2 Computational meshes and parameters

We denote the base flow simulation containing the complete setup by BF, while the two and three-dimensional subdomain configurations are termed SUB2D and SUB3D. Fig. 4.2 (left) shows the employed computational grid for BF as well as the boundary of the subdomain, while Fig. 4.2 (right) shows the one for SUB2D and SUB3D. Note in particular that only the upper surface of the mirror model is included in the subdomain. For case BF, the farfield boundary is circular with $R = 100C$. The mirror surface is described using a polynomial mapping with $N_{\text{geo}} = 4$. Like both sides of the (infinitely thin) splitter plate, it is implemented as no-slip isothermal wall using the free-stream temperature. For the three-dimensional simulations, periodic boundary conditions are applied in the spanwise direction. Furthermore, we rely on the free-stream material properties listed in Section 3.2 for all simulations.

Details on the polynomial approximation, the de-aliasing procedure, the grid resolution and computational time can be found in Table 4.1, where we rely on the definitions introduced in Section 3.3. For the three-dimensional simulations, the table also provides the spanwise extent of the domain based on the model 'chord' $L_z/C$ and based on the peak displacement thickness $L_z/\delta^*$. Resolution measures $f_{4\text{ppw}}$ and $N_p(\delta_{99})$ as defined in Section 3.3 are included, which are given based on the baseline free-stream velocity $u_\infty = 27.78\,\mathrm{m\,s^{-1}}$. A significantly higher resolution through the higher polynomial degree is employed for the subdomain cases in order to accurately capture the processes in the near-wall region, while the main purpose of simulation BF is the generation of a suitable mean flow.

For case BF, a Smagorinsky subgrid scale model with $C_s = 0.03$ is applied locally in the wake region behind the mirror model. Implementation details for this model can be found in [13]. All other simulations can be termed no-model LES as they rely on the de-aliasing procedure only. In the subdomain cases, a sponge zone (see Section 2.5.9) is applied at the artificial boundaries to attenuate outgoing disturbances. The associated damping coefficient is set to $d = 10u_\infty/C$, while the mean flow from case BF serves as sponge base flow $U_B$. For the simulations presented in the current chapter, the alternative 14 stage Runge-Kutta scheme (Section 2.5.7) was preferred for time integration, due to its slightly larger time step per stage. Initial tests at the mirror model revealed only negligible differences compared to the classical five stage low storage Runge-Kutta scheme.

Table 4.1 also provides computational performance information of the simulations performed on the CRAY XC40 Hornet and Hazel Hen clusters. CPU and wall times are given in terms of convective time units $T^* = C/u_\infty$ for $u_\infty = 27.78\,\mathrm{m\,s^{-1}}$. We define the performance index (PID) as the CPU time required for the evaluation of one Runge-Kutta stage for one integration point. From the PID, we recognize that the two-dimensional operator is about 60% faster. The load per core is within the nominally optimal range (cf. Section 2.5.10), which is reflected in the similar PID of the three-dimensional cases. Nonetheless, large differences between these cases can be noticed in CPU and wall time. The reason for the performance advantage of the BF configuration lies in the fact that it's timestep is larger by almost an order of magnitude, which is enabled by the coarser near-wall resolution and the lower polynomial degree.

Table 4.1: Computational setup, resolution and performance details for the base flow (BF) and subdomain (SUB2D and SUB3D) configurations. The grid spacings are taken at the DE approximately at $x = 0.7C$ in Fig. 4.1 (right) and are given as $\Delta x = \Delta x_{\text{Elem}}/(N+1)$ in order to take into account the element-local resolution. $L_z$ and $n_{\text{Elems},z}$ denote the spanwise extent of the domain and the the number of elements in the spanwise direction, respectively.

| Case | BF | SUB2D | SUB3D |
|---|---|---|---|
| dim. | 3D | 2D | 3D |
| $N$ | 3 | 7 | 7 |
| $M$ | 4 | 9 | 9 |
| $L_z/C$ | 0.6 | – | 0.2 |
| $L_z/\delta^*$ | 40 | – | 14 |
| $n_{\text{Elems},z}$ | 16 | – | 8 |
| $n_{\text{Elems}}$ | 122,000 | 1,087 | 8,969 |
| $n_{\text{GP}} \times 10^{-6}$ | 26.0 | 0.1 | 15.0 |
| $\Delta y$ [mm] | 0.070 | 0.014 | 0.014 |
| $\Delta x$ [mm] | 0.55 | 0.21 | 0.21 |
| $N_p(\delta_{99})$ | 8 | 28 | 28 |
| $f_{4\text{ppw}}$ [Hz] | 6,360 | 13,230 | 13,230 |
| $\Delta t \times 10^8$ [s] | 48.5 | 6.0 | 5.75 |
| No. cores | 8736 | 96 | 4368 |
| Load ($n_{\text{GP}}$ / no. cores) | 3017 | 1132 | 3440 |
| PID $\times 10^{-6}$ [s] | 1.24 | 0.48 | 1.30 |
| CPU time / $T^*$ [h] | 798 | 8.45 | 3303 |
| Wall time / $T^*$ [min] | 5.5 | 5.3 | 45.4 |

## 4.3 Base flow simulation

Although the main purpose of run BF is the generation of a suitable mean flow, we briefly analyze the resulting flow and radiated sound and compare the results with the available measurements at the mirror model with splitter plate performed in the LWT, which are documented in [117].

### 4.3.1 Flow field

The flow field is initialized with the free-stream velocity $u_\infty = 27.78\,\mathrm{m\,s^{-1}}$, which yields $Re_C \approx 130,000$ or $Re_L \approx 10^6$. It is then advanced in time for 10 convective time units $T^* = C/u_\infty$ before statistics are collected. Fig. 4.3 shows contours of velocity magnitude averaged over $190T^*$ and exemplary streamlines, characterizing the 'dead-air' region behind the mirror model. On the upper surface of the splitter plate, the mean reattachment point is located at $x/C = 7.4$. Mean reattachment on the lower surface seems to take place in close proximity to the trailing edge of the splitter plate at $x/C = 9$, so that traces of the large scale unsteadiness might still be present. However, the flow was found sufficiently steady to obtain statistically converged mean flow fields and to support tonal noise generation at the trailing edge of the mirror model, which will be shown in the following.

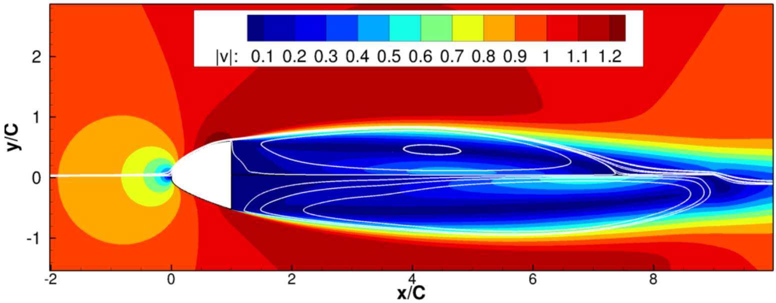

Figure 4.3: Isocontours of the time-averaged velocity magnitude $\langle|\vec{v}|/u_\infty\rangle$ and exemplary streamlines for case BF.

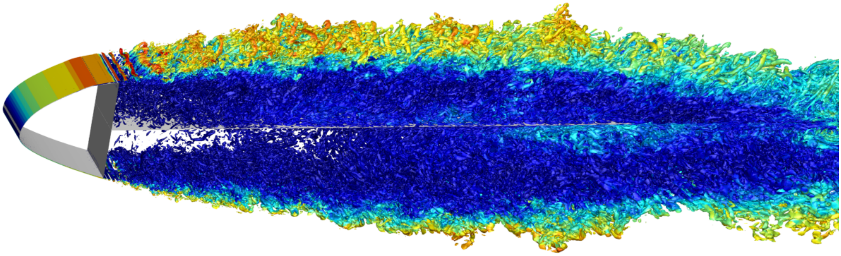

Figure 4.4: Isosurfaces of the $Q$ criterion for $Q = 5(u_\infty/C)^2$ colored with velocity magnitude $|\vec{v}|$ for a random instant of simulation BF.

An impression of the three-dimensional, instantaneous flow is given in Fig. 4.4, which shows isosurfaces of the $Q$ criterion at a random instant. Along the mirror model surface, the flow is laminar up to the trailing edge, where we observe shedding of spanwise oriented vortical structures, which appear due to laminar separation upstream of the trailing edge. Downstream, they first exhibit spanwise modulation and soon develop into turbulent structures. Owing to the splitter plate, large-scale vortex shedding with length scales on the order of the model's vertical extent cannot be recognized in the direct vicinity of the mirror model.

The resulting mean pressure distribution on the mirror model is plotted in Fig. 4.5 (left) and can be compared to both measurements at the mirror model and the corresponding distribution for the simulation of the original mirror discussed in Chapter 3 at the $z = 110\,\mathrm{mm}$ cut. The latter distribution was shifted and scaled in the $x$ coordinate to match the positions of the trailing edge and the DE. We first notice that the three distributions appear similar and are characterized by acceleration of the flow along the surface up to a suction peak close to the point of peak curvature ($x_{\mathrm{DE}}/C \approx 0.67$). Downstream, a relatively flat pressure distribution appears as a consequence of boundary layer separation. The separation point for case BF is located at $x_S/C \approx 0.73$. Thus, the qualitative features of the mean flow in the tonal source region of the original

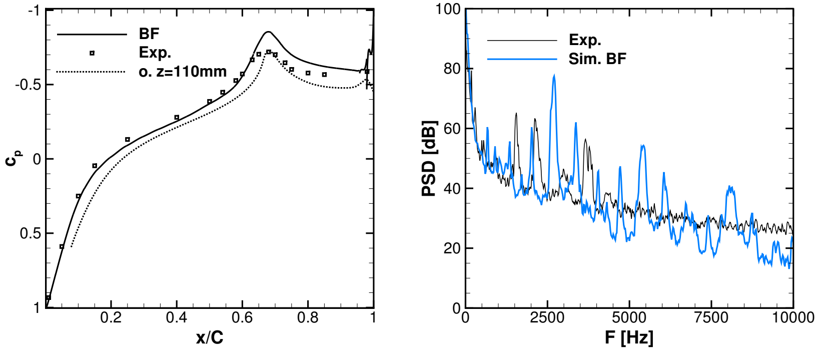

Figure 4.5: Left: Pressure coefficient on the upper surface of the mirror model for simulation BF and corresponding measurements. For comparison, the pressure coefficient is also given for the original mirror at $z = 110\,\text{mm}$. Right: PSD spectrum of pressure at $\vec{x} = (3.22C, 3.6C)^T$ for simulation BF and the corresponding inflow microphone measurement. Reference value $p_{\text{ref}} = 4 \cdot 10^{-10}\text{Pa}^2/\text{Hz}$.

mirror are accurately reproduced by the model geometry in both simulation and experiment. Furthermore, despite the slightly stronger, more distinct suction peak present in the computational result, we find overall reasonable agreement between simulation and experiment.

### 4.3.2 Acoustic emissions

Fig. 4.5 (right) shows a comparison of the radiated sound by means of PSD spectra between the directly computed noise in simulation BF and inflow microphone measurements. The probe is located approximately $2.2C$ behind and $3C$ above the trailing edge of the mirror model. The computational spectrum is obtained from a time signal of length $390T^*$ or 0.98 seconds using a sampling rate of 44.1 kHz, 2048 samples per block, 50% overlap and Hanning windowing, while the experimental signal length amounts to 5 minutes and is processed using the same sampling rate and 4096 samples per block with Hanning window but without overlap.

Both spectra are composed of multiple narrowband peaks protruding beyond the slowly decaying broadband spectrum by up to 40 dB (for the simulation). In the computational case, the broadband component can hardly be distinguished from the dominant tonal peaks, but it seems to match the experimental broadband level quite well towards the low frequency end. From about $F \geq 3000\,\mathrm{Hz}$, the computational spectrum decays faster towards higher frequencies than the measured one. A similar behavior was also found in the side mirror case (cf. Section 3.4.2) and might be related to wind tunnel background noise (boundary layers, screens and fan noise) and free-stream disturbances altering the transitional flow around the mirror model. The computational peaks are of higher amplitude, which can be attributed to the uninterrupted spanwise coherence of the vortical structures at the trailing edge (see Fig. 4.4). This coherence might be a consequence of either or both the missing freestream turbulence or a still too low spanwise extent of the computational domain. However, this effect was expected and could not be circumvented in the design of the simulation.

More importantly, the peak frequencies of the simulation do not match the measured ones. The first reason for this mismatch could be the slight deviation in the mean flow between simulation and measurement (see Fig. 4.5 (left)). Indeed, a necessary requirement for quantitative agreement in the selected frequencies by a feedback loop is the precise same development of the boundary layer, which dictates the receptivity and stability properties. Reflections of the emitted sound at the wind tunnel walls also might interfere with the frequency selection through the feedback loop. A strong influence of the environmental conditions in closed test section facilities on the peaks has been noted by Nash et al. [85] for the case of the NACA 0012 airfoil. Finally, the comparatively low spatial resolution in run BF could affect the peak frequencies via modified instability characteristics of the separated shear layer.

Despite these issues, the simulation displays base flow characteristics that mimic the conditions at the original mirror. It also exhibits significant tonal noise emissions in the same frequency range as the measurement. Given the strong similarities to the original side mirror case in terms of mean flow and the coherent vortical structures in Fig. 4.4, these tones are most likely caused by the same feedback mechanism as found in Chapter 3. Thus, the associated time averaged flow field is employed as base flow for further analysis of the tonal noise generation mechanism by means of the mirror model.

## 4.4 Subdomain simulation

In this section the simulation results of the subdomain runs (SUB2D and SUB3D in Table 4.1) are discussed for the baseline velocity $u_\infty = 27.78\,\mathrm{m\,s^{-1}}$ in order to validate the subdomain approach. Furthermore, by comparing SUB2D and SUB3D, the suitability of two-dimensional simulations for our analysis is evaluated. In contrast to case BF, a variation of the polynomial degree in the current setup demonstrated that the hydrodynamic and acoustic results can be regarded as practically grid-converged.

### 4.4.1 Mean flow

The subdomain runs are initialized with the mean flow from case BF and advanced for $20T^*$ and $10T^*$ for the SUB2D and SUB3D, before time-averaging is performed over $180T^*$ and $50T^*$, respectively. The long interval for SUB2D is necessary to assure statistically converged PSD spectra, however the mean flow properties converge much faster. The collapse of the resulting mean pressure distributions shown in Fig. 4.6 (left) confirms that the mean flow from BF is successfully enforced through the farfield boundary conditions in the subdomain. In addition, the mean pressure distribution is not altered notably in the two-dimensional simulation SUB2D compared to BF and SUB3D.

The separated laminar boundary layer drives the vortex shedding at the trailing edge and ultimately governs the associated sound generation. In order to characterize its development, Fig. 4.6 (right) shows the Reynolds number based on the displacement thickness $Re_{\delta^*} = \rho_e u_e \delta^* / \mu$, where $(\cdot)_e$ denotes evaluation at the edge of the boundary layer. Up to $x/C \approx 0.7$, $Re_{\delta^*} \approx 400$ and varies only weakly due to the strongly accelerating flow around the mirror model for all three cases. In this region, it remains below the instability threshold for a Blasius boundary layer of $Re_{\delta^*} = 520$, illustrating the high stability of the boundary layer upstream of the DE. Shortly downstream of $x_{\mathrm{DE}}/C \approx 0.67$, $Re_{\delta^*}$ begins to grow considerably and approximately linearly up to the trailing edge. This growth appears slightly earlier and is stronger for case SUB3D. However, the overall deviation between the three cases is low. Finally, the shape factor $H = \delta^*/\theta$ is plotted in the same diagram, where $\theta$ denotes the momentum thickness. We find the same division into a nearly constant part upstream of $x_{\mathrm{DE}}$ followed by rapid growth towards the trailing edge, which does not differ significantly between the different runs. In particular, no severe deviation in the boundary layer properties is introduced through the two-dimensional simulation.

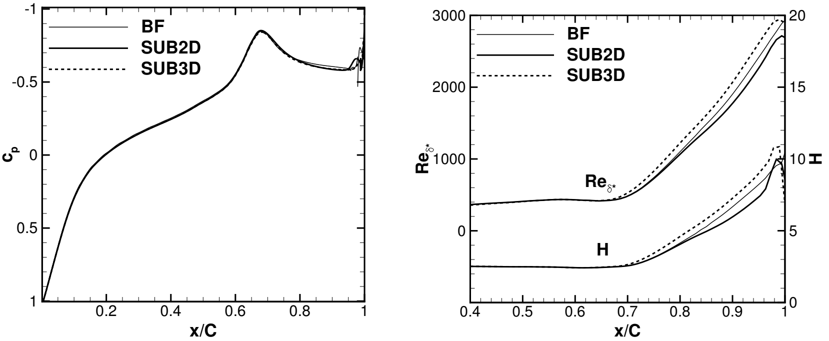

Figure 4.6: Left: Pressure coefficient on the upper surface of the mirror model for cases BF, SUB2D and SUB3D. Right: Displacement thickness Reynolds number $Re_{\delta^*}$ and shape factor $H$ for cases BF, SUB2D and SUB3D.

### 4.4.2 Unsteady flow

We next visualize the unsteady flow around the trailing edge and identify the differences between the two- and the three-dimensional simulation. To this end, Fig. 4.7 displays contours of the instantaneous spanwise component of vorticity $\Omega_z$ for SUB2D (top) and SUB3D (bottom). In both cases the formation of Kelvin-Helmholtz vortices can be observed, which begin to roll up from the separated shear layer shortly upstream of the trailing edge. The two-dimensional simulation restricts the vortices to the spanwise direction, whereas in the three-dimensional case they progressively break down into smaller structures downstream of the trailing edge. However, in the direct vicinity of the trailing edge, where we expect the most important contribution to the acoustic radiation, the vortex structures shown for SUB3D appear predominantly two-dimensional and quite similar to the ones belonging to SUB2D.

To obtain insight into the three-dimensional structure of the shear layer flow for case SUB3D, we plot isosurfaces of the $Q$ criterion in Fig. 4.8. The figure reveals that the initially two-dimensional nature of the separated flow is indeed maintained almost up to the trailing edge, where the rollers are abruptly augmented with small-scale streamwise-oriented vortex tubes.

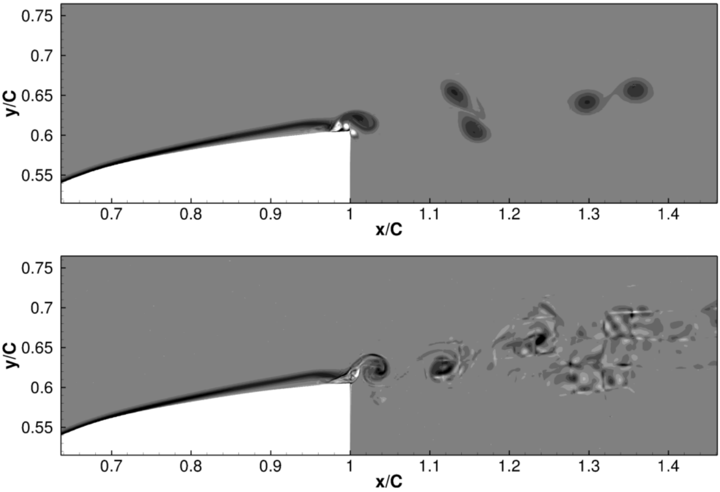

Figure 4.7: Contours of instantaneous spanwise vorticity $\Omega_z$ for SUB2D (top) and SUB3D (bottom). The 10 contour levels range between $-200 \leq \Omega_z C/u_\infty \leq 200$.

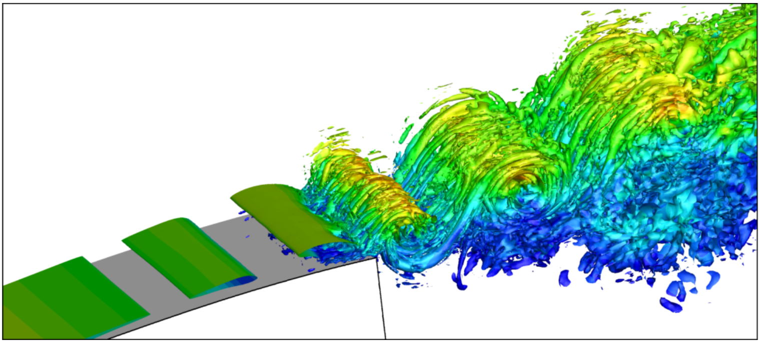

Figure 4.8: Isosurfaces of the $Q$ criterion for $Q = 50(u_\infty/C)^2$ colored with velocity magnitude $|\vec{v}|$ for a random instant of simulation SUB3D.

This late appearance of three-dimensional effects might be the reason for the low influence of three-dimensionality on the mean flow. Despite the immediate onset of three-dimensional flow features, the spanwise vortices are still discernible in the turbulent shear layer downstream.

The production of streamwise vorticity upon the saturated two-dimensional Kelvin-Helmholtz vortices is a typical phenomenon observed in separated laminar shear layers and bluff-body wakes, which can determine the path to turbulence in these flows. Jones et al. [54] describe a self-sustaining instability mechanism explaining the sudden onset of these three-dimensional structures in a nominally two-dimensional flow field.

### 4.4.3 Acoustic emissions

The scattering process at the trailing edge is visualized in Fig. 4.9 (left) for case SUB2D by means of fluctuation pressure contours. As expected, acoustic radiation is caused by the scattering of the Kelvin-Helmholtz vortices at the trailing edge. Due to the comparatively long acoustic wavelengths at this low Mach number, an acoustic wave pattern cannot be clearly recognized. Fig. 4.9 (right) shows PSD spectra of pressure at the trailing edge (marked with 'TE') and at the probe position marked with a circle in Fig. 4.9 (left) for SUB2D and SUB3D. Signal processing is carried out with the same parameters as detailed in Section 4.3.2. The signal durations for SUB2D and SUB3D are $180T^*$ and $65T^*$, respectively.

As opposed to the multiple peaks in the spectrum obtained from the simulation of the full configuration (case BF, see Fig. 4.5 (right)), both acoustic spectra (marked with 'ac.') are characterized by a single dominant peak at about 2500-2600 Hz and its harmonics for both subdomain runs. At this point, the exact reasons for this different behavior between the BF and subdomain simulations remain unclear. Nonetheless, it should be kept in mind that the current subdomain setup enforces a completely steady base flow free of disturbances, whereas in case BF unsteadiness on a whole bandwidth of length and time scales is induced by the turbulent wake flow.

The trailing edge spectra are overall similar between SUB2D and SUB3D, including the level of the dominant peak. In contrast, in the acoustic spectrum of case SUB3D, the broadband level is significantly lower compared to the two-dimensional case, while the peak levels remain similar. This result can be connected to the sudden appearance of three-dimensional flow features in the vicinity of the trailing edge. The scattering process seems to be most efficient for spanwise coherent structures, which retain the amplitudes of the two-dimensional

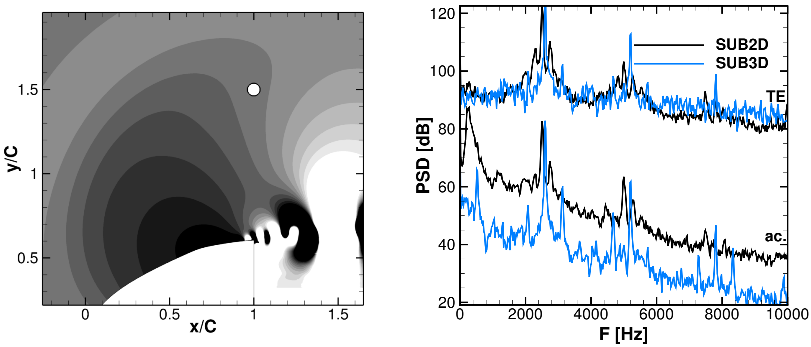

Figure 4.9: Left: Contours of instantaneous fluctuation pressure $c_p - \langle c_p \rangle$ with 11 levels ranging between $\pm 0.02$ for case SUB2D. Right: PSD spectrum of pressure at $\vec{x} = (1.0C, 0.6C)^T$ (TE) and $(1C, 1.5C)^T$ (ac.) for simulations SUB2D and SUB3D. Reference value $p_{\text{ref}} = 4 \cdot 10^{-10}\text{Pa}^2/\text{Hz}$.

case in the scattered field. Three-dimensional eddies, which contain part of the fluctuation energy in the three-dimensional case, are apparently scattered less efficiently.

In addition, in the acoustic spectrum of SUB3D, two side peaks can be clearly identified. The global stability analysis in Section 4.6 suggests these side peaks are the result of global feedback instabilities. In contrast, the weaker side peaks found for case SUB2D have a smaller frequency spacing of about 220 Hz. Evaluation of the temporal fluctuation spectra in the separated shear layer at the trailing edge reveals a flapping of the shear layer at 220 Hz, which is reflected in the high amplitude peak at that frequency in the acoustic spectrum. Thus, the side peaks found for SUB2D most likely are the result of a nonlinear interaction between the flapping and the main tonal frequency.

To conclude, it was shown that the subdomain simulations successfully describe the tonal noise generation mechanism found for the original side mirror in Chapter 3 in a reduced configuration. The impact of three-dimensional effects on the mean flow and the tonal noise generation mechanism appears to be relatively weak for the current configuration due to the late onset of three-dimensional flow features, which only emerge in the vicinity of the trailing edge. The restriction to two space dimensions seems to affect mainly the efficiency of the scattering mechanism for the broadband spectrum. It only slightly changes the tonal peak frequency while not significantly altering the peak amplitude. Thus, two-dimensional simulations sufficiently describe the relevant effects for our purposes.

## 4.5 Ladder structure

In experiments [3,93,111], the variation of the discrete frequencies with respect to the free-stream velocity in a so-called ladder structure (cf. Section 1.1) is one of the most important indicators for tonal noise generation via an acoustic feedback mechanism. However, no attempt to analyze this characteristic feature in a numerical simulation could be found in literature, maybe due to the high computational effort necessary to evaluate a reasonable range of free-stream velocities. The comparatively inexpensive two-dimensional subdomain setup offers the opportunity to examine the behavior of the tonal noise generation mechanism for the case of the mirror model in a clean, idealized setup free of background noise. The main question here is whether the typical ladder structure features known from experiments can be reproduced in a numerical simulation and how the tones compare to the frequencies predicted by a theoretical model based on the phase condition (cf. Section 3.5.5).

In order to allow for variable free-stream velocities in the subdomain simulation, the base flow solution enforced at the farfield boundary conditions and used for the sponge zone is adjusted in the following fashion

$$\begin{aligned} \vec{v}(\vec{x}, u_\infty) &= \frac{u_\infty}{u_{\infty,\mathrm{BF}}} \vec{v}_{\mathrm{BF}}(\vec{x}), \\ p(\vec{x}, u_\infty) &= p_\infty + \left( \frac{u_\infty}{u_{\infty,\mathrm{BF}}} \right)^2 \left( p_{\mathrm{BF}}(\vec{x}) - p_{\infty,\mathrm{BF}} \right), \end{aligned} \tag{4.1}$$

where the subscript 'BF' marks the original solution obtained at $u_{\infty,\mathrm{BF}} = 27.78\,\mathrm{m\,s^{-1}}$ described in Section 4.3 interpolated on the subdomain grid. Thus, the base flow velocity is simply scaled to the desired freestream velocity. The corresponding pressure field is calculated such that the resulting pressure coefficient matches the one obtained from the original base flow simulation. 25 simulations were conducted to cover the range $10 \leq u_\infty \leq 45\,\mathrm{m\,s^{-1}}$ using the setup SUB2D detailed in Table 4.1. Each run is initialized with the appropriate base flow according to (4.1) and run for 0.05 s corresponding to

$20T^*$ at $u_\infty = 27.78\,\mathrm{m\,s^{-1}}$ to wash out initial transients. PSD spectra are obtained in the manner described in Section 4.3.2 using a time window of 0.45 s or $180T^*$ at $u_\infty = 27.78\,\mathrm{m\,s^{-1}}$.

## 4.5.1 Acoustic results

The resulting PSD spectra at the probe position indicated in Fig. 4.9 (left) are plotted over $u_\infty$ in Fig. 4.10. The free-stream velocities of the individual simulations are marked with circles at the upper border of the plot. As expected, tonal components rising with the free-stream velocity can be observed from about $u_\infty = 15\,\mathrm{m\,s^{-1}}$. The highest frequency peaks clearly seen for $u_\infty \approx 27\,\mathrm{m\,s^{-1}}$ and higher are harmonics of the fundamental tones. The tone frequencies vary in agreement with typical experimental trends for the NACA 0012 airfoil $u_\infty^{0.8}$ [89] to $u_\infty^{0.85}$ [3]. Although the main tone (2620 Hz at $27.78\,\mathrm{m\,s^{-1}}$) stays dominant over a wide range of free-stream velocities, the plot shows an overlapping region of two tones between $25 \leq u_\infty \leq 28\,\mathrm{m\,s^{-1}}$. Starting at about $u_\infty \approx 35\,\mathrm{m\,s^{-1}}$, a higher frequency tone appears as a side peak somewhat weaker than the main tone. To summarize, the tones predicted by the simulation exhibit the qualitative features of the ladder structure, namely the occurrence of multiple peaks (excluding harmonics) and jumps between different tone frequencies.

As opposed to these computational results, the experimental spectra for the model mirror show up to four simultaneous tones at a given velocity [117]. Since the simulation of the complete configuration BF also developed multiple tones – albeit at different frequencies – the excitation of these additional tones might be promoted by the unsteady wake flow. In addition, the comparison of the acoustic spectra for cases SUB2D and SUB3D in Fig. 4.9 (right) showed that the two-dimensional simulation approach yields stronger broadband levels in the acoustic field, obscuring potential side peaks which are captured in the three-dimensional case. Hence, the predominant single-tone behavior found in Fig. 4.10 seems to be a consequence of the artificial, steady mean flow imposed by the subdomain boundary conditions and the restriction to two space dimensions.

## 4.5.2 Phase condition

As stated in Section 3.5.5, the tone frequencies can be predicted using theoretical models typically based on the phase difference over one loop cycle. We employ the phase condition (3.3) as a complementary means to the global stability analysis carried out for the side mirror in Section 3.5.3 to seek evidence for the

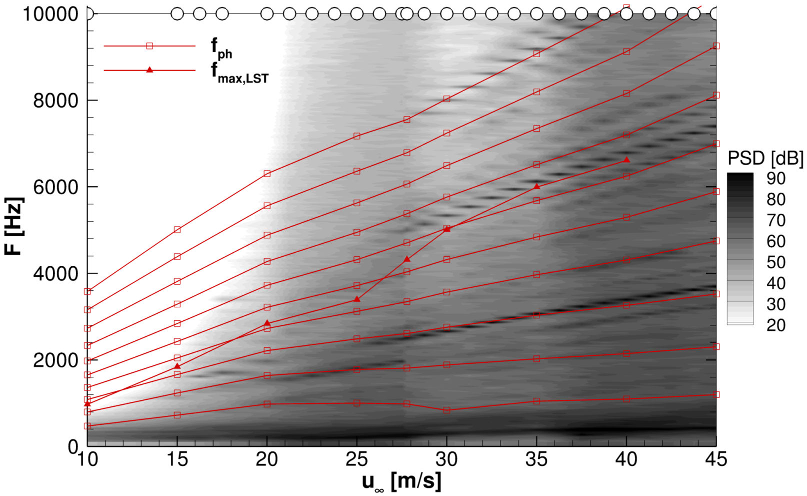

Figure 4.10: Campbell diagram for the PSD of pressure at the probe position indicated in Fig. 4.9 (left), envelope of the most amplified frequency $f_{\mathrm{max,LST}}$ and the frequencies predicted by the phase condition $f_{\mathrm{ph}}$ (eq. (4.2)). Reference value $p_{\mathrm{ref}} = 4 \cdot 10^{-10}\mathrm{Pa}^2/\mathrm{Hz}$.

feedback mechanism. The condition reads as

$$2\pi f_{\mathrm{ph}} \left( \frac{d}{u_{\mathrm{ph}}(f_{\mathrm{ph}})} + \frac{d}{c - \overline{u}_{\delta}} \right) + \varphi_d = 2\pi k, \tag{4.2}$$

where $k$ is an arbitrary integer. The mean velocity at the edge of the boundary layer $\overline{u}_{\delta}$ and the speed of sound $c$ are known from the respective mean flow, while the phase velocity of the convective instability $u_{\mathrm{ph}}(f)$ is computed from the time-averaged velocity profiles using the LST solver described in Section 2.6.1. The solver is employed with 110 collocation points and a domain spanning 30 local displacement thicknesses. Newton's method combined with spline interpolation of the tabulated LST data then solves for the frequencies $f_{\mathrm{ph}}(k)$ which fulfill the condition at a given free-stream velocity and $k$.

The two remaining unknowns are the overall phase delay $\varphi_d$ and the distance between the effective acoustic receptivity position and the trailing edge, $d$.

Due to the dependency of the former on the unknown phase shift of the receptivity process, we simply apply $\varphi_d = 2\pi$ as suggested by Plogmann et al. [93]. Concerning the receptivity position, recall that the analysis of the original side mirror clearly showed that the relevant part of the receptivity process takes place shortly downstream of the DE due to the rapid streamwise adjustment of the boundary layer in that region. The DE of the mirror model is located at $x_{\mathrm{DE}}/C = 0.67$. A good fit with the tone frequencies is achieved with $x_R/C = 0.69$ corresponding to $d = 22.1\,\mathrm{mm}$. This yields the set of curves labeled $f_{\mathrm{ph}}(k)$, which are superimposed over the Campbell diagram in Fig. 4.10. Given the assumptions and simplifications involved in the theoretical model, the tonal frequencies agree well with the theoretical ones in terms of frequency spacing and slope. The side peaks visible for $u_\infty \geq 35\,\mathrm{m\,s^{-1}}$ are of considerably smaller frequency spacing than the theoretical feedback modes. As noted in Section 4.4.3, these side peaks most likely originate from the nonlinear interaction of the main tone with a slow flapping of the shear layer.

For comparison, the most amplified frequency according to LST, $f_{\mathrm{max,LST}}$ is also plotted in Fig. 4.10. As already observed and discussed in the mirror case in Section 3.5.2, the tone frequencies stay well below $f_{\mathrm{max,LST}}$ for all considered free-stream velocities. The same behavior was found in the experimental analysis of the mirror model [117] and previously in the DNS of the NACA 0012 airfoil [56]. Therein, it was attributed to the frequency dependency of the receptivity and trailing edge scattering processes.

The above results demonstrate that the typical ladder structure features are retained in the simulation. Furthermore, the tonal peaks vary in good approximation in the manner the theoretical feedback model predicts, strongly supporting the notion of a feedback loop as frequency selection mechanism. Two different processes producing side peaks are observed in the same simulation, namely the excitation of multiple, essentially linear feedback instabilities and the nonlinear interaction of the dominant tone with a slow oscillation of the shear layer.

## 4.6 Stability analysis

In the preceding section, a theoretical feedback model was used to predict the computationally obtained tone frequencies. A global stability analysis represents an alternative and more direct means to reveal the global feedback instability that presumably selects the discrete frequencies. To that end, the current section is devoted to the application of the impulse response analysis used in

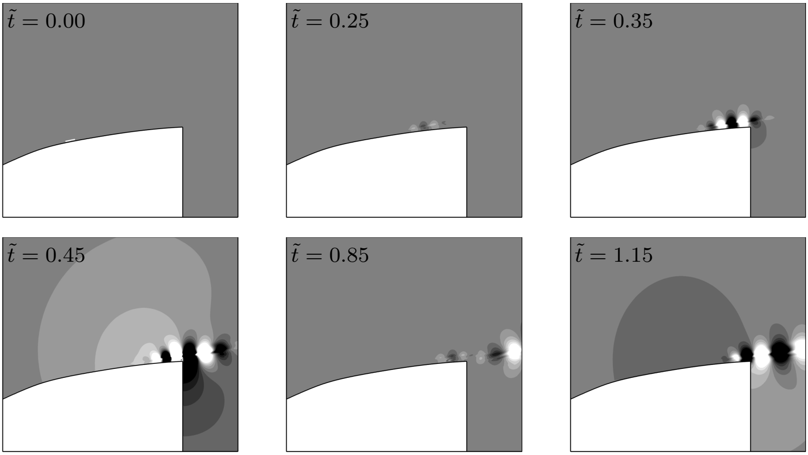

Figure 4.11: Visualization of the wavepacket time evolution by means of density perturbation contours with $-1 \cdot 10^{-8} \leq \rho' \leq -1 \cdot 10^{-8}$.

Section 3.5.3 to the mirror model.

In order to directly visualize the global instability evoked through acoustic feedback, we perform a disturbance simulation as introduced in Section 2.6.2 on the time-averaged flow from case SUB2D at $u_\infty = 27.78\,\mathrm{m\,s^{-1}}$ using the computational parameters listed in Table 4.1, except for the de-aliasing, which is switched off, i.e. $N = M = 7$, for the reasons outlined in Section 3.5.3. An increment of $U'(t=0)/U_\infty = 10^{-8}$ in density and the velocity components is initialized in the DG element adjacent to the wall at $x/C = 0.7$. We found a considerable impact of the initial disturbance position on the results and a position close to the point of separation seems to most efficiently excite the dominant global modes.

The early response of the flow is visualized using perturbation density contours in Fig. 4.11 at representative time instants $\tilde{t} = t\frac{u_\infty}{C}$. A wavepacket is seen to emerge from the initial disturbance, which leads to sound radiation upon convection over the trailing edge ($\tilde{t} = 0.45$). At the next shown instant, $\tilde{t} = 0.85$, a second hydrodynamic wavepacket develops in the separated shear layer, which subsequently causes sound emissions visible at $\tilde{t} = 1.15$.

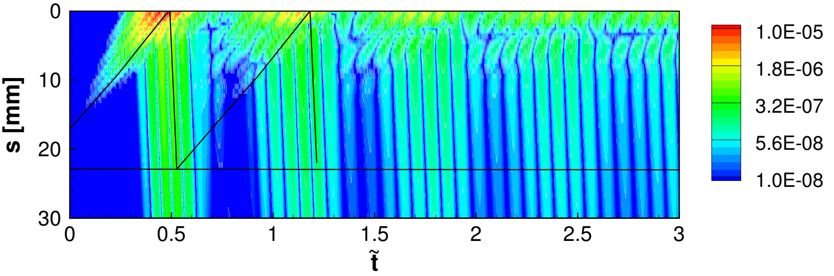

Figure 4.12: Contours of the perturbation wall pressure $|p'/p_\infty|$ plotted over the wall-tangential coordinate $s$ and time $\tilde{t}$. The contours are distributed exponentially to cover the amplitude range.

In order to better illustrate the space-time development of the disturbance, contours of the perturbation wall pressure are shown in Fig. 4.12 along the wall-tangential distance to the trailing edge $s$ depicted in Fig. 4.1. The downstream convecting and strongly amplified initial wavepacket can be spotted clearly as well as the subsequent acoustic upstream running wavepacket. Although the early development of a second hydrodynamic wavepacket is partly hidden by the preceding superimposed upstream running acoustic wavepacket, it is clearly visible from about $\tilde{t} = 0.7$. The approximate trajectories of the first wavepackets are drawn into the figure and suggest the second wavepacket and the following downstream running disturbances are initiated by the upstream running acoustic waves through acoustic receptivity around $s \approx 23\,\mathrm{mm}$ or $x/C \approx 0.67$, close to the receptivity position chosen for the phase condition model in the preceding section. Similar to the disturbance investigation at the original mirror in Section 3.5.3, the discrete wavepacket character of the signal is lost towards later times and merges into a continuous wave pattern.

These results reveal the action of acoustic feedback effects in the separation region at the model mirror. The next step is to identify the frequencies selected through this global instability using the DMD algorithm. To that end, we use a total of 501 snapshots of the disturbance calculation in the time interval $0 \leq \tilde{t} \leq 5$ with $\Delta\tilde{t} = 0.01$, yielding a dimensional sampling frequency of approximately 40 kHz. In the resulting Ritz spectrum shown in Fig. 4.13, all Ritz values lie below the imaginary axis, which implies that the associated global modes are damped. This behavior was also found in a global stability analysis

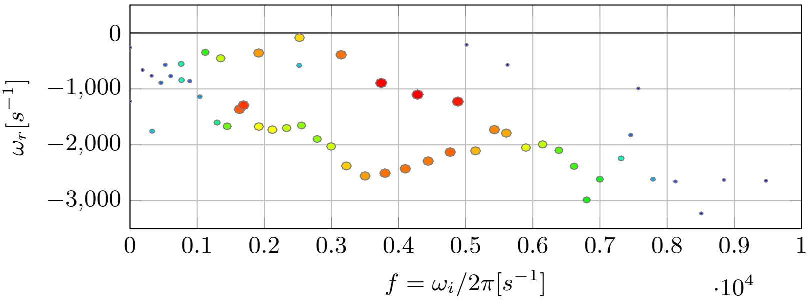

Figure 4.13: Spectrum of Ritz values delivered by the DMD algorithm based on the perturbation simulation in the time interval $0 \leq t \leq 5$. Size and color coding indicate the Euclidean norm $||\hat{\mathbf{k}}_j||$ of the respective mode. The symmetric complex conjugate part is omitted.

of a NACA 0012 airfoil carried out by Fosas de Pando et al. [32]. In their simulation, the corresponding developed flow nonetheless exhibited a number of tonal peaks in the acoustic spectrum, which corresponded accurately to the leading (least damped) global modes. The at most neutral growth rates are not unexpected when recalling the discussion in Section 3.5.1. Most likely, they are the consequence of the time-averaged base flow.

The spectrum contains a continuous branch of damped modes ranging from 0 to about 7000 Hz and a group of superimposed modes of significantly lower damping, which are regularly spaced between 1400 and 5000 Hz. Thus, we apparently retrieve the modes possessing the proper overall phase difference to be reinforced through the feedback mechanism. The frequency of the least damped feedback mode, 2525 Hz matches the peak frequency in the developed flow of 2510 Hz (case SUB2D in Fig. 4.9 (right)), which evidences that this global stability mechanism governs the dynamics also in the developed, nonlinear flow. Moreover, the two adjacent peaks at 1917 and 3145 Hz show a similar frequency spacing as the side peaks of case SUB3D in Fig. 4.9 (right), suggesting that these side peaks are the footprints of the neighboring feedback modes identified in the global stability analysis.

The feedback frequencies and frequency spacings obtained from this global stability analysis can be compared to the ones predicted by the phase condition in Table 4.2. The trends in both quantities are similar over a wide range of

| k | | | 3 | 4 | 5 | 6 | 7 |
|---|---|---|---|---|---|---|---|
| $f$ | [Hz] | DMD | 1122 | 1917 | 2525 | 3145 | 3743 |
| $f$ | [Hz] | phase cond. | 986 | 1814 | 2613 | 3348 | 4037 |
| $\Delta f$ | [Hz] | DMD | – | 795 | 608 | 620 | 598 |
| $\Delta f$ | [Hz] | phase cond. | – | 828 | 799 | 735 | 689 |

Table 4.2: Feedback frequencies $f_k$ and spacings $\Delta f = f_k - f_{k-1}$ according to the global stability analysis using DMD and predicted by the phase condition (3.3) for $u_\infty = 27.78\,\mathrm{m\,s^{-1}}$.

frequencies. Deviations can be attributed to the simplifications of the theoretical model and the underlying linear stability solver. Interestingly, the obtained frequency spacings resemble the experimental ones, which lie between 560 and 880 Hz for $u_\infty = 27.78\,\mathrm{m\,s^{-1}}$ (Fig. 4.5 (right)). Thus, the globally dominant modes directly identified by the global stability analysis are consistent with the theoretical feedback model, even the ones not observable in the developed flow.

## 4.7 Geometrical countermeasures against feedback tones

The most obvious way to avoid tonal noise through acoustic feedback mechanisms in the transitional boundary layer is to ensure that the flow is fully turbulent when it reaches the trailing edge. A turbulent boundary layer state may either prevent coherent vortex shedding or even circumvent laminar separation altogether. This state could be be achieved by tripping devices, blowing or other kinds of flow obstruction. However, due to the convex shape of the side mirror and the associated strong favorable pressure gradient present upstream of the trailing edge, the obstacle's dimensions necessary to ensure transition may become very large. Ensuring a turbulent boundary layer state at this position with only subtle changes to the shape is difficult in general. Lounsberry et al. [77] noted for the example of a one-piece mirror that the suitability of tripping devices is also a matter of manufacturability and production tolerances. Therefore, we directly build upon the characteristics of the feedback mechanism to devise relatively subtle shape modifications to reduce or prevent tonal noise generation without altering the design dramatically. In the following we briefly discuss the five variants A-E depicted schematically in Fig. 4.14.

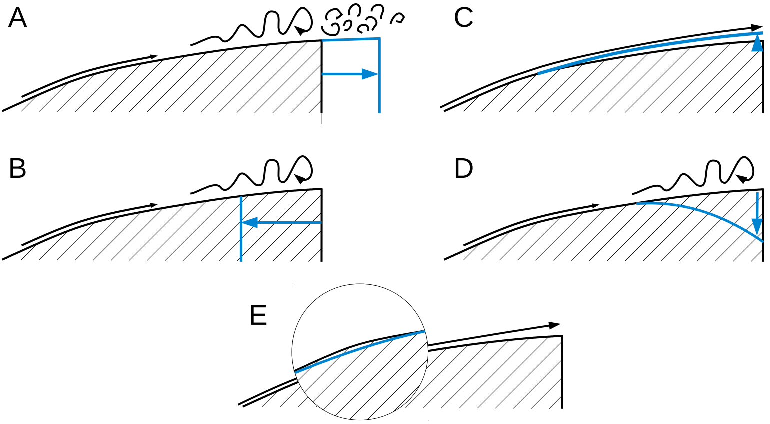

Figure 4.14: Possible modifications of the mirror model to counteract tonal noise generation.

**A**: One essential geometrical parameter is the 'amplification length', i.e. the distance between the location of first instability and the trailing edge. Starting from a baseline case which develops tones, increasing this length by prolongating the rear part of the mirror, will at some critical length lead to turbulent reattachment and at an even larger critical length to the breakdown of coherent structures at the trailing edge leading to a vanishing tone. However, this critical length is dependent on the transition scenario and the degree of free-stream turbulence.
**B**: Conversely, decreasing the amplification length by truncating the baseline geometry lowers the energy of the coherent vortices at the trailing edge. At some point, the energy input through the convective instability will not be enough for a self-sustaining oscillation, which again inhibits the tone.
**C**: Another possibility is to modify the mirror shape downstream of the baseline separation point. By lifting the contour, a favorable or at least neutral pressure gradient can be reached, such that laminar separation is avoided. The resulting attached laminar boundary is much more stable against disturbances.
**D**: A different effect can be achieved when lowering the contour downstream of the separation point. In their classical paper, Ffowcs Williams and Hall [118]

deduced a dependency of the farfield acoustic intensity $I$ on the distance $r_0$ of the source 'eddy' to the trailing edge specified as $I \propto r_0^{-3}$. Assuming that the shear layer propagates under approximately the same angle, the distance between the Kelvin-Helmholtz vortices and the trailing edge is increased when lowering the contour, which weakens the scattering process at the trailing edge. Recalling that the occurrence of the feedback mechanism is directly dependent on the scattering efficiency, it becomes clear that at some critical distance the tone again disappears.

**E**: The analyses of both the side mirror and the simplified model suggest that the flow is largely influenced by the so-called design edge. This geometric feature represents a localized surface curvature peak in the form of a rounded edge. The suction peak in the static pressure distribution leading to laminar separation appears in the direct vicinity of the DE. The results also indicate that the DE promotes receptivity to acoustic disturbances. Decreasing or eliminating the curvature peak has therefore a direct impact on the acoustic feedback loop.

Among these possible strategies, measures B, D and E were evaluated, namely truncation and lowering of the trailing edge as well as the modified DE, as they allow for a meaningful quantitative analysis. For this investigation we choose two-dimensional simulations on the subdomain with near-wall grid spacings and computational parameters listed for SUB2D in Table 4.1 and similar numbers of degrees of freedom. The free-stream velocity is set to $u_\infty = 27.78\,\mathrm{m\,s^{-1}}$ and the corresponding time periods given in Section 4.4.1 are employed to collect statistics.

### 4.7.1 Truncated trailing edge

In this subsection, we analyze modification B by seeking the critical amplification length reduction to avoid tonal noise generation and comparing it with a theoretical estimate.

Judging from the acoustic spectra resulting from the baseline geometry at selected velocities in Fig. 4.15 (left), the tone disappears for about $u_\infty \leq 15\,\mathrm{m\,s^{-1}}$. In order to get a first estimate for the necessary truncation length to remove the tone at $27.78\,\mathrm{m\,s^{-1}}$, we compare the streamwise development of the overall $N$ factor for the two free-stream velocities in Fig. 4.15 (right). Here, we define the overall $N$ factor as $N(s) = \max_f (n(f, s))$, where $n(f, s)$ is computed using (3.2) and LST based on the time-averaged velocity profiles with the numerical parameters given in Section 4.5.2. The resulting amplification for the higher velocity exceeds the one of the lower velocity of $N = 5.7$ at the

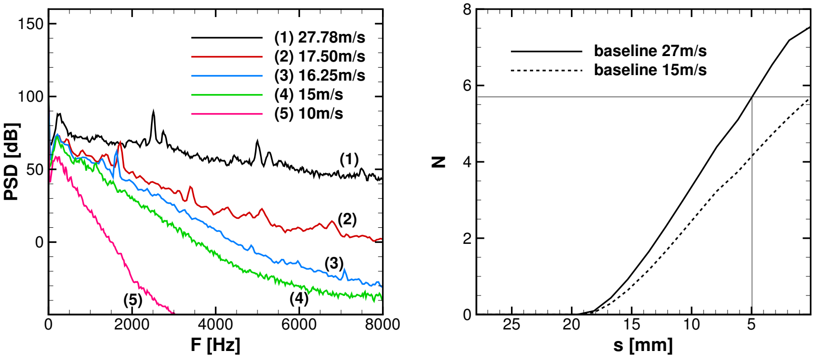

Figure 4.15: Left: acoustic spectra resulting from the baseline geometry for various free-stream velocities. Right: Corresponding $N$ factor yielded by LST for $u_\infty = 27.78$ and $15\,\mathrm{m\,s^{-1}}$. Reference value $p_{\mathrm{ref}} = 4 \cdot 10^{-10}\mathrm{Pa}^2/\mathrm{Hz}$.

trailing edge. Assuming that the base flow remains approximately the same, this amplification level is reached at the trailing edge for $27.78\,\mathrm{m\,s^{-1}}$, when truncating the mirror by 5 mm. Thus, according to this estimate the tone should vanish for $s_t \geq 5\,\mathrm{mm}$.

Fig. 4.16 (left) shows the acoustic spectra resulting from the baseline geometry and truncation variants with $s_t = 6, 7$ and 8 mm at $u_\infty = 27.78\,\mathrm{m\,s^{-1}}$. For clarity, the consecutive cases are shifted downwards by 40 dB each. With increasing $s_t$, the tonal peak first decreases in amplitude and moves towards higher frequencies and then practically vanishes for $s_t = 8\,\mathrm{mm}$ or $s/d \approx 0.35$, $d$ being the distance between DE and trailing edge. Thus, a somewhat larger truncation length than the estimated 5 mm is necessary to prevent tones. Inspection of the associated $N$ factors plotted in Fig. 4.16 (right) reveals that in the truncated cases, the shear layer amplification rises more steeply than in the baseline case, leading to a higher value at the trailing edge. This explains why the estimate based on the original base flow is flawed. Furthermore, it can be noticed that the critical $N$ factor taken from the $u_\infty = 15\,\mathrm{m\,s^{-1}}$ case ($N = 5.7$) is still surpassed at the trailing edge for $s_t = 8\,\mathrm{mm}$, although the tone is essentially gone. Therefore, apart from the convective amplification capacity,

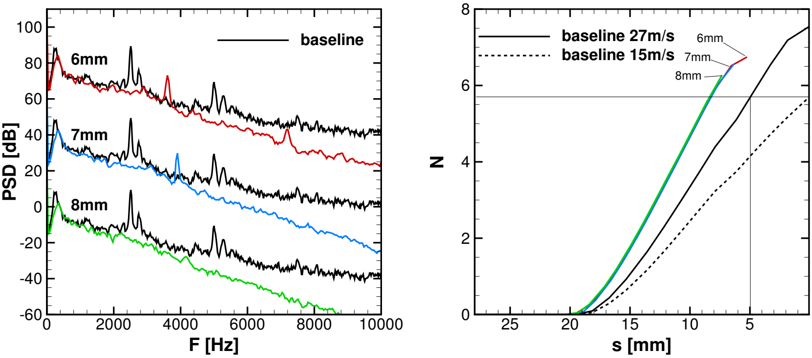

Figure 4.16: Left: acoustic spectra for the truncated trailing edge with $s_t = 6, 7$ and $8\,\text{mm}$ at $u_\infty = 27.78\,\text{m}\,\text{s}^{-1}$. For clarity, the consecutive cases are shifted by $40\,\text{dB}$ each. Right: $N$ factor yielded by LST for the baseline and truncated geometries at $u_\infty = 27.78$ and $15\,\text{m}\,\text{s}^{-1}$. Reference value $p_{\text{ref}} = 4 \cdot 10^{-10}\text{Pa}^2/\text{Hz}$.

the characteristics of the other mechanisms contributing to the tone generation must have been altered through the geometric modification.

In order to identify the base flow modification leading to the increased growth rates, Fig. 4.17 shows the wall-normal position of the inflection point $y_I$. The shear layer is observed to spread considerably faster if the trailing edge is truncated. According to the linear stability analysis of inflectional velocity profiles reported in Dovgal et al. [25], larger wall-normal distances of the inflection point are associated with increased instability growth rates. This base flow modification might also explain the diminished tone at $s_t = 8\,\text{mm}$ despite the comparatively high $N$ factor in this case. As the Kelvin-Helmholtz vortices travel approximately along the connecting line of the inflection points of the shear layer, which shift away from the wall, we can expect the trailing edge scattering mechanism to become less efficient. This aspect is exploited to prevent the tones in the following subsection.

To conclude, tones can be reduced to acceptable levels by decreasing the amplification length through truncation. However, the simulations demonstrate that massive base flow modifications should be expected even for slight changes

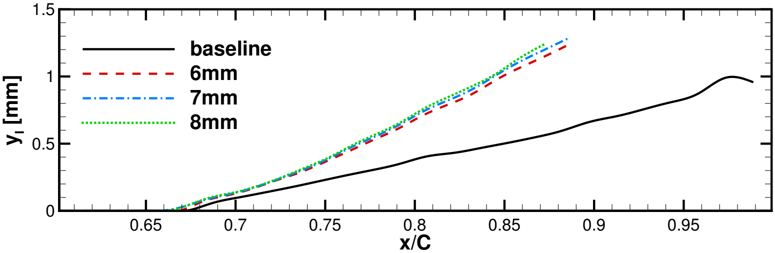

Figure 4.17: Streamwise distribution of the wall-normal position of the inflection point $y_I$ for the truncated trailing edge cases at $u_\infty = 27.78\,\mathrm{m\,s^{-1}}$.

in the geometry. Besides decreasing the amplification length, in the current simulations truncation leads to an outwards-shifting of the shear layer, which causes two competing trends: (i) increasing growth rates and (ii) decreasing scattering efficiency. The interplay between both determines whether a tone develops or not, significantly complicating faithful design estimates.

### 4.7.2 Lowered trailing edge

As already noted in the preceding subsection, the distance between the shed vortices and the trailing edge is a crucial parameter determining the scattering efficiency. With modification D, we directly target the scattering efficiency through lowering of the trailing edge and thereby increasing this distance. The trailing edge is lowered by modifying the shape downstream of the point of separation using a spline interpolant that is tangentially constant at the transition point. Fig. 4.18 shows the resulting variants with $l = 1, 2, 3$ and 5 mm. In order to minimize the influence on the upstream flow and isolate the effect of the lowered trailing edge, the modified contour starts downstream of the baseline separation point S.

The acoustic spectra obtained for the above variants from two-dimensional simulations at $u_\infty = 27.78\,\mathrm{m\,s^{-1}}$ are compared to the baseline case in Fig. 4.19 (left), where again the consecutive cases are shifted by 40 dB each. Interestingly, a lowering by 1 mm already leads to a noticeable reduction of the tone. For lowerings of 3 and 5 mm, the tone vanishes completely. Quite unexpectedly, this trend is interrupted by the $l = 2$ mm simulation, where a high amplitude tone

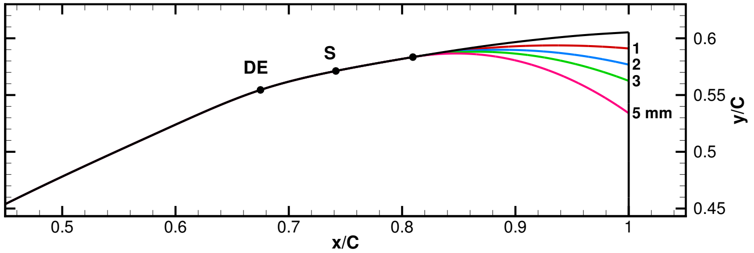

Figure 4.18: Lowered trailing edge configurations.

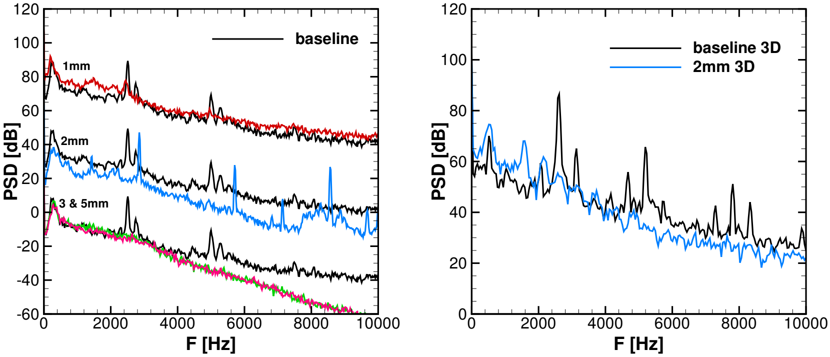

Figure 4.19: Acoustic spectra with lowered trailing edge at $u_\infty = 27.78\,\mathrm{m\,s^{-1}}$. For clarity, the consecutive cases are shifted by 40 dB each. Left: two-dimensional simulations, right: three-dimensional simulations. Reference value $p_{\mathrm{ref}} = 4 \cdot 10^{-10}\mathrm{Pa}^2/\mathrm{Hz}$.

appears. This variant was repeated using a three-dimensional setup similar to SUB3D in Table 4.1, which led to diminished tone amplitudes compared to the three-dimensional baseline case (Fig. 4.19 (right)).

The effect of the modified geometry on the boundary layer is illustrated in Fig. 4.20 by means of the wall-normal position of the mean velocity profile inflection point $y_I$, which again serves as a measure for the trajectory of the

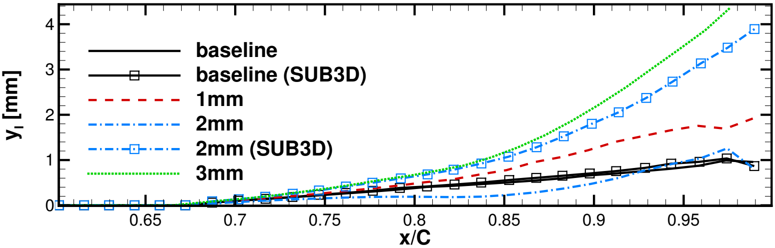

Figure 4.20: Mean inflection point position $y_I$ for the lowered trailing edge configurations.

Kelvin-Helmholtz vortices. For all simulations except the two-dimensional $l = 2\,\mathrm{mm}$ case, the desired effect of a more distant shear layer is evident. In the $l = 2\,\mathrm{mm}$ case, the shear layer is located even closer to the wall as in the baseline case for $x/C \leq 0.94$. Downstream, its distance to the wall is comparable to the one found for the baseline case.

Fig. 4.20 shows snapshots of the instantaneous distribution of spanwise vorticity for the considered cases. Therein, the general trend found in the inflection point distribution is retrieved in the increasingly distant shear layer and the associated rolled-up vortices.

The case $l = 2\,\mathrm{mm}$ (SUB2D) represents an exception: here the separated shear layer is bent and remains close to the wall. We observe rolled-up vortices earlier than in the baseline case. In this particular configuration, the action of these vortices seems to cause the shear layer to remain close to the wall. In contrast, the shear layer in the three-dimensional case diverges from the wall along a straight line. Downstream, diffusion of spanwise vorticity as a result of the build-up of smaller three-dimensional structures can be noticed. If these three-dimensional effects are taken into account in the $l = 2\,\mathrm{mm}$ case, the flow follows the trend of the other cases. For that reason, the two-dimensional simulation of the $l = 2\,\mathrm{mm}$ case is discarded. Comparing the inflection point distributions in Fig. 4.20 for the two- and three-dimensional baseline case suggests a low influence of the Kelvin-Helmholtz vortices on the mean flow, if their saturation occurs not significantly upstream of the trailing edge. Furthermore, the larger lowering case $l = 3\,\mathrm{mm}$ illustrates how the effect of the saturated vortices on the mean flow weakens with increasing wall-normal distance.

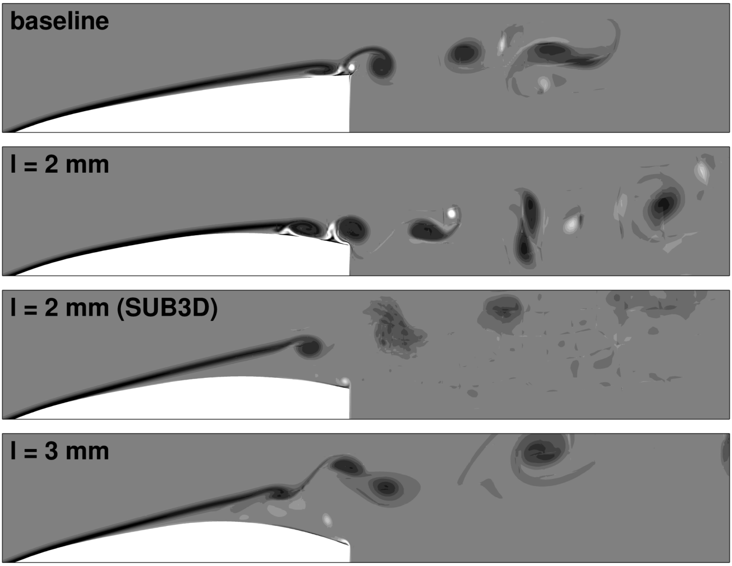

Figure 4.21: Instantaneous snapshots of spanwise vorticity contours for these configurations with $-200 \leq \Omega_z C/u_\infty \leq 200$.

This analysis reveals the high potential of trailing edge lowering for tone reduction. A slight lowering by $l = 1\,\text{mm}$ already decreases the tone by approximately 5 dB and – referring to the three-dimensional simulation – it is practically absent for $l = 2\,\text{mm}$, which corresponds to about one trailing edge boundary layer thickness of the baseline case ($\delta_{99} \approx 1.8\,\text{mm}$). Second, the non-monotonic behavior and strong discrepancy between the two- and three-dimensional simulations in the $l = 2\,\text{mm}$ case demonstrate one of the limits of the two-dimensional approach. In this particular case, three-dimensional effects seem to be critical.

### 4.7.3 Modified design edge

In this section, we analyze how modifications to the DE of the mirror model affect flow and noise generation, while keeping the remainder of the shape as

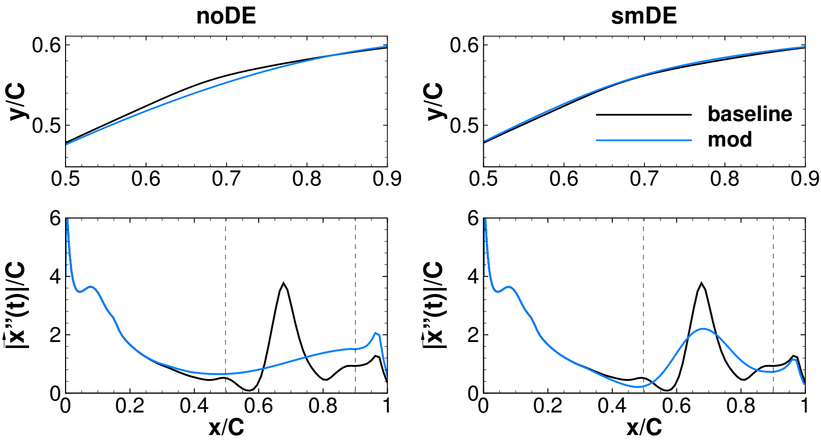

Figure 4.22: Top row: modified contours, bottom row: magnitude of the corresponding second derivatives $|\vec{x}''(t)| = |\frac{d^2\vec{x}}{dt^2}|$.

close as possible to the baseline model. Two variants are considered. The first variant termed noDE is a shape where the local curvature peak is eliminated and replaced by a smooth curvature variation. In order to evaluate the influence of its 'sharpness', the curvature peak is stretched out for the second variant smDE.

Both modifications are realized as follows. The contour from leading edge to trailing edge is sampled using 1000 points spaced equidistantly along the normalized arc length $t \in [0, 1]$. The first and second derivatives of the parametrization $\vec{x}(t)$ are approximated using central second order finite differences.

When looking at the magnitude of the second derivative $|\vec{x}''(t)|$ of the baseline shape plotted in the bottom left panel of Fig. 4.22, the DE manifests as a peak at $x/C \approx 0.68$. To control the curvature, the peak in $\vec{x}''(t)$ is bypassed using spline interpolation between $x/C = 0.5$ and 0.9 to obtain a flat distribution $\tilde{x}''_{\mathrm{mod}}(t)$. To ensure that the resulting contour $\vec{x}_{\mathrm{mod}}(t)$ reaches the same end point $\vec{x}(1)$ as the original one, the modified second derivative is scaled in the following way. For the first component of $\vec{x}(t) = (x(t), y(t)),^T$ we set

$$x''_{\mathrm{mod}}(t) = (1 + c_x \cdot \phi(t)) \cdot \tilde{x}''_{\mathrm{mod}}(t). \tag{4.3}$$

where $\phi(t)$ is a shape function smoothly blending from 0 to 1 between $t = 0.2$ and 0.7. Integration over $t$ two times gives

$$x_{\mathrm{mod}}(t) = x(0) + \int_0^t \left( x'(0) + \int_0^{\tilde{t}} x''_{\mathrm{mod}}(\hat{t})\, d\hat{t} \right) d\tilde{t} \tag{4.4}$$

which is evaluated numerically using the trapezoidal rule. The factor $c_x$ is chosen to fulfill

$$x_{\mathrm{mod}}(1) = x(1). \tag{4.5}$$

Repeating this procedure for the $y$ component delivers the modified shape termed noDE shown in the left column of Fig. 4.22.

For the second variant smDE, we start from the bypassed second derivative $\tilde{x}''_{\mathrm{mod}}(t)$ and augment it with a modified exponential function

$$x''_{\mathrm{mod}}(t) = \tilde{x}''_{\mathrm{mod}}(t) + \Delta x''_P (1 - b(t - t_{\mathrm{DE}})^2) \cdot \mathrm{e}^{-b(t-t_{\mathrm{DE}})^2} \tag{4.6}$$

to model the DE curvature peak with the ability to control its peak value at $t_{\mathrm{DE}}$ via $\Delta x''_P$. Here, matching end points are ensured by choosing the width parameter $b$ so that (4.5) is satisfied. The value of $b$ is obtained using Newton's method over (4.5). This procedure results in a widening of the peak for desired peak values lower than in the baseline case. The contour labeled smDE shown in the right column of Fig. 4.22 was constructed in this manner. Although it is hardly distinguishable from the baseline shape, it exhibits a 68 % larger radius of curvature of $r_C(t_{\mathrm{DE}}) = 48.6\,\mathrm{mm}$ compared to the baseline value of 28.9 mm. The two modified shapes are assessed in two-dimensional simulations at $u_\infty = 27.78\,\mathrm{m\,s^{-1}}$. The resulting acoustic spectra can be compared to the baseline case in Fig. 4.23 (left). For the case noDE, the tonal components have completely disappeared and the overall level of the spectrum is significantly lowered compared to the baseline case. A similar trend is noticed for case smDE, although some weaker tones remain.

Considering the $c_p$ distributions plotted in Fig. 4.23 (right), we see that case noDE exhibits only a weak trace of the suction peak present in the baseline case, which in addition appears farther downstream. For the smoothed design edge, the suction peak as well as the upstream distribution are shifted to lower values. The more even pressure distribution of case noDE leads to delayed separation at $x_S \approx 0.860$. (baseline $x_S \approx 0.760$). In contrast, the smoothed DE moves the point of separation slightly upstream to $x_S = 0.746$.

An impression of the instantaneous flow fields is given in Fig. 4.24 by means of vorticity contours for the three cases. Both modifications lead to a lifted shear

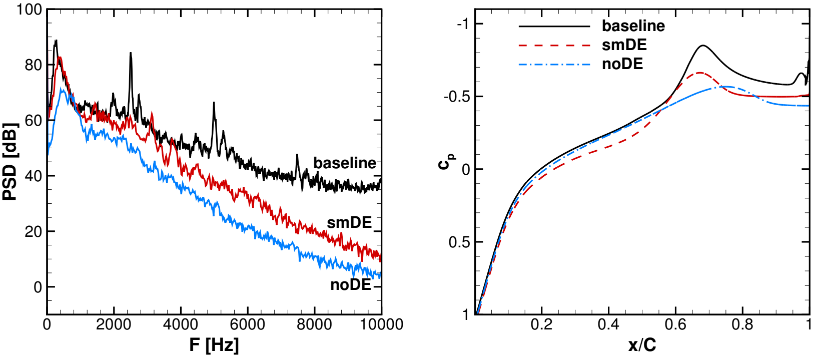

Figure 4.23: Left: Acoustic spectra for the modified DE at $u_\infty = 27.78\,\mathrm{m\,s^{-1}}$. Reference value $p_{\mathrm{ref}} = 4 \cdot 10^{-10}\mathrm{Pa}^2/\mathrm{Hz}$. Right: corresponding pressure coefficient $c_p$.

layer, quite similar to the truncated trailing edge results. As demonstrated in Section 4.7.2, this lifting of the shear layer weakens the acoustic radiation at the trailing edge. In addition, vortex shedding is inhibited for case noDE until far downstream of the trailing edge, as a consequence of the short amplification length resulting from the late separation.

The vanishing tones for the case noDE demonstrate the critical role of local curvature features in the generation of feedback tones. Local curvature peaks (i) can directly cause laminar separation, potentially giving rise to strong instability growth over a larger distance and (ii) intensify local peaks in the streamwise pressure and velocity gradients presumably enhancing receptivity.

In the smDE case, the peak curvature was decreased by redistributing the integral amount of curvature to a wider range. Although the tonal peak amplitude is decreased significantly compared to the baseline case, this modification seems to be not very robust. The tone reduction appears to be mainly caused by the higher distance of the shear layer to the trailing edge. It appears difficult to assign a limit for local curvature peaks, below which a shape feature can be deemed uncritical.

On the other hand, ensuring a shape free of local curvature maxima in the vicinity of the trailing edge effectively prevents tones in the present simulation.

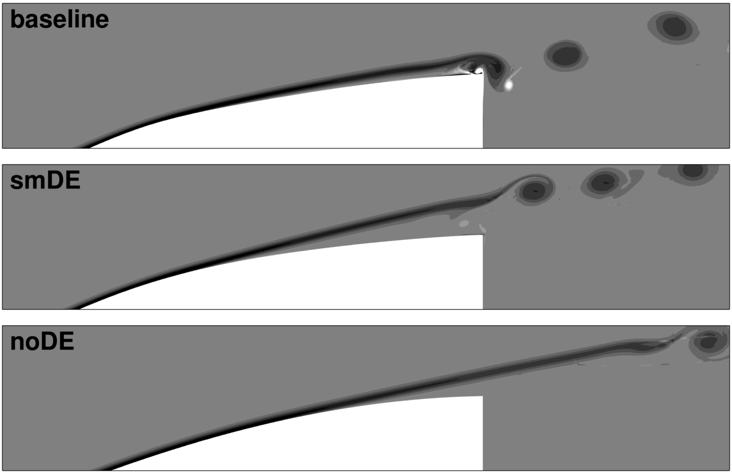

Figure 4.24: Instantaneous contours of vorticity $-200 \leq \Omega_z C/u_\infty \leq 200$ for the modified DE cases at $u_\infty = 27.78\,\mathrm{m\,s^{-1}}$.

Of course, feedback tones can also establish at smooth surfaces as in the case of the NACA 0012 airfoil. However, the above analysis demonstrates that local curvature peaks largely promote feedback tones and thus represent one of the substantial points of attack to avoid them.

## 4.8 Summary and discussion

The main findings of the present analysis of the two-dimensional mirror model are summarized below.

- In the simulation of the complete experimental configuration, we achieve reasonable agreement with the measured mean pressure distribution. The simplified mirror model is shown to mimic the flow around the mirror in the tonal noise source region. Furthermore, the general multi-peak character of the measured acoustic spectrum and similar frequency spacing between the neighboring tones are retrieved in the simulation, although the peak frequencies do not match the experimental ones.

- In contrast, the subdomain simulations yield acoustic spectra dominated by a single tone, presumably due to the artificially steady base flow imposed through the boundary conditions. Three-dimensional effects only weakly alter the mean flow and the tones in terms of frequency and level. Their main influence was found to lie in the lower broadband levels appearing in the acoustic spectra, while tone levels are not altered significantly. Due to the lower broadband levels, tonal side peaks of lower amplitude become apparent in the three-dimensional case. Overall, the two-dimensional simulation approach seems to be appropriate for this investigation. One of the lowered trailing edge variants marks a notable exception: the two-dimensional simulation predicts strong tone emissions due to the action of early saturated vortices upstream of the trailing edge that cause the separated shear layer to remain close the wall. In the corresponding three-dimensional simulation, these vortices break down to smaller three-dimensional structures, resulting in a more realistic transitional shear layer for which practically no tone appears.

- For the first time, the features of the so-called ladder structure are captured in numerical simulations. These features include the occurrence of multiple peaks (excluding harmonics) and the jumps between different modes. The peak frequencies are shown to vary with the free-stream velocity in close agreement to a theoretical model based on the acoustic feedback loop. As opposed to the experiment, a dominant single peak is observed over a wide range of free-stream velocities. The preceding item of this summary suggests that this tendency is a consequence of the steady base flow enforced in the subdomain and the lower sensitivity of two-dimensional simulations for side peaks due to the increased broadband noise level.

- An impulse response analysis helped directly visualize acoustic feedback effects and identify the effective receptivity location. The dominant global instability mode frequency computed by spectral decomposition of the response agrees well with the main tone frequency measured in the developed flow. Moreover, a surrounding group of feedback modes is captured which correspond to the respective frequencies delivered by the theoretical phase condition.

- Three possible countermeasures are selected for numerical investigation. Trailing edge truncation and lowering are both easy to implement and directly target the properties of the feedback loop. A truncation length of $t = 8\,\mathrm{mm}$ is necessary to prevent tonal noise generation at

$u_\infty = 27.78\,\mathrm{m\,s^{-1}}$. It is shown that a quantitative estimation of the necessary truncation based on the amplification properties of the baseline can fail easily, since altering the geometry affects the whole flow field. Weakening the trailing edge scattering process by lowering the trailing edge is demonstrated to be a quite efficient measure against feedback tones: lowering by only 2 mm or about one boundary layer thickness at the trailing edge removes the tones in the current setup. Finally, the influence of the local curvature peak associated with the design edge is addressed by simulations of two modified designs. The localized mean flow changes induced by the design edge are found to significantly strengthen acoustic feedback tones.

In practice, combinations of suitable modifications should be more robust and efficient, i.e. require a lower amount of truncation or lowering. Ultimately, the feedback mechanism can only occur in a very limited range of the main parameters. Departure from this range in any direction eliminates the tone. However, it is this delicateness and lack of robustness of the mechanism which makes it so difficult to identify and prevent.

# 5 Conclusions and prospects

## 5.1 Conclusions

The present work describes the computational analysis of tonal noise generation by the flow over a side mirror via high order large eddy simulations. The possibility of acoustic feedback effects driving the tone emissions marks the starting point of the investigation, necessitating the use of a compressible simulation suitable for direct noise computations. In addition, the instability dynamics in laminar and transitional boundary layers or shear layers constitute an integral component of the noise generation in this application. To accurately capture these processes at a side mirror geometry, high fidelity no-model LES are carried out using the discontinuous Galerkin spectral element method, which enables high order accurate simulations on unstructured, non-conforming grids. Tonal noise emitted from isolated airfoils was subject to a number of investigations, many of which support the notion of a self-sustaining acoustic feedback loop as underlying mechanism. The feedback loop comprises convectively amplified instabilities in a separated, laminar shear layer upstream of the trailing edge that culminate in coherent vortex shedding. The associated sound emissions continuously reinforce the instabilities through natural receptivity at some upstream position, establishing a closed loop selecting discrete frequencies. Thus, a simulation of the flow around a NACA 0012 airfoil based on the work of Jones and Sandberg [56] was chosen for validation of the present simulation framework for acoustic feedback effects.

To address the question whether the tonal components in the acoustic radiation from the side mirror can be connected to a similar mechanism, a simulation of the flow over an isolated mirror housing is conducted. Comparisons with wall pressure, hotwire and PIV measurements show that the flow field is accurately described by the simulation. Two tonal noise source regions at the inner and upper side of the mirror are identified consistent with experimental findings. At these locations, the laminar boundary layer separates shortly downstream of a rounded kink called 'design edge'. Tonal sound emissions are observed, which are caused by the periodic shedding of highly coherent Kelvin-Helmholtz vortices at the trailing edge. For one of the tone frequencies, quantitative agreement with the measurements is achieved.

A linear stability analysis determines a wide range of amplified frequencies in the separated shear layer, suggesting some additional mechanism causes the selection of discrete frequencies. Therefore, global stability and feedback effects are elucidated by studying the response to a localized small-amplitude disturbance in a perturbation simulation based on the time-averaged flow field [32, 55, 56]. The disturbance is found to excite a global acoustic feedback loop instability between the design edge and the trailing edge. A dynamic mode decomposition of the space-time response shows that discrete frequencies are selected by this mechanism. Moreover, the tone frequencies of the developed flow practically coincide with the retrieved dominant global instability frequencies. The computational analysis of the side mirror geometry thus establishes the existence of a global acoustic feedback instability leading to significant tonal noise emissions.

Having identified the principal source mechanism, the investigation is continued using a simplified mirror geometry designed in the experimental study [117], that takes into account the essentially two-dimensional nature of the mechanism. To exploit the two-dimensional shape and circumvent the computational cost stemming from the bluff body wake of the model, a subdomain approach is introduced. Simulations of the model geometry exhibit reasonable agreement to the measured mean pressure distribution, accurately reproduce the flow features in the tonal source region of the original mirror and deliver tonal components in the acoustic spectrum.

The simplified mirror is used to study the variation of the tones with increasing free-stream velocity to evaluate the ladder structure known from experimental investigations [3, 89, 111] for the first time in numerical simulations. The tonal frequencies increase with velocity and show jumps between consecutive rungs. In addition, multiple tones are obtained in parts of the velocity range. Overall, the computational results are found to mimic the experimentally observed behavior. Subsequently, the peak frequencies are shown to vary in accordance with a theoretical phase condition model [93]. Furthermore, the theoretical feedback frequencies compare favorably to the leading global instability frequencies obtained in the same manner as for the original mirror. This result connects the notion of a phase condition predetermining the leading frequencies directly to the global instability point of view: the flow exhibits a group of potential feedback modes fulfilling the phase condition, some of which establish in the developed flow.

The remaining question is how the tone frequencies are selected from a group of feedback modes. The global stability results at both mirror geometries indicate that the temporal growth rate (or equivalently the loop gain over one cycle) predominantly determines the dominant tonal frequency in the developed flow. In the linear case, this gain is determined by the shear layer amplification and the efficiencies of the trailing edge scattering and the receptivity processes [55, 56]. However, in general there seems to be a high influence of environmental conditions (free-stream turbulence, reverberation in the closed wind tunnel test-section) on the selection process, which impedes quantitative comparisons between simulation and experiment.

Based on the simplified mirror model, design modifications are investigated that aim at reducing or avoiding flow-induced tones and target at the components of the feedback loop. First, the mirror contour is truncated at the trailing edge to reduce the length over which the shear layer instabilities are amplified. The analysis shows the measure is effective for long enough truncations. Second, the trailing edge is lowered to increase the distance of the wall to the separated shear layer, inhibiting the diffraction process. Slight lowering already eliminates the tone, although the robustness of this measure is yet to be determined. Finally, simulations of the flow around shapes with decreased local curvature peaks at the design edge prove the high influence of this geometric feature, which strongly promotes the generation of acoustic feedback tones.

In summary, one main contribution of the present work is the demonstration of the relevance of acoustic feedback effects in an automotive application. The investigation is the first to provide numerical evidence of such effects for a complex geometry and to directly compare to the results of an experimental study of the same geometry. The findings may provide guidance in mirror design and in the development of future predictive tools.

## 5.2 Prospects

The present results motivate the application of the high order DGSEM framework in fundamental investigations of other aeroacoustic problems. For instance, the flow over cavities or gaps generates noise through different mechanisms with and without acoustic feedback depending on the Reynolds number and the state of the boundary layer. Furthermore, extensions of the simulation framework in two directions are particularly interesting.

One outcome of the experimental side mirror study [114] was a high sensitivity of the acoustic spectrum towards uncertain boundary conditions and free-stream turbulence. Such sensitivity can hardly be noticed in deterministic CFD simulations. For this class of problem, a possible route is the inclusion of

uncertain input data based on probabilistic simulation approaches.
Other key topics are nonlinear numerical stability and subgrid scale model design, which are both required to make accessible turbulent flows at larger Reynolds numbers. Here, no-model approaches require unfeasibly high resolutions. In that context split DG methods [38] are a promising development. They borrow ideas from summation-by-parts finite difference schemes to improve nonlinear stability. Some of these formulations could substitute the current de-aliasing technique while achieving a discretely dissipation-free operator, offering a high degree of control for SGS modeling.

# Bibliography

[1] E. Åkervik, L. Brandt, D. S. Henningson, J. Hœpffner, O. Marxen, and P. Schlatter. Steady solutions of the Navier-Stokes equations by selective frequency damping. *Physics of Fluids (1994-present)*, 18(6):068102, 2006.

[2] M. Alam and N. D. Sandham. Direct numerical simulation of 'short' laminar separation bubbles with turbulent reattachment. *Journal of Fluid Mechanics*, 403:223–250, 2000.

[3] H. Arbey and J. Bataille. Noise generated by airfoil profiles placed in a uniform laminar flow. *Journal of Fluid Mechanics*, 134:33–47, 1983.

[4] D. N. Arnold, F. Brezzi, B. Cockburn, and L. D. Marini. Unified analysis of discontinuous Galerkin methods for elliptic problems. *SIAM J. Numer. Anal.*, 39(5):1749–1779, 2002.

[5] J. Ask and L. Davidson. The sub-critical flow past a generic side mirror and its impact on sound generation and propagation. *AIAA Paper*, 2558:2006, 2006.

[6] A. Babucke. *Direct Numerical Simulations of Noise-Generating Mechanisms in the Mixing Layer of a Jet.* PhD thesis, University of Stuttgart, 2009.

[7] D. Barkley. Linear analysis of the cylinder wake mean flow. *EPL (Europhysics Letters)*, 75(5):750, 2006.

[8] F. Bassi and S. Rebay. A high order accurate discontinuous finite element method for the numerical solution of the compressible Navier–Stokes equations. *Journal of Computational Physics*, 131:267–279, 1997.

[9] F. Bassi and S. Rebay. A high-order accurate discontinuous finite element method for the numerical solution of the compressible Navier-Stokes equations. *J. Comput. Phys.*, 131:267–279, 1997.

[10] F. Bassi, S. Rebay, G. Mariotti, S. Pedinotti, and M. Savini. A high-order accurate discontinuous finite element method for inviscid an viscous turbomachinery flows. In R. Decuypere and G. Dibelius, editors, *Proceedings of 2nd European Conference on Turbomachinery, Fluid and Thermodynamics*, pages 99–108, Technologisch Instituut, Antwerpen, Belgium, 1997.

[11] A. Beck. *High Order Discontinuous Galerkin Methods for the Simulation of Multiscale Problems.* PhD thesis, University of Stuttgart, 2015.

[12] A. D. Beck, T. Bolemann, D. Flad, H. Frank, G. J. Gassner, F. Hindenlang, and C.-D. Munz. High-order discontinuous Galerkin spectral element methods for transitional and turbulent flow simulations. *International Journal for Numerical Methods in Fluids*, 76(8):522–548, 2014.

[13] A. D. Beck, D. G. Flad, C. Tonhäuser, G. Gassner, and C.-D. Munz. On the influence of polynomial de-aliasing on subgrid scale models. *Flow, Turbulence and Combustion*, pages 1–37, 2016.

[14] A. Birkefeld. *Computational aeroacoustics with a high order discontinuous Galerkin scheme.* PhD thesis, University of Stuttgart, 2012.

[15] C. Bogey and C. Bailly. A family of low dispersive and low dissipative explicit schemes for flow and noise computations. *Journal of Computational Physics*, 194(1):194–214, 2004.

[16] C. Bogey and C. Bailly. Computation of a high Reynolds number jet and its radiated noise using large eddy simulation based on explicit filtering. *Computers & fluids*, 35(10):1344–1358, 2006.

[17] C. Bogey, S. Barré, D. Juvé, and C. Bailly. Simulation of a hot coaxial jet: Direct noise prediction and flow-acoustics correlations. *Physics of Fluids (1994-present)*, 21(3):035105, 2009.

[18] J. Boris, F. Grinstein, E. Oran, and R. Kolbe. New insights into large eddy simulation. *Fluid dynamics research*, 10(4-6):199–228, 1992.

[19] C. Burstedde, L. C. Wilcox, and O. Ghattas. P4est: Scalable algorithms for parallel adaptive mesh refinement on forests of octrees. *SIAM J. Sci. Comput.*, 33(3):1103–1133, May 2011.

[20] M. Carpenter and C. Kennedy. Fourth-order 2N-storage Runge-Kutta schemes. Technical Report NASA TM 109111, 1994.

[21] T. P. Chong and P. Joseph. “ladder” structure in tonal noise generated by laminar flow around an airfoil. *The Journal of the Acoustical Society of America*, 131(6):EL461–EL467, 2012.

[22] T. Colonius. An overview of simulation, modeling, and active control of flow/acoustic resonance in open cavities. *AIAA paper*, 76:2001, 2001.

[23] T. Colonius. Modeling artificial boundary conditions for compressible flow. *Annu. Rev. Fluid Mech.*, 36:315–345, 2004.

[24] G. Desquesnes, M. Terracol, and P. Sagaut. Numerical investigation of the tone noise mechanism over laminar airfoils. *Journal of Fluid Mechanics*, 591:155–182, 2007.

[25] A. Dovgal, V. Kozlov, and A. Michalke. Laminar boundary layer separation: instability and associated phenomena. *Progress in Aerospace Sciences*, 30(1):61–94, 1994.

[26] R. Ewert and W. Schröder. Acoustic perturbation equations based on flow decomposition via source filtering. *Journal of Computational Physics*, 188(2):365–398, 2003.

[27] S. Fechter, F. Hindenlang, H. Frank, C.-D. Munz, and G. Gassner. Discontinuous Galerkin schemes for the direct numerical simulation of fluid flow and acoustics. In *Aeroacoustics Conferences*. American Institute of Aeronautics and Astronautics, June 2012.

[28] M. R. Fink. Prediction of airfoil tone frequencies. *Journal of Aircraft*, 12(2):118–120, 1975.

[29] P. F. Fischer. An overlapping Schwarz method for spectral element solution of the incompressible Navier–Stokes equations. *Journal of Computational Physics*, 133(1):84–101, 1997.

[30] D. Flad, A. Beck, and C.-D. Munz. Simulation of underresolved turbulent flows by adaptive filtering using the high order discontinuous Galerkin spectral element method. *Journal of Computational Physics*, 313:1–12, 2016.

[31] D. Flad, H. Frank, A. D. Beck, and C.-D. Munz. A discontinuous Galerkin spectral element method for the direct numerical simulation of aeroacoustics. *AIAA Paper (2014-2740)*, 2014.

[32] M. Fosas de Pando, P. J. Schmid, and D. Sipp. A global analysis of tonal noise in flows around aerofoils. *Journal of Fluid Mechanics*, 754:5–38, 2014.

[33] H. M. Frank and C.-D. Munz. Direct aeroacoustic simulation of acoustic feedback phenomena on a side-view mirror. *Journal of Sound and Vibration*, 371:132–149, 2016.

[34] H. M. Frank and C.-D. Munz. Large eddy simulation of tonal noise at a simplified side-view mirror using a high order discontinuous Galerkin method. *AIAA Paper (2016-2847)*, 2016.

[35] G. Gassner. *Discontinuous Galerkin methods for the unsteady compressible Navier-Stokes equations*. PhD thesis, Universität Stuttgart, 2009.

[36] G. Gassner and D. A. Kopriva. A comparison of the dispersion and dissipation errors of Gauss and Gauss-Lobatto discontinuous Galerkin spectral element methods. *SIAM Journal on Scientific Computing*, 33(5):2560–2579, 2011.

[37] G. J. Gassner and A. D. Beck. On the accuracy of high-order discretizations for underresolved turbulence simulations. *Theoretical and Computational Fluid Dynamics*, 27(3-4):221–237, 2013.

[38] G. J. Gassner, A. R. Winters, and D. A. Kopriva. Split form nodal discontinuous Galerkin schemes with summation-by-parts property for the compressible Euler equations. *arXiv preprint arXiv:1604.06618*, 2016.

[39] M. Germano, U. Piomelli, P. Moin, and W. H. Cabot. A dynamic subgrid-scale eddy viscosity model. *Physics of Fluids A: Fluid Dynamics (1989-1993)*, 3(7):1760–1765, 1991.

[40] S. Ghosal. An analysis of numerical errors in large-eddy simulations of turbulence. *Journal of Computational Physics*, 125(1):187–206, 1996.

[41] J. Hesthaven and T. Warburton. *Nodal Discontinuous Galerkin Methods. Algorithms, Analysis, and Applications*. Springer, Berlin Heidelberg New York, 2008.

[42] S. Hickel, N. A. Adams, and J. A. Domaradzki. An adaptive local deconvolution method for implicit LES. *Journal of Computational Physics*, 213(1):413–436, 2006.

[43] F. Hindenlang. *Mesh curving techniques for high order parallel simulations on unstructured meshes*. PhD thesis, University of Stuttgart, 2014.

[44] F. Hindenlang, T. Bolemann, and C.-D. Munz. Mesh curving techniques for high order discontinuous Galerkin simulations. In *IDIHOM: Industrialization of High-Order Methods-A Top-Down Approach*, pages 133–152. Springer, 2015.

[45] F. Hindenlang, G. J. Gassner, C. Altmann, A. Beck, M. Staudenmaier, and C.-D. Munz. Explicit discontinuous Galerkin methods for unsteady problems. *Computers & Fluids*, 61:86–93, 2012.

[46] M. Howe. A review of the theory of trailing edge noise. *Journal of Sound and Vibration*, 61(3):437–465, 1978.

[47] F. Q. Hu, M. Hussaini, and P. Rasetarinera. An analysis of the discontinuous Galerkin method for wave propagation problems. *Journal of Computational Physics*, 151(2):921–946, 1999.

[48] X. Huai, R. D. Joslin, and U. Piomelli. Large-eddy simulation of transition to turbulence in boundary layers. *Theoretical and computational fluid dynamics*, 9(2):149–163, 1997.

[49] X. Huai, R. D. Joslin, and U. Piomelli. Large-eddy simulation of boundary-layer transition on a swept wedge. *Journal of Fluid Mechanics*, 381:357–380, 1999.

[50] W.-H. Hucho. *Aerodynamik des Automobils: Strömungsmechanik, Wärmetechnik, Fahrdynamik, Komfort*. Springer-Verlag, 2015.

[51] A. G. Hutton. The emerging role of large eddy simulation in industrial practice: challenges and opportunities. *Philosophical Transactions of the Royal Society of London A: Mathematical, Physical and Engineering Sciences*, 367(1899):2819–2826, 2009.

[52] H. Huynh. A flux reconstruction approach to high-order schemes including discontinuous Galerkin methods. *AIAA paper*, 4079:2007, 2007.

[53] R. Höld, A. Brenneis, A. Eberle, V. Schwarz, and R. Siegert. Numerical simulation of aeroacoustic sound generated by generic bodies placed on a plate: Part I-prediction of aeroacoustic sources. *AIAA paper*, 20:40–60, 1999.

[54] L. Jones, R. Sandberg, and N. Sandham. Direct numerical simulations of forced and unforced separation bubbles on an airfoil at incidence. *Journal of Fluid Mechanics*, 602:175–207, 2008.

[55] L. Jones, R. Sandberg, and N. Sandham. Stability and receptivity characteristics of a laminar separation bubble on an aerofoil. *Journal of Fluid Mechanics*, 648:257–296, 2010.

[56] L. E. Jones and R. D. Sandberg. Numerical analysis of tonal airfoil self-noise and acoustic feedback-loops. *Journal of Sound and Vibration*, 330(25):6137 – 6152, 2011.

[57] M. Kaltenbacher, M. Escobar, S. Becker, and I. Ali. Numerical simulation of flow-induced noise using LES/SAS and Lighthill's acoustic analogy. *International journal for numerical methods in fluids*, 63(9):1103–1122, 2010.

[58] G. Karniadakis and S. Sherwin. *Spectral/hp element methods for computational fluid dynamics*. Oxford University Press, 2013.

[59] Y. Khalighi, A. Mani, F. Ham, and P. Moin. Prediction of sound generated by complex flows at low mach numbers. *AIAA journal*, 48(2):306–316, 2010.

[60] J. W. Kim and R. D. Sandberg. Efficient parallel computing with a compact finite difference scheme. *Computers & Fluids*, 58:70–87, 2012.

[61] M. J. Kingan and J. R. Pearse. Laminar boundary layer instability noise produced by an aerofoil. *Journal of Sound and Vibration*, 322(4):808–828, 2009.

[62] R. M. Kirby and G. E. Karniadakis. De-aliasing on non-uniform grids: algorithms and applications. *Journal of Computational Physics*, 191(1):249–264, 2003.

[63] A. N. Kolmogorov. The local structure of turbulence in incompressible viscous fluid for very large Reynolds numbers. In *Dokl. Akad. Nauk SSSR*, volume 30, pages 299–303, 1941.

[64] D. Kopriva. Metric identities and the discontinuous spectral element method on curvilinear meshes. *Journal of Scientific Computing*, 26(3):301–327, Mar. 2006.

[65] D. A. Kopriva. *Implementing spectral methods for partial differential equations: Algorithms for scientists and engineers*. Springer Science & Business Media, 2009.

[66] D. A. Kopriva and G. Gassner. On the quadrature and weak form choices in collocation type discontinuous Galerkin spectral element methods. *Journal of Scientific Computing*, 44:136–155, 2010.

[67] D. A. Kopriva, S. L. Woodruff, and M. Y. Hussaini. Computation of electromagnetic scattering with a non-conforming discontinuous spectral element method. *International journal for numerical methods in engineering*, 53(1):105–122, 2002.

[68] A. Kravchenko and P. Moin. On the effect of numerical errors in large eddy simulations of turbulent flows. *Journal of Computational Physics*, 131(2):310–322, 1997.

[69] L. Larchevêque, P. Sagaut, I. Mary, O. Labbé, and P. Comte. Large-eddy simulation of a compressible flow past a deep cavity. *Physics of Fluids (1994-present)*, 15(1):193–210, 2003.

[70] J. Larsson and Q. Wang. The prospect of using large eddy and detached eddy simulations in engineering design, and the research required to get there. *Philosophical Transactions of the Royal Society of London A: Mathematical, Physical and Engineering Sciences*, 372(2022):20130329, 2014.

[71] R. B. Lehoucq, D. C. Sorensen, and C. Yang. *ARPACK users' guide: solution of large-scale eigenvalue problems with implicitly restarted Arnoldi methods*, volume 6. Siam, 1998.

[72] S. K. Lele. Compact finite difference schemes with spectral-like resolution. *Journal of computational physics*, 103(1):16–42, 1992.

[73] A. Leonard. Energy cascade in large-eddy simulations of turbulent fluid flows. In *Turbulent Diffusion in Environmental Pollution*, volume 1, pages 237–248, 1974.

[74] M. Lesieur and O. Métais. New trends in large-eddy simulations of turbulence. *Annual Review of Fluid Mechanics*, 28(1):45–82, 1996.

[75] M. J. Lighthill. On sound generated aerodynamically. i. general theory. In *Proceedings of the Royal Society of London A: Mathematical, Physical and Engineering Sciences*, volume 211, pages 564–587. The Royal Society, 1952.

[76] D. K. Lilly. The representation of small scale turbulence in numerical simulation experiments. 1967.

[77] T. H. Lounsberry, M. E. Gleason, and M. M. Puskarz. Laminar flow whistle on a vehicle side mirror. Technical report, SAE Technical Paper, 2007.

[78] C. J. Mack and P. J. Schmid. A preconditioned Krylov technique for global hydrodynamic stability analysis of large-scale compressible flows. *Journal of Computational Physics*, 229(3):541–560, 2010.

[79] L. M. Mack. *Boundary-layer linear stability theory.* AGARD Special course on stability and transition of laminar flow. 1984.

[80] O. Marsden, C. Bogey, and C. Bailly. Direct noise computation of the turbulent flow around a zero-incidence airfoil. *AIAA journal*, 46(4):874–883, 2008.

[81] A. McAlpine, E. Nash, and M. Lowson. On the generation of discrete frequency tones by the flow around an aerofoil. *Journal of Sound and Vibration*, 222(5):753 – 779, 1999.

[82] C. Meneveau and J. Katz. Scale-invariance and turbulence models for large-eddy simulation. *Annual Review of Fluid Mechanics*, 32(1):1–32, 2000.

[83] Y. Morinishi, T. Lund, O. Vasilyev, and P. Moin. Fully conservative higher order finite difference schemes for incompressible flow. *Journal of computational physics*, 143(1):90–124, 1998.

[84] C.-D. Munz, M. Dumbser, and S. Roller. Linearized acoustic perturbation equations for low mach number flow with variable density and temperature. *Journal of Computational Physics*, 224(1):352–364, 2007.

[85] E. Nash, M. Lowson, and A. McAlpine. Boundary layer instability noise on aerofoils. *Journal of Fluid Mechanics*, 382:27–61, 1999.

[86] F. Nicoud and F. Ducros. Subgrid-scale stress modelling based on the square of the velocity gradient tensor. *Flow, turbulence and Combustion*, 62(3):183–200, 1999.

[87] J. Niegemann, R. Diehl, and K. Busch. Efficient low-storage Runge–Kutta schemes with optimized stability regions. *Journal of Computational Physics*, 231(2):364–372, 2012.

[88] S. A. Orszag. Numerical methods for the simulation of turbulence. *Physics of Fluids (1958-1988)*, 12(12):II–250, 1969.

[89] R. W. Paterson, P. G. Vogt, M. R. Fink, and C. L. Munch. Vortex noise of isolated airfoils. *Journal of Aircraft*, 10(5):296–302, 1973.

[90] U. Piomelli. Large-eddy simulation: achievements and challenges. *Progress in Aerospace Sciences*, 35(4):335–362, 1999.

[91] U. Piomelli and T. A. Zang. Large-eddy simulation of transitional channel flow. *Computer physics communications*, 65(1):224–230, 1991.

[92] U. Piomelli, T. A. Zang, C. G. Speziale, and M. Y. Hussaini. On the large-eddy simulation of transitional wall-bounded flows. *Physics of Fluids A: Fluid Dynamics (1989-1993)*, 2(2):257–265, 1990.

[93] B. Plogmann, A. Herrig, and W. Würz. Experimental investigations of a trailing edge noise feedback mechanism on a NACA 0012 airfoil. *Experiments in fluids*, 54(5):1–14, 2013.

[94] S. B. Pope. *Turbulent flows.* Cambridge university press, 2000.

[95] S. Pröbsting, J. Serpieri, and F. Scarano. Experimental investigation of aerofoil tonal noise generation. *Journal of Fluid Mechanics*, 747:656–687, 2014.

[96] C. Pruett, T. Gatski, C. Grosch, and W. Thacker. The temporally filtered Navier–Stokes equations: properties of the residual stress. *Physics of Fluids (1994-present)*, 15(8):2127–2140, 2003.

[97] G. Raman. Advances in understanding supersonic jet screech: review and perspective. *Progress in aerospace sciences*, 34(1):45–106, 1998.

[98] P. L. Roe and J. Pike. Efficient construction and utilisation of approximate Riemann solutions. In *Proc. Of the Sixth Int'L. Symposium on Computing Methods in Applied Sciences and Engineering, VI*, pages 499–518, Amsterdam, The Netherlands, The Netherlands, 1985. North-Holland Publishing Co.

[99] C. W. Rowley, T. Colonius, and A. J. Basu. On self-sustained oscillations in two-dimensional compressible flow over rectangular cavities. *Journal of Fluid Mechanics*, 455:315–346, 2002.

[100] C. W. Rowley, I. Mezić, S. Bagheri, P. Schlatter, and D. S. Henningson. Spectral analysis of nonlinear flows. *Journal of Fluid Mechanics*, 641:115–127, 2009.

[101] T. Rung, D. Eschricht, J. Yan, and F. Thiele. Sound radiation of the vortex flow past a generic side mirror. In *Eighth AIAA/CEAS Aeroacoustics Conference, Breckenridge, CO, Jun*, pages 17–19, 2002.

[102] W. S. Saric, H. L. Reed, and E. J. Kerschen. Boundary-layer receptivity to freestream disturbances. *Annual review of fluid mechanics*, 34(1):291–319, 2002.

[103] A. Schell. *Entwicklung einer Berechnungsmethode zur Vorhersage der Schallausbreitung im Nahfeld eines umströmten Kraftfahrzeugs.* PhD thesis, University of Stuttgart, 2014.

[104] P. C. Schlatter. *Large-eddy simulation of transition and turbulence in wall-bounded shear flow.* PhD thesis, Technische Wissenschaften ETH Zürich, Nr. 16000, 2005, 2005.

[105] H. Schlichting and K. Gersten. *Grenzschicht-theorie.* Springer-Verlag, 2006.

[106] P. J. Schmid. Dynamic mode decomposition of numerical and experimental data. *Journal of Fluid Mechanics*, 656:5–28, 2010.

[107] O. T. Schmidt and U. Rist. Viscid-inviscid pseudo-resonance in streamwise corner flow. *J. Fluid Mech.*, 743:327–357, 2014.

[108] R. Siegert, V. Schwarz, and J. Reichenberger. Numerical simulation of aeroacoustic sound generated by generic bodies placed on a plate. Part II-prediction of radiated sound pressure. In *5th AIAA/CEAS Aeroacoustics Conference and Exhibit*, page 1895, 1999.

[109] J. Slotnick, A. Khodadoust, J. Alonso, D. Darmofal, W. Gropp, E. Lurie, and D. Mavriplis. CFD vision 2030 study: a path to revolutionary computational aerosciences. 2013.

[110] Y. Sun, Z. J. Wang, and Y. Liu. High-order multidomain spectral difference method for the Navier-Stokes equations on unstructured hexahedral grids. *Communications in Computational Physics*, 2(2):310–333, 2007.

[111] C. Tam. Discrete tones of isolated airfoils. *Journal of the Acoustical Society of America*, 55:1173–1177, 1974.

[112] C. K. Tam and J. C. Webb. Dispersion-relation-preserving finite difference schemes for computational acoustics. *Journal of computational physics*, 107(2):262–281, 1993.

[113] V. Theofilis. Advances in global linear instability analysis of nonparallel and three-dimensional flows. *Progress in aerospace sciences*, 39(4):249–315, 2003.

[114] M. Werner. *Experimental study on tonal self-noise generated by aeroacoustic feedback on a side mirror.* PhD thesis, University of Stuttgart (to be submitted), 2017.

[115] M. Werner, W. Würz, and E. Krämer. Experimental investigations of tonal noise on a vehicle side mirror. In *Notes on Numerical Fluid Mechanics and Multidisciplinary Design, Munich, Germany.* STAB/DGLR, 2014.

[116] M. Werner, W. Würz, and E. Krämer. Experimental investigations of the tonal self-noise emission of a vehicle side mirror. In *22nd AIAA/CEAS Aeroacoustics Conference*, 2016.

[117] M. J. Werner, W. Würz, and E. Krämer. Experimental investigations of an aeroacoustic feedback mechanism on a two-dimensional side mirror model. *Journal of Sound and Vibration*, 387:79–95, 2017.

[118] J. F. Williams and L. Hall. Aerodynamic sound generation by turbulent flow in the vicinity of a scattering half plane. *Journal of Fluid Mechanics*, 40(04):657–670, 1970.

[119] J. F. Williams and D. L. Hawkings. Sound generation by turbulence and surfaces in arbitrary motion. *Philosophical Transactions of the Royal Society of London A: Mathematical, Physical and Engineering Sciences*, 264(1151):321–342, 1969.

# List of Tables

2.1 Wall-tangential and wall-normal grid spacing $\Delta x$ and $\Delta y$ at the leading edge (LE) and trailing edge (TE) for the current simulation of the NACA 0012 case and reference [56]. . . . . . 40

3.1 Computational mesh and resolution details for two runs at polynomial degrees $N = 4$ and $N = 7$. . . . . . . . . . . . . . . . . . . 48
3.2 Frequencies of unstable feedback modes from the perturbation calculation $f_p$, their respective frequencies from the power spectra of the LES data $f_{\text{LES}}$ (if detectable), frequency spacing $\Delta f = f_k - f_{k-1}$ and 'loop frequency' $1/T_{\text{loop}}$ for side surface (S) and upper surface (U) measured from Fig. 3.14. . . . . . . . . . . . 72

4.1 Computational setup, resolution and performance details for the base flow (BF) and subdomain (SUB2D and SUB3D) configurations. The grid spacings are taken at the DE approximately at $x = 0.7C$ in Fig. 4.1 (right) and are given as $\Delta x = \Delta x_{\text{Elem}}/(N+1)$ in order to take into account the element-local resolution. $L_z$ and $n_{\text{Elems},z}$ denote the spanwise extent of the domain and the the number of elements in the spanwise direction, respectively. 80
4.2 Feedback frequencies $f_k$ and spacings $\Delta f = f_k - f_{k-1}$ according to the global stability analysis using DMD and predicted by the phase condition (3.3) for $u_\infty = 27.78\,\mathrm{m\,s^{-1}}$. . . . . . . . . . . . 97

# List of Figures

1.1 Left: Idealized diagram of the tone frequency development with respect to free-stream velocity. Thick lines: dominant tones, solid lines: associated side peaks, dashed line: general trend, thin lines: frequencies fulfilling the phase condition. Right: Schematic of the aeroacoustic feedback loop. (1) separation point, (2) amplified instability in the separated shear layer, (3) diffraction at the trailing edge, (4) reinforcement of the instability by the upstream traveling acoustic wave. . . . . . . . . . . . . . . . . . . . . . . . 4

2.1 Comparison of direct and hybrid procedures and their properties for aeroacoustic noise prediction. Here, $(\cdot)_h$ and $(\cdot)_a$ denote hydrodynamic and acoustic components and $S(t)$ represents the acoustic source term. . . . . . . . . . . . . . . . . . . . . . . . . . . 11

2.2 Schematic of a turbulent kinetic energy spectrum. $k_c$ marks the cutoff wavenumber given by the grid resolution. The gray-shaded areas mark the ranges of the marginally resolved scales, which are prone to numerical errors. . . . . . . . . . . . . . . . . . . . . . 16

2.3 Legendre-Gauss points in the volume (filled circles) and on the surface (squares) of the reference element for $N = 3$, $N = 7$ and $N = 11$. . . . . . . . . . . . . . . . . . . . . . . . . . . . . . . 24

2.4 Mortar interface types: (a) 4:1, (b) and (c) 2:1. . . . . . . . . . 28

2.5 Schematic of the mortar procedure. (a) Step 1, projection of the solution $U$ to the mortars. (b) Step 3, projection of the flux from the mortars to the adjacent sides. . . . . . . . . . . . . . . . . . 29

2.6 Free stream preservation test with a non-conforming curved sphere mesh with $N = 4$ and $N_{\text{geo}} = 4$. Shown is the deviation from the free-stream density $\log_{10} |\rho'/\rho_0|$ after 2000 time steps. Left: Global mapping metrics, right: local mapping metrics. . . 31

2.7 Left: Instantaneous vorticity contours over the range $\Omega_z = \pm 100 u_\infty / C$, right: Volume dilatation contours in the range $\vec{\nabla}_x \cdot \vec{v} = \pm 0.1 u_\infty / C$. . . . . . . . . . . . . . . . . . . . . . . . . . . 41

2.8 PSD of pressure at $\vec{x}/C = (0.5, 0.5)$, where the origin is placed at the leading edge of the airfoil. . . . . . . . . . . . . . . . . . 42

3.1 Left: mirror model in the LWT. Right: Mirror geometry. Marked areas are *(S)*: Side surface, *(U)*: Upper surface, *DE*: Design edge. The $\delta_{99,\mathrm{WT}}$ line marks the approximate thickness of the wind tunnel boundary layer in the experiments and $s$ is a body-fitted coordinate with origin at the trailing edge. . . . . . . . . . . . 46
3.2 Cut view of the computational mesh. . . . . . . . . . . . . . . . 48
3.3 Computational and measured pressure coefficient distributions along surface lines $z = 110$, $z = 91$, $z = 71$ and $y = -50\,\mathrm{mm}$. The wall-tangential distance to the trailing edge is denotes by $s$. 50
3.4 Isocontours of the time-averaged pressure coefficient and surface streamlines based on wall friction. . . . . . . . . . . . . . . . 51
3.5 Comparison of PIV data (a,c) with the simulation results (b,d) in the $z = 110\,\mathrm{mm}$ cut. (a,b): Time-averaged velocity magnitude $\langle \vec{v} \cdot \vec{v} \rangle^{1/2}$, (c,d): RMS velocity fluctuations $\langle \vec{v}' \cdot \vec{v}' \rangle^{1/2}$, both in $\mathrm{m\,s^{-1}}$. . . . . . . . . . . . . . . . . . . . . . . . . . . . . 52
3.6 Time-averaged profiles of wall-tangential velocity $u_s/u_\delta$ plotted over $y/\delta_{99}$ from LES and hotwire measurements. The streamwise position is marked with the wall-tangential distance to the trailing edge, $s$. . . . . . . . . . . . . . . . . . . . . . . . . . . 54
3.7 SPL for selected frequencies and overall SPL (bottom right) on a spherical evaluation surface of $r = 500\,\mathrm{mm}$ placed around the mirror. . . . . . . . . . . . . . . . . . . . . . . . . . . . . 56
3.8 PSD of pressure at two positions outside of the unsteady hydrodynamic field. The experimental low-freq. mode and high-freq. mode datasets are obtained via conditional averaging of the spectra. PSD reference value: $4 \cdot 10^{-10}\mathrm{Pa}^2/\mathrm{Hz}$. . . . . . . . . 57
3.9 PSD of the wall pressure fluctuations along the coordinate $r$ at the trailing edge. PSD reference value: $4 \cdot 10^{-10}\mathrm{Pa}^2/\mathrm{Hz}$. . . . . 58
3.10 Vortical structures at a flow field snapshot visualized by isosurfaces of $Q = 100(u_\infty/L)^2$ colored with velocity magnitude. . . . 59
3.11 Left: Spectrum of the integral kinetic energy on an evaluation surface at the trailing edge. Right: Spatial development of the local maximum in the wall-tangential velocity $\hat{u}_{\max}/u_\infty$ for selected modes from the simulation and hotwire measurements at $z = 110\,\mathrm{mm}$. The light gray shaded lines represent computational modes in the band $2000\,\mathrm{Hz} \leq f \leq 4000\,\mathrm{Hz}$. . . . . . . . . . . . 60

3.12 Left column: isosurfaces of (the real part of) positive and negative streamwise velocity for three DFT modes. The levels are chosen to ensure comparability. Right column: Pressure contours at $z = 110\,\mathrm{mm}$. . . . . . . . . . . . . . . . . . . . . . . . . . . . 62

3.13 Integral amplification $n(f, s)$ at $z = 110\,\mathrm{mm}$ along the streamwise coordinate for selected frequencies ($277\,\mathrm{Hz} \leq f \leq 8830\,\mathrm{Hz}$, left) and at selected streamwise positions over frequency (right). . . 65

3.14 Time evolution of the disturbance wavepacket visualized by isosurfaces of the streamwise velocity disturbance $u'/u_\infty = \pm 10^{-7}$. Grayscale density contours with $-10^{-10} \leq \rho/\rho_\infty \leq 10^{-10}$ on slices at $z = 110\,\mathrm{mm}$ and $y = 0\,\mathrm{mm}$ characterize the acoustic radiation. . . . . . . . . . . . . . . . . . . . . . . . . . . . 67

3.15 Time evolution of the pressure perturbation magnitude $|p'/p_\infty|$ along the wall-tangential line at $z = 110\,\mathrm{mm}$. . . . . . . . . . . 68

3.16 Perturbation wall pressure $p'/p_\infty$ at the trailing edge at $z = 110\,\mathrm{mm}$ (top) and $y = -6\,\mathrm{mm}$ (bottom) as a function of time. . 69

3.17 Ritz spectrum of the DMD based on the perturbation calculation in the complex stability plane. $\omega_r > 0$ defines the unstable halfplane, coloring and size indicate the Euclidean norm $||\hat{\mathbf{k}}_j||$ of the respective mode. The symmetric complex conjugate part is omitted. . . . . . . . . . . . . . . . . . . . . . . . . . . . 71

3.18 Isosurfaces of positive (red) and negative (blue) streamwise velocity $\hat{u}_i/u_\infty$ of selected unstable dynamic modes. . . . . . . . . 71

4.1 Left: Original mirror geometry with the cut at $z = 110\,\mathrm{mm}$, center: Extruded mirror model, right: Cross-sectional view through the mirror model. . . . . . . . . . . . . . . . . . . . . . . . . . 76

4.2 Left: computational mesh of the base flow simulation including the boundaries of the subdomain. Right: computational mesh of the subdomain simulation. . . . . . . . . . . . . . . . . . . . . . . 78

4.3 Isocontours of the time-averaged velocity magnitude $\langle|\vec{v}|/u_\infty\rangle$ and exemplary streamlines for case BF. . . . . . . . . . . . . 81

4.4 Isosurfaces of the $Q$ criterion for $Q = 5(u_\infty/C)^2$ colored with velocity magnitude $|\vec{v}|$ for a random instant of simulation BF. . 82

4.5 Left: Pressure coefficient on the upper surface of the mirror model for simulation BF and corresponding measurements. For comparison, the pressure coefficient is also given for the original mirror at $z = 110\,\mathrm{mm}$. Right: PSD spectrum of pressure at $\vec{x} = (3.22C, 3.6C)^T$ for simulation BF and the corresponding inflow microphone measurement. Reference value $p_{\mathrm{ref}} = 4 \cdot 10^{-10}\mathrm{Pa}^2/\mathrm{Hz}$. 83

4.6 Left: Pressure coefficient on the upper surface of the mirror model for cases BF, SUB2D and SUB3D. Right: Displacement thickness Reynolds number $Re_{\delta^*}$ and shape factor $H$ for cases BF, SUB2D and SUB3D. . . . . . . . . . . . . . . . . . . . . . . . 86

4.7 Contours of instantaneous spanwise vorticity $\Omega_z$ for SUB2D (top) and SUB3D (bottom). The 10 contour levels range between $-200 \le \Omega_z C/u_\infty \le 200$. . . . . . . . . . . . . . . . . . . . . . . . . . 87

4.8 Isosurfaces of the $Q$ criterion for $Q = 50(u_\infty/C)^2$ colored with velocity magnitude $|\vec{v}|$ for a random instant of simulation SUB3D. 87

4.9 Left: Contours of instantaneous fluctuation pressure $c_p - \langle c_p \rangle$ with 11 levels ranging between ±0.02 for case SUB2D. Right: PSD spectrum of pressure at $\vec{x} = (1.0C, 0.6C)^T$ (TE) and $(1C, 1.5C)^T$ (ac.) for simulations SUB2D and SUB3D. Reference value $p_{\mathrm{ref}} = 4 \cdot 10^{-10}\mathrm{Pa}^2/\mathrm{Hz}$. . . . . . . . . . . . . . . . . . . . . . . . . . . 89

4.10 Campbell diagram for the PSD of pressure at the probe position indicated in Fig. 4.9 (left), envelope of the most amplified frequency $f_{\mathrm{max,LST}}$ and the frequencies predicted by the phase condition $f_{\mathrm{ph}}$ (eq. (4.2)). Reference value $p_{\mathrm{ref}} = 4 \cdot 10^{-10}\mathrm{Pa}^2/\mathrm{Hz}$. 92

4.11 Visualization of the wavepacket time evolution by means of density perturbation contours with $-1 \cdot 10^{-8} \le \rho' \le -1 \cdot 10^{-8}$. 94

4.12 Contours of the perturbation wall pressure $|p'/p_\infty|$ plotted over the wall-tangential coordinate $s$ and time $\tilde{t}$. The contours are distributed exponentially to cover the amplitude range. . . . . 95

4.13 Spectrum of Ritz values delivered by the DMD algorithm based on the perturbation simulation in the time interval $0 \le t \le 5$. Size and color coding indicate the Euclidean norm $||\hat{\mathbf{k}}_j||$ of the respective mode. The symmetric complex conjugate part is omitted. 96

4.14 Possible modifications of the mirror model to counteract tonal noise generation. . . . . . . . . . . . . . . . . . . . . . . . . . . 98

4.15 Left: acoustic spectra resulting from the baseline geometry for various free-stream velocities. Right: Corresponding $N$ factor yielded by LST for $u_\infty = 27.78$ and $15\,\mathrm{m\,s}^{-1}$. Reference value $p_{\mathrm{ref}} = 4 \cdot 10^{-10}\mathrm{Pa}^2/\mathrm{Hz}$. . . . . . . . . . . . . . . . . . . . . . . . . . 100

4.16 Left: acoustic spectra for the truncated trailing edge with $s_t = 6, 7$ and $8\,\mathrm{mm}$ at $u_\infty = 27.78\,\mathrm{m\,s^{-1}}$. For clarity, the consecutive cases are shifted by $40\,\mathrm{dB}$ each. Right: $N$ factor yielded by LST for the baseline and truncated geometries at $u_\infty = 27.78$ and $15\,\mathrm{m\,s^{-1}}$. Reference value $p_{\mathrm{ref}} = 4 \cdot 10^{-10}\mathrm{Pa}^2/\mathrm{Hz}$. . . . . . . . . 101
4.17 Streamwise distribution of the wall-normal position of the inflection point $y_I$ for the truncated trailing edge cases at $u_\infty = 27.78\,\mathrm{m\,s^{-1}}$. . . . . . . . . . . . . . . . . . . . . . . . . . . 102
4.18 Lowered trailing edge configurations. . . . . . . . . . . . . . . . . 103
4.19 Acoustic spectra with lowered trailing edge at $u_\infty = 27.78\,\mathrm{m\,s^{-1}}$. For clarity, the consecutive cases are shifted by $40\,\mathrm{dB}$ each. Left: two-dimensional simulations, right: three-dimensional simulations. Reference value $p_{\mathrm{ref}} = 4 \cdot 10^{-10}\mathrm{Pa}^2/\mathrm{Hz}$. . . . . . . . . . . 103
4.20 Mean inflection point position $y_I$ for the lowered trailing edge configurations. . . . . . . . . . . . . . . . . . . . . . . . . . . . 104
4.21 Instantaneous snapshots of spanwise vorticity contours for these configurations with $-200 \leq \Omega_z C/u_\infty \leq 200$. . . . . . . . . . . . 105
4.22 Top row: modified contours, bottom row: magnitude of the corresponding second derivatives $|\vec{x}''(t)| = |\frac{d^2\vec{x}}{dt^2}|$. . . . . . . . . 106
4.23 Left: Acoustic spectra for the modified DE at $u_\infty = 27.78\,\mathrm{m\,s^{-1}}$. Reference value $p_{\mathrm{ref}} = 4 \cdot 10^{-10}\mathrm{Pa}^2/\mathrm{Hz}$. Right: corresponding pressure coefficient $c_p$. . . . . . . . . . . . . . . . . . . . . . . . 108
4.24 Instantaneous contours of vorticity $-200 \leq \Omega_z C/u_\infty \leq 200$ for the modified DE cases at $u_\infty = 27.78\,\mathrm{m\,s^{-1}}$. . . . . . . . . . . 109

# Lebenslauf

| | |
|---|---|
| 27.07.1985 | Geboren in Filderstadt |
| 1992 - 1996 | Grundschule, Simmozheim |
| 1996 - 2005 | Johannes Kepler Gymnasium, Weil der Stadt |
| 2005 | Allgemeine Hochschulreife |
| 2005 - 2006 | Zivildienst in der Schule für Körperbehinderte, Sindelfingen |
| 2006 - 2012 | Studium der Luft- und Raumfahrttechnik an der Universität Stuttgart, Vertiefungsrichtungen: Strömungslehre, Luftfahrtantriebe |
| 2009 | Auslandssemester an der North Carolina State University, Raleigh, USA |
| 2012 - 2016 | Wissenschaftlicher Mitarbeiter am Institut für Aerodynamik und Gasdynamik der Universität Stuttgart |

Stuttgart, den 09.11.2016 Hannes Frank